Beyond optical profiling

Innovative use of the lidar technique in atmospheric research

Von der Fakultät für Physik und Geowissenschaften

der Universität Leipzig

genehmigte

HABILITATIONSSCHRIFT

zur Erlangung des akademischen Grades
DOCTOR RERUM NATURALIUM HABILITATUS
Dr. rer. nat. habil.

vorgelegt

von

Dr. rer. nat. Matthias Tesche

geboren am 27. Januar 1981 in Leipzig

Tag der Verleihung: 20. Juli 2020

Gutachter: Prof. Dr. Jacques Pelon   Sorbonne Université
               Prof. Dr. Johan Ström   Stockholms Universitet
               Prof. Dr. Manfred Wendisch Universität Leipzig

Bibliographische Beschreibung:

Tesche, Matthias
Beyond optical profiling —
Innovative use of the lidar technique in atmospheric research
Universität Leipzig, Habilitationsschrift
329 Seiten, 185 Referenzen, 15 Abbildungen, 3 Tabellen

Referat:

Es ist noch nicht lange her, dass sich die Lidartechnik von einer Nische hochspezialisierter Instrumentalisten dahingehend gewandelt hat, ihr volles Potential der Atmosphärenforschung zugänglich zu machen. Diese Entwicklung lässt sich auf drei Faktoren zurückführen. Zunächst wurden die Kosten für Lidargeräte durch Entwicklungen in der Lasertechnik und dem Angebot optischer Bauteile so weit gesenkt, dass kommerzielle Anbieter Produkte entwickeln konnten, die neuen Nutzern den Einstieg in die Lidarforschung ermöglichten. Desweiteren gelang es, die Ausgabeparameter verschiedener Messgeräte sowie die größtenteils individualisierten Auswertealgorithmen zu homogenisieren. Zuletzt führte die erste Langzeitmission eines weltraumgetragenen Lidargeräts zu einem globalen Datensatz, der auch Nutzern, die bisher nicht mit Lidardaten gearbeitet hatten, das Potential dieser Messungen aufzeigte und zu neuen Auswertemethoden führte.

Diese Habilitationsschrift gibt einen Überblick über Fortschritte in der Lidartechnik und der Nutzung von lidarspezifischen Parametern über die konventionelle Bestimmung optischer Partikel- oder Wolkeneigenschaften hinaus. Diese Arbeit unterteilt sich in vier Themenbereiche. Die Veröffentlichungen im ersten Themenbereich beschreiben, wie der Bedarf an Informationen zur atmosphärischen Aschebelastung nach Vulkanausbrüchen zu Methoden zur Bestimmung von Partikelmassenkonzentrationen und der Konzentration von Partikeln, die für die Wolkenbildung und -entwicklung relevant sind, geführt hat. Im zweiten Themenbereich werden Veröffentlichungen besprochen, die einerseits die Evaluierung von weltraumgetragenen Lidarmessungen beschreiben und andererseits darstellen, wie diese Daten für neuartige Studien, wie sie bisher mit bodengebundenen Messungen nicht möglich waren, verwendet werden können. Der dritte Themenbereich beschreibt die Weiterentwicklung der Inversion von Lidardaten zur Anwendung auf Messungen von nichtsphärischen Partikeln. Der vierte und letzte Themenbereich stellt dar, wie die Erkenntnisse zu lidarspezifischen Parametern zusammen mit lidarspezifischen Methoden derart angepasst werden können, dass sie zu einer umfangreicheren Auswertung bodengebundener passiver Fernerkundung mit Sonnenphotometern zurate gezogen werden können.

Diese Arbeit demonstriert das Potential von Lidarmessungen und lidarspezifischen Methoden für die Atmosphärenforschung. Der Wandel der Lidarfernerkundung von einer durch Instrumentenentwicklung angetriebenen und stark spezialisieren Randgruppe zu einem Feld das bequem zu verwendende Daten für andere Nutzer zur Verfügung stellt, ist allerding noch lange nicht abgeschlossen. Die Einbindung komplexer Lidargeräte in Messstationen für bodengebunde Langzeitbeobachtungen mit synergistischen Geräteparks hat gerade erst begonnen. Diese Entwicklung wird auch für die nächsten Jahre für eine anhaltende Weiterentwicklung der Lidartechnik und lidarspezifischer Methoden sorgen.

Abstract:

It is only since about the middle of the first decade of this century that the lidar technique has left the niche of a rather small, instrument-focussed group of specialists to provide its full potential to the wider community of atmospheric scientists. This is the combined result of three developments. Most importantly, advances in laser technology and optical elements led to a strong decrease in the cost of lidar instruments and to customized commercially available systems. At the same time, a strong effort was made towards the homogenization and quality-assurance of the products being available from those instruments. Finally, the first long-term aerosol lidar in space produced a global, well documented, and easily accessible data set that demonstrates the potential of lidar measurements to data users previously unacquainted with this technique and opened new pathways for data exploitation.

This habilitation thesis describes advances in using the lidar technique and the inferred lidar-specific parameters for applications that go beyond the conventional retrieval of the optical properties of aerosols and clouds. The work is sorted into four themes that describe (1) the pathway of moving from the retrieval of aerosol optical properties to number and mass concentrations, (2) the validation and innovative use of spaceborne lidar observations, (3) advances in the inversion of lidar data, and (4) the use of lidar-specific parameters in the analysis of sun photometer data. The papers in Theme 1 describe how the necessity to provide profiles of the mass concentration of volcanic ash rather than aerosol optical properties for the assessment of aviation safety in the aftermath of volcanic eruptions led to the development of new lidar-based products that enable height-resolved remote sensing of the concentrations of those particles that are relevant for cloud formation and evolution. Theme 2 presents papers that on the one hand assess the quality of spaceborne lidar observations based on ground-based measurements and on the other hand use the new perspective provided by spaceborne lidar for innovative research that would not have been possible with ground-based instruments. The papers in Theme 3 describe recent progress that has been made in the inversion of lidar data for the retrieval of microphysical particle properties for observations performed in the presence of non-spherical mineral dust particles. Finally, Theme 4 gives an overview of how lidar-specific parameters and the insight gained about these parameters over the last ten years can be exploited for a more comprehensive analysis of data taken from ground-based passive remote sensing with sun photometers.

The papers included in this work demonstrate the potential of lidar measurements and lidar-based methods for the larger atmospheric science community. However, the transformation of lidar-based research from an instrument-development driven, highly specialized fringe topic towards a field focussed on providing data products that are easily accessible by the wider scientific community is still far from complete. The integration of advanced lidar measurements into routine and synergistic multi-instrumental ground-based observing systems has only begun. This development is likely to provide further momentum to the evolution of the lidar technique and lidar-based methods over the years to come.

List of Papers

The following papers, referred to in the text by their Roman numerals I to XIV and collated according to four research clusters, are included in this cumulative habilitation thesis. Reprints have been made with permission from the publishers.

Theme 1: From aerosol optical properties to number and mass concentrations

PAPER I   The 16 April 2010 major volcanic ash plume over central Europe: EARLINET lidar and AERONET photometer observations at Leipzig, Germany
Ansmann, A., **M. Tesche**, S. Groß, V. Freudenthaler, P. Seifert, A. Hiebsch, J. Schmidt, U. Wandinger, I. Mattis, D. Müller, and M. Wiegner (2010)
Geophys. Res. Lett., **37**, https://doi.org/10.1029/2010GL043809.

PAPER II   Ash and fine-mode particle mass profiles from EARLINET-AERONET observations over central Europe after the eruptions of the Eyjafjallajökull volcano in 2010
Ansmann, A., **M. Tesche**, P. Seifert, S. Groß, V. Freudenthaler, A. Apituley, K. Wilson, I. Serikov, V. Linné, B. Heinold, A. Hiebsch, F. Schnell, J. Schmidt, I. Mattis, U. Wandinger, and M. Wiegner (2011)
J. Geophys. Res., **116**, https://doi.org/10.1029/2010JD015567.

PAPER III   Volcanic ash over Scandinavia originating from the Grímsvötn eruptions in May 2011
Tesche, M., P. Glantz, C. Johansson, M. Norman, A. Hiebsch, A. Ansmann, D. Althausen, R. Engelmann, and P. Seifert (2012)
J. Geophys. Res., **117**, https://doi.org/10.1029/2011JD017090.

PAPER IV   Profiling of fine and coarse particle mass: Case studies of Saharan dust and Eyjafjallajökull/Grimsvötn volcanic plumes
Ansmann, A., P. Seifert, **M. Tesche**, and U. Wandinger (2012)
Atmos. Chem. Phys., **12**, https://doi.org/10.5194/acp-12-9399-2012.

PAPER V   Retrieval of ice-nucleating particle concentrations from lidar observations and comparison with UAV in situ measurements
Marinou, E., **M. Tesche**, A. Nenes, A. Ansmann, J. Schrod, D. Mamali, A. Tsekeri, M. Pikridas, H. Baars, R. Engelmann, K.-A. Voudouri, S. Solomos, J. Sciare, S. Groß, F. Ewald, and V. Amiridis (2019)
Atmos. Chem. Phys., **19**, https://doi.org/10.5194/acp-19-11315-2019.

Theme 2: Validation and innovative use of spaceborne lidar observations

PAPER VI   Ground–based validation of CALIPSO observations of dust and smoke in the Cape Verde region
Tesche, M., U. Wandinger, A. Ansmann, D. Althausen, D. Müller, and A. Omar (2013)
J. Geophys. Res., **118**, https://doi.org/10.1002/jgrd.50248.

PAPER VII   Assessing lidar-based classification schemes for Polar Stratospheric Clouds based on 16 years of lidar measurements at Esrange, Sweden
Achtert, P. and **M. Tesche** (2014)
J. Geophys. Res., **119**, https://doi.org/10.1002/2013JD020355.

PAPER VIII Reconciling aerosol light extinction measurements from spaceborne lidar observations and in-situ measurements in the Arctic
Tesche, M., P. Zieger, N. Rastak, R. J. Charlson, P. Glantz, P. Tunved, and H.-C. Hansson (2014)
Atmos. Chem. Phys., **14**, https://doi.org/10.5194/acp-14-7869-2014.

PAPER IX   Aviation effects on already-existing cirrus clouds
Tesche, M., P. Achtert, P. Glantz, and K. Noone (2016)
Nature Comms., **7**, https://doi.org/10.1038/ncomms12016.

Theme 3: Advances in the inversion of lidar data

PAPER X   Vertical profiles of pure dust and mixed smoke-dust plumes inferred from inversion of multiwavelength Raman/polarization lidar data and comparison to AERONET retrievals and in situ observations
Müller, D., I. Veselovskiy, A. Kolgotin, **M. Tesche**, A. Ansmann, and O. Dubovik (2013)
Appl. Opt., **52**, https://doi.org/10.1364/AO.52.003178.

PAPER XI   3+2+X: What is the most useful depolarization input for retrieving microphysical properties of non-spherical particles from lidar measurements using the spheroid model of Dubovik et al. (2006)?
Tesche, M., A. Kolgotin, M. Haarig, S. P. Burton, R. A. Ferrare, C. A. Hostetler, and D. Müller (2019)
Atmos. Meas. Techn., **12**, https://doi.org/10.5194/amt-12-4421-2019.

Theme 4: Use of lidar-specific parameters in the analysis of sun photometer data

PAPER XII   On the spectral depolarisation and lidar ratio of mineral dust provided in the AERONET version 3 inversion product
Shin, S.-K., **M. Tesche**, K. Kim, M. Kezoudi, B. Tatarov, D. Müller, and Y. Noh (2018)
Atmos. Chem. Phys., **18**, https://doi.org/10.5194/acp-18-12735-2018.

PAPER XIII   Technical note: Absorption aerosol optical depth components from AERONET observations of mixed dust plumes
Shin, S.-K., **M. Tesche**, D. Müller, and Y. Noh (2019)
Atmos. Meas. Techn., **12**, https://doi.org/10.5194/amt-12-607-2019.

PAPER XIV   Aerosol-type classification based on AERONET version 3 inversion products
Shin, S.-K., **M. Tesche**, Y. Noh, and D. Müller (2019)
Atmos. Meas. Techn., **12**, https://doi.org/10.5194/amt-12-3789-2019.

Contents

1 Introduction

The light detection and ranging (lidar) technique has been used for height-resolved measurements of aerosols and clouds for several decades. It has only been over the last ten to 15 years, however, that different applications have been combined into advanced lidar instruments (Wandinger 2005a). These state-of-the-art lidars provide the data needed to gain insight into particle load (extinction and backscatter coefficients), size (measurements at multiple wavelengths), and shape (polarization-sensitive measurements). Today, advanced lidars give intensive optical parameters that allow for detailed aerosol characterization (Tesche et al. 2009a, 2011a, Burton et al. 2013, Groß et al. 2013) and the separation of the contribution of different aerosol types such as mineral dust, biomass-burning smoke, continental pollution, or marine aerosol within mixed layers (Tesche et al. 2009b, 2011b, Burton et al. 2014). In addition, methodologies have been developed to derive aerosol microphysical properties (i.e. size distribution, concentration, effective radius, complex refractive index, Ansmann and Müller 2005) as well as mass concentration profiles (Ansmann et al. 2012, Mamouri and Ansmann 2014) from the measured optical parameters. Lidar observations have been used in the aftermath of the eruptions of the Icelandic volcanoes Eyjafjallajökull (Ansmann et al. 2011a) and Grímsvötn (Tesche et al. 2012) to derive ash mass-concentration profiles. This information was crucial for assessing aviation safety when surface-based and column-integrated measurements could not provide the required information to stakeholders and decision makers. The method for converting profiles of aerosol extinction coefficients into height-resolved aerosol mass concentration has been expanded by Mamouri and Ansmann (2015, 2016) towards the retrieval of aerosol number concentration profiles from which concentrations of cloud condensation nuclei (CCN) and ice nucleating particles (INP) are derived using measurement-based parametrizations for mineral dust, marine aerosols, and continental pollution (DeMott et al. 2010, 2015a, 2016, Niemand et al. 2012, Steinke et al. 2015, Ullrich et al. 2017).

The optical data obtained from advanced lidar measurement at multiple wavelength can also be used to infer aerosol microphysical properties by means of data inversion (Ansmann and Müller 2005). The purpose of this procedure, which addresses an ill-posed problem that can only be solved numerically, is to find those sets of microphysical particle properties that best describe the measured optical data. The methodology has matured over the last 20 years to now provide the desired information in near-real time (Müller et al. 2014, Müller et al. 2019). Comparisons to independent in-situ measurements confirm that parameters retrieved from the inversion of lidar measurements are reasonable (Sawamura et al. 2017). However, the inversion of lidar data that have been collected in the presence of nonspherical particles such as mineral dust or volcanic ash still poses a major challenge. This is because there is no mathematically exact method for describing the light-scattering by particles whose shape deviates from that of a sphere (Mie 1908). Efforts have been made to use spheroids (Dubovik et al. 2006) or irregularly shaped particles (Gasteiger et al. 2011) in the inversion of optical remote-sensing measurements of the atmosphere. But so far, no approach has fully met the requirements of the remote-sensing community. Ultimately, such a

light-scattering model needs to be universally applicable to both active and passive remote-sensing observations with the goal of reconciling them with independent measurements of microphysical and optical particle properties. Nevertheless, light scattering by randomly oriented spheroids currently marks the best available option to address the problem.

Spaceborne lidar measurements with the Cloud-Aerosol Lidar with Orthogonal Polarization (CALIOP) aboard the Cloud-Aerosol Lidar and Infrared Pathfinder Satellite Observations (CALIPSO, Winker et al. 2009) satellite within the A-Train constellation of polar-orbiting satellites have been available since June 2006. Since then, CALIOP has provided an unprecedented view of the global height-resolved distribution of atmospheric aerosols and clouds. It spawned an abundance of validation efforts with ground-based and airborne lidar instruments but also introduced the concept of lidar profiling and the inferred products to a wide field of researchers that had never been in contact with lidar before but now had the opportunity to exploit the data to pursue their research interests.

Another pathway for expanding lidar research to other fields is by adapting the insights gained over the last decade to measurements conducted with other optical remote-sensing instruments. Lidar and sun photometer observations are based on measuring scattered light. They are quite complementary, and thus, the two types of instrument are often collocated. Therefore, is seems natural to find a way to apply lidar-specific methods to data inferred from sun-photometer measurements. This has become possible since lidar-specific parameters have become a standard output of the inversion of ground-based sun-photometer measurements and characteristic values of the different parameters for pure aerosol types have been collected with today's advanced lidar instruments.

This cumulative habilitation thesis presents advances on the items listed above. The included papers have been sorted according to four themes that have defined the author's research activities since receiving his title of Doctor rerum naturalium in 2011:
    Theme 1: From aerosol optical properties to number and mass concentrations
    Theme 2: Validation and innovative use of spaceborne lidar observations
    Theme 3: Advances in the inversion of lidar data
    Theme 4: Use of lidar-specific parameters in the analysis of sun photometer data

Chapter 2 provides the theoretic background of the remote-sensing methods considered in this work. This includes the basics of light scattering, the fundamentals of active remote sensing with lidar and passive remote sensing with sun photometers, as well as the adaptation of lidar-specific methods for the analysis of sun-photometer measurements. Chapter 3 discusses some highlights of the author's work since 2011 according to the themes introduced above. Chapter 4 summarizes the comprehensive results of the publications included in this work and concludes this thesis.

2 Background

2.1 Light scattering in the atmosphere

[1]Light in the atmosphere becomes visible for the human eye after the interaction with scatterers. These scatterers can be molecules, cloud droplets, aerosol particles, as well as rain or snow. When interfering with scatterers light might also be absorbed. The sum of scattering and absorption within a certain volume is called extinction. Light extinction depends on the wavelength λ of incident light. Its measure is the volume extinction coefficient α_λ that describes the attenuation of light travelling through a medium.

The intensity of scattered light of a certain wavelength varies with the size, the shape, and the complex refractive index of a scatterer. It furthermore strongly depends on the direction of scattering which is defined by the zenith angle Θ and the azimuth angle Φ in spherical coordinates. The intensity of light that is scattered in the direction (Θ, Φ) is described by the scattering phase function $p_\lambda(\Theta, \Phi)$ (van de Hulst 1957, Bohren and Huffman 1983). It is a dimensionless function whose integral over all directions is generally normalized to unity. The scattering phase function displays distinctive features for different scatterers, especially in sidewards and backward direction. The integral of the scattering phase function of an ensemble of scatterers is proportional to the volume extinction coefficient. Scattering in the direction of propagation of the incident beam of light ($\Theta = 0°$) is referred to as forward scattering while scattering in the direction of the primary source ($\Theta = 180°$) is referred to as backward scattering or backscattering. The intensity of the backscattered light is described by the volume backscatter coefficient β_λ. The backscatter coefficient strongly depends on the effective size and the mean refractive index of an ensemble of scatterers. The imaginary part of the refractive index controls the absorptive properties of a particle.

In physical terms, light is an electromagnetic wave with an electric field vector **E** that is periodically oscillating perpendicular to the direction of propagation (z-direction). It is called linearly polarized, if the oscillation is restricted to a single plane. The x and y components of the wave are in phase and the field vector draws a line in the x-y-plane. The electric field vector rotates with time, if a $90°$ phase shift occurs between its x and y components. It now draws a circle in the x-y-plane and is called circularly polarized. If the phase shift differs from $90°$, light is called elliptically polarized. The latter also is the general case of polarization (van de Hulst 1957, Bohren and Huffman 1983). Natural sunlight is unpolarized because it consists of a multitude of waves that are polarized in an infinite variety of ways.

The intensity and the state of polarization of a light beam are fully described by its Stokes vector **S** $= (I, Q, U, V)$. The four elements of this vector are called Stokes parameters and characterize the total intensity I, the intensity along the x and y axes Q, the intensity along the $+45°$ and $-45°$ axes U, and the intensity that is right-hand circular and left-hand circular

---

[1]Parts of this section has been adapted from Tesche (2011).

V. The latter parameter describes the rotation of the electric field vector in case of elliptically polarized light. The Stokes vector is often normalized to its first element, i.e. I equals unity. For example, the Stokes vector of unpolarized light is $\boldsymbol{S} = (1, 0, 0, 0)$, while it is $\boldsymbol{S} = (1, 1, 0, 0)$ for linearly (along the x axis) and $\boldsymbol{S} = (1, 0, 0, 1)$ for (left-hand) circularly polarized light. The relation between the intensity and state of polarization of scattered light $\boldsymbol{S}$ and the intensity and state of polarization of incident light $\boldsymbol{S}_0$ is fully described as $\boldsymbol{S} = \mathbf{F}(\Theta, \Phi)\boldsymbol{S}_0$.

The normalized 4×4 transformation matrix $\mathbf{F}$ is dimensionless and is referred to as scattering matrix. It consists of 16 elements $F_{ij}(\Theta, \Phi)$ that depend on the scattering angles Θ and Φ (van de Hulst 1957, Bohren and Huffman 1983). In case of first-order scattering by randomly oriented non-spherical particles having a plane of symmetry, e.g. spheroids, the matrix simplifies to

$$\mathbf{F}(\Theta) = \begin{bmatrix} F_{11} & F_{12} & 0 & 0 \\ F_{12} & F_{22} & 0 & 0 \\ 0 & 0 & F_{33} & -F_{43} \\ 0 & 0 & F_{43} & F_{44} \end{bmatrix} \tag{2.1}$$

and becomes diagonal for exact backscattering when $F_{12}(180°) = F_{43}(180°) = 0$,

$$\mathbf{F}(180°) = \begin{bmatrix} F_{11} & 0 & 0 & 0 \\ 0 & F_{22} & 0 & 0 \\ 0 & 0 & F_{33} & 0 \\ 0 & 0 & 0 & F_{44} \end{bmatrix} = \begin{bmatrix} a_1 & 0 & 0 & 0 \\ 0 & a_2 & 0 & 0 \\ 0 & 0 & -a_2 & 0 \\ 0 & 0 & 0 & a_1 - 2a_2 \end{bmatrix}, \tag{2.2}$$

with only two independent parameters a_1 and a_2. The first element $F_{11}(\Theta) = a_1(\Theta)$ is identical to the phase function $p(\Theta)$. Usually, all elements of the transformation matrix are normalized to the first element $F_{11} = a_1$. In case of backscattering by spherical particles the normalized scattering matrix simplifies even further as $a_1 = a_2 = 1$. Transforming an incident beam of linearly polarized light with this matrix preserves the state of polarization as it is observed for backscattering by spherical cloud droplets.

Depending on the wavelength of the incident light and the size (radius r) of the scatterers, different kinds of scattering are discerned. Rain drops and ice crystals are very large compared to the wavelength of incident light ($r \gg \lambda$). While these scatterers show no wavelength dependence of the intensity of scattered light, refraction of light at their surfaces can cause optical phenomena like rainbows or halos. If the size of the scatterers decreases to the dimension of the wavelength of incident light ($r \approx \lambda$), the intensity of scattering is approximately proportional to the inverse of the wavelength but can also vary strongly depending on the kind of scatterers. This case is often called Mie scattering, despite the fact that this term originally refers to scattering of electromagnetic waves by spherical objects of various size (Mie 1908). The size of atmospheric aerosol particles ranges from a few nanometers to several micrometers. Thus, these particles are very effective scatterers of electromagnetic waves with wavelengths from the ultraviolet (UV) to the infrared (IR) (van de Hulst 1957, Bohren and Huffman 1983). The interaction of light with air molecules that are much smaller than the wavelength of light ($r \ll \lambda$) is called Rayleigh scattering. This process is strongly wavelength-dependent (proportional to λ^{-4}). The blue sky is caused by Rayleigh scattering because the blue part of the visible spectrum is scattered much stronger than light of larger wavelength.

For most scattering processes the energy and wavelength of the scattered photon are equal to those of the incident photon. This is called elastic scattering. For a very small

fraction of scattered light a wavelength shift between incident and scattered photon can be observed. This inelastic Raman scattering is caused by an excitation or disexcitation of the scattering molecule by incident photons changing its vibrational, rotational, or vibrational-rotational level of energy.

2.2 Active remote sensing with aerosol lidar

2.2.1 Lidar principle

A lidar (Light Detection and Ranging, Weitkamp 2005) instrument uses laser light for range-resolved measurements of aerosols, clouds, trace gasses, temperature, or winds with high temporal resolution. A lidar consists of a transmitter and a receiver (Wandinger 2005a). The transmitter includes a laser that emits short pulses which are directed into the atmosphere. The light source of a common aerosol lidar is a commercially available Nd:YAG laser that emits light at the fundamental wavelength of 1064 nm. The emitted light can be frequency-doubled to 532 nm or frequency-tripled to 355 nm. The receiver telescope collects backscattered light that is directed through a beam separation unit after which light at different wavelength and state of polarization is detected by means of photomultiplier tubes. Because the speed of light c is known, the distance R between the lidar and the location of scattering can be calculated as $R = ct/2$. The detected signal is described by the lidar equation

$$P_{\lambda_0}(R) = E_{\lambda_0} \frac{O_{\lambda_0}(R)}{R^2} \beta_{\lambda_0}(R) \exp\left[-2 \int_0^R \alpha_{\lambda_0}(\xi) \mathrm{d}\xi\right]. \tag{2.3}$$

The range-resolved received power $P_{\lambda_0}(R)$ at the emitted wavelength λ_0 depends on a constant, range-independent system term E_{λ_0} (that considers the emitted laser pulse power and length, the speed of light, the area of the receiver telescope, and the wavelength-dependent transmission of the receiver optics), the geometric form factor $O_{\lambda_0}(R)$, the inverse square distance, the wavelength-dependent volume backscatter coefficient $\beta_{\lambda_0}(R)$ at the place of backscattering, and a transmission term that is expressed by an exponential function. The latter describes the attenuation of light on the way to the place of scattering and back. The function $O_{\lambda_0}(R)$ characterizes the geometric overlap between the laser beam and the receiver field of view. It varies between zero near the lidar and unity at a height of complete overlap beyond which its effect does no longer need to be accounted for.

A comprehensive introduction into the principles of active remote sensing with lidar and an overview of different lidar techniques is provided by Wandinger (2005a, b), Ansmann and Müller (2005), Eloranta (2005) and Sassen (2005).

2.2.2 Measured parameters

Particle backscatter and extinction coefficient
On the way from the emitting laser to the location of scattering and back to the lidar receiver, photons can be absorbed or scattered. The sum of absorption and scattering describes the attenuation of light travelling through a medium and is called extinction. In the atmosphere emitted laser light can interact with molecules and particles. Thus, the volume backscatter

coefficient β (in $m^{-1}sr^{-1}$) and the volume extinction coefficient α (in m^{-1}) need to be split into contributions of particles (superscript p) and molecules (superscript m) as

$$\beta_\lambda(R) = \beta_\lambda^p(R) + \beta_\lambda^m(R) = \int n^p(R,r)\frac{d\sigma_{sca}^p(r,\pi)}{d\Omega}dr + n^m(R)\frac{d\sigma_{sca}^m(\pi)}{d\Omega} \tag{2.4}$$

and

$$\alpha_\lambda(R) = \alpha_\lambda^p(R) + \alpha_\lambda^m(R) = \int n^p(R,r)\sigma_{ext}^p(r)dr + n^m(R)\sigma_{ext}^m. \tag{2.5}$$

$n^p(r)$ (in $m^{-3}m^{-1}$) denotes the number concentration of aerosol particles of a certain size while n^m (in m^{-3}) refers to the number concentration of air molecules. $d\sigma_{sca}^{p,m}(\pi)/d\Omega$ represents the differential scattering cross section (in m^2sr^{-1}) of particles and molecules for the backward direction ($\Theta = \pi$). The extinction cross section (in m^2) of particles and molecules is characterized as $\sigma_{ext}^{p,m}$. The differential scattering cross section is known for different molecules. Profiles of the number concentration $n^m(R)$ of air molecules can be derived from profiles of temperature and pressure originating from radiosonde ascents or standard atmospheric models (Bucholtz 1995). Both $\beta^p(R)$ and $\alpha^p(R)$ are extensive quantities that increase with increasing particle concentration in the atmosphere.

Particle lidar ratio
In the past, lidar instruments were set up to detect light only at the wavelength of the emitted laser light. This complicated the data analysis as two unknown quantities, $\beta(R)$ and $\alpha(R)$, appear in Eq. (2.3) while only one signal is being detected. Klett's method (Klett 1981, 1985, Fernald 1984) is used to infer quantitative aerosol information from such elastic backscatter lidar measurements (Ansmann and Müller 2005). Because $\beta(R)$ and $\alpha(R)$ cannot be retrieved independent of each other, extinction-to-backscatter ratios (or lidar ratios)

$$S^p(R) = \frac{\alpha^p(R)}{\beta^p(R)} \tag{2.6}$$

and

$$S^m = \frac{\alpha^m(R)}{\beta^m(R)} \approx \frac{8\pi}{3}\,\text{sr} \tag{2.7}$$

for particles and molecules, respectively, are introduced to substitute one of the two unknowns. The molecular lidar ratio S^m is constant with height. The particulate lidar ratio $S^p(R)$ on the other hand is an intensive parameter that depends on the size, shape, and refractive index of the scattering particles. For the analysis of signals of an elastic backscatter lidar a reasonable value of $S^p(R)$ needs to be assumed. In cases of complex aerosol stratification with layers of different origin, $S^p(R)$ can show strong vertical variations which can introduce large errors to the retrieval of $\beta^p(R)$ and $\alpha^p(R)$ (Sasano et al. 1985). Typical values of lidar ratios for common aerosol types are presented in Section 2.2.3.

The limitations of the early elastic backscatter lidars have been overcome by new techniques that enable the measurement of a second signal to solve Eq. (2.3) without the need for assuming a particle lidar ratio. This pure molecular signal can be obtained either with a Raman channel (Ansmann and Müller 2005, Wandinger 2005b) for the detection of Raman scattering by nitrogen combined with the known nitrogen concentration in the atmosphere or with a high-spectral-resolution channel (Eloranta 2005) that measures the Doppler broadening of the Cabannes line. Such channels can provide the independent information needed to calculate $\beta^p(R)$ and $\alpha^p(R)$, and thus, to get a direct measurement of $S^p(R)$.

Particle linear depolarization ratio

The polarization lidar technique (Sassen 2005) makes use of the fact that the linearly polarized laser light emitted by a lidar might change its state of polarization when interacting with scatterers in the atmosphere. To quantify this change in the state of polarization, backscattered light is measured in two detection channels representing two planes of polarization, parallel ($\parallel$) and perpendicular ($\perp$) with respect to the plane of polarization of the emitted laser light. This leads to two lidar equations for backscattered light that has the same state of polarization as the emitted laser light (co-polarized, $^{\parallel}P_\lambda(R)$) and for light whose state of polarization is perpendicular to the one of the emitted laser light (cross-polarized, $^{\perp}P_\lambda(R)$). The ratio of these two signals is referred to as the linear volume depolarization ratio (Schotland et al. 1971), that comprises the contributions of molecules and aerosol particles as

$$\delta^{\mathrm{v}} = \frac{^{\perp}P}{^{\parallel}P} = \frac{^{\perp}\beta}{^{\parallel}\beta} = \frac{^{\perp}\beta^{\mathrm{p}} + {}^{\perp}\beta^{\mathrm{m}}}{^{\parallel}\beta^{\mathrm{p}} + {}^{\parallel}\beta^{\mathrm{m}}} \; . \tag{2.8}$$

A separation of the backscatter coefficients related to molecules and particles leads to the linear molecular (Rayleigh) depolarization ratio

$$\delta^{\mathrm{m}} = \frac{^{\perp}\beta^{\mathrm{m}}}{^{\parallel}\beta^{\mathrm{m}}} \tag{2.9}$$

and the linear particle depolarization ratio

$$\delta^{\mathrm{p}} = \frac{^{\perp}\beta^{\mathrm{p}}}{^{\parallel}\beta^{\mathrm{p}}} \; . \tag{2.10}$$

From Eqs. (2.9) and (2.10), the equation for the calculation of δ^{p} from the measured lidar profiles of β^{p} and δ^{v} is derived as

$$\delta^{\mathrm{p}} = \frac{\beta^{\mathrm{m}}(\delta^{\mathrm{v}} - \delta^{\mathrm{m}}) + \beta^{\mathrm{p}}\delta^{\mathrm{v}}(1 + \delta^{\mathrm{m}})}{\beta^{\mathrm{m}}\,(\delta^{\mathrm{m}} - \delta^{\mathrm{v}}) + \beta^{\mathrm{p}}\,(1 + \delta^{\mathrm{m}})} \; . \tag{2.11}$$

Like the particle lidar ratio, the particle linear depolarization ratio is an intensive quantity of the ensemble of scattering particles. Accurate measurements of this parameter require regular calibration measurements as well as a thorough characterization of the lidar receiver optics (Freudenthaler et al. 2009, Freudenthaler 2016, Mattis et al. 2009, Bravo-Aranda et al. 2016, Belegante et al. 2018). Typical values of particle linear depolarization ratios for common aerosol types are presented in Section 2.2.3.

Ångström exponent

Measurements of aerosol optical properties at different wavelengths allow for calculating the spectral slope of those parameters. This information is described by the Ångström exponent $\mathring{a}$ (Ångström 1964). For a quantity ξ, which could be α^{p}, β^{p}, or S^{p}, measured at the two wavelengths λ_1 and λ_2, the Ångström exponent is calculated as

$$\mathring{a}^{\xi}_{\lambda_1/\lambda_2} = \frac{\ln\left(\xi_{\lambda_1}/\xi_{\lambda_2}\right)}{\ln\left(\lambda_2/\lambda_1\right)} \; . \tag{2.12}$$

2.2.3 Aerosol typing

Modern multiwavelength polarization Raman lidars use high-power Nd:YAG lasers to emit light at two or three of the wavelengths of 355, 532, and 1064 nm. The measured profiles

Table 2.1: Typical values for common aerosol types discerned from advanced aerosol lidar measurement as provided in Müller et al. (2007), Burton et al. (2012), Groß et al. (2013), Haarig et al. (2017a, b, 2018).

Aerosol type	S^{p} (sr)		δ^{p}		
wavelength (nm)	355	532	355	532	1064
marine	20	20	0.03	0.02	0.02
Saharan dust	55	55	0.25	0.32	0.23
smoke	40–50	50–70	0.02	0.05	0.01
urban	50–60	40–70	0.04	0.06	–
polluted dust	70–80	60–80	0.12–0.22	0.12–0.27	–
volcanic ash	60	60	0.37	0.36	–

of β^{p} at 355, 532, and 1064 nm, of α^{p} at 355 and 532 nm, and of δ^{v} at one or more of the emitted wavelengths can be used to calculate optical aerosol parameters that are sensitive to size, shape, and refractive index of atmospheric particles. These parameter can refer to the concentration or the type of the scattering particles, and thus, give extensive information about the measured clouds and aerosols that can be used for comprehensive aerosol characterization. Typical values for commonly considered aerosol types are given in Table 2.1.

The lidar ratio gives information about the size, shape, and the absorption properties of the scattering particles. It decreases with particle size and increases with particle absorption efficiency. Typically, non-spherical particles have higher lidar ratios than spherical particles of the same size. The different effects might compensate each other which leads to similar lidar ratios for totally different particle types. For instance, lidar ratios of urban haze (small and highly absorbing) and mineral dust (large, non-spherical, and less absorbing) are similar with values of 50–55 sr (Ackermann 1998, Müller et al. 2007, Tesche et al. 2009a). In such ambiguous cases the shape-dependent particle linear depolarization ratio provides further insight. Scattering by spheres does not alter the state of polarization of light. Thus $\delta^{\mathrm{p}}_{\lambda} \approx 0$ for spherical particles and increases with particle non-sphericity as well as for mixtures of spherical and non-spherical particles. Ångström exponents of zero denote wavelength independence of the investigated quantity which is due to scattering by large particles. Scattering by small particles on the other hand shows a strong wavelength dependence and causes values of $\mathring{a}$ that are larger than unity (Eck et al. 1999). This information is combined to create lidar-based aerosol-typing schemes (Burton et al. 2012, 2013, Groß et al. 2013) that are also of vital importance for the analysis of data from spaceborne lidars (Omar et al. 2009, Illingworth et al. 2015, Wandinger et al. 2016) which generally lag the sophistication of ground-based state-of-the-art instruments.

2.2.4 Aerosol-type separation

The first separation of aerosol types based on lidar measurements of δ^{p} is presented by Sugimoto et al. (2003) and Shimizu et al. (2004). This method has been further refined by Tesche et al. (2009b) with the increased availability of precise measurements of δ^{p} together with measurements of this parameter for aerosol types in their pure, unmixed form. The technique is similar to the one used for separating the contributions of molecules and parti-
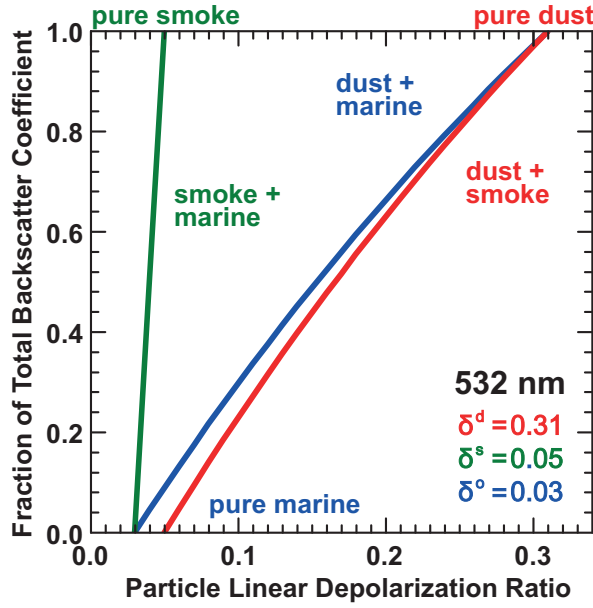
Figure 2.1: Visualization of Eq. (2.14) for two-component mixtures of mineral dust ($\delta^{\mathrm{d}} = 0.31$), biomass–burning smoke ($\delta^{\mathrm{s}} = 0.05$), and marine aerosol ($\delta^{\mathrm{o}} = 0.03$) at 532 nm.

cles to the volume depolarization ratio to obtain Eq. (2.11). The particle depolarization ratio is assumed to contain contributions of mineral dust (superscript d) and less depolarizing aerosols (superscript nd for non-dust). Similarly to Eq. (2.8), $\delta_\lambda^{\mathrm{p}}$ can be rewritten as

$$\delta_\lambda^{\mathrm{p}} = \frac{^{\perp}\beta_\lambda^{\mathrm{d}} + {}^{\perp}\beta_\lambda^{\mathrm{nd}}}{^{\parallel}\beta_\lambda^{\mathrm{d}} + {}^{\parallel}\beta_\lambda^{\mathrm{nd}}} \ . \tag{2.13}$$

Following the transformations described in Tesche et al. (2009b) leads to

$$\beta_\lambda^{\mathrm{d}} = \beta_\lambda^{\mathrm{p}} \frac{\left(\delta_\lambda^{\mathrm{p}} - \delta_\lambda^{\mathrm{nd}}\right)\left(1 + \delta_\lambda^{\mathrm{d}}\right)}{\left(\delta_\lambda^{\mathrm{d}} - \delta_\lambda^{\mathrm{nd}}\right)\left(1 + \delta_\lambda^{\mathrm{p}}\right)} \ . \tag{2.14}$$

The dust backscatter coefficient can thus be derived, if $\beta_\lambda^{\mathrm{p}}$ and $\delta_\lambda^{\mathrm{p}}$ of a certain wavelength are measured and $\delta_\lambda^{\mathrm{d}}$ and $\delta_\lambda^{\mathrm{nd}}$ are known. Once $\beta_\lambda^{\mathrm{d}}$ is known from Eq. (2.14) the contribution of the non-dust component can be derived as

$$\beta_\lambda^{\mathrm{nd}} = \beta_\lambda^{\mathrm{p}} - \beta_\lambda^{\mathrm{d}} . \tag{2.15}$$

Figure 2.1 is a visualization of Equation (2.14) for the measurement of two-component mixtures of maritime aerosol + biomass–burning smoke, maritime aerosol + mineral dust, and biomass–burning smoke + mineral dust at 532 nm. The third mixture represents the conditions observed in the elevated layers over Cape Verde during winter (Tesche et al. 2009b, 2011a, b). An investigation of the second aerosol mixture is presented by Groß et al. (2011b). In the following, parameters will refer to particles if not stated otherwise. Hence, the superscript p will be omitted from here on.

The method of Tesche et al. (2009b) has been generalized by Burton et al. (2014) who incorporated the lidar ratio and the Ångström exponent in addition to the particle linear depolarization ratio to obtain simple mixing rules that can be used to infer mixing-ratios from

lidar-derived parameters also for cases of low values of the particle linear depolarization ratio. The aerosol-type separation based on lidar parameters is fundamentally different from approaches that simply cut an assumed aerosol size distribution into a fine and a coarse mode such as *in-situ* measurements or the AERONET retrieval (Eck et al. 2010)). The latter generally ignore the effects of small mineral dust particles in the fine mode or large smoke particles in the coarse mode. The method of Tesche et al. (2009b) also forms the foundation for inferring mass concentration profiles of mineral dust and volcanic ash from polarization lidar measurements (Ansmann et al. 2010, 2011a, 2012).

2.2.5 Dust and ash mass concentrations

The methodology outlined in Section 2.2.4 has been further refined to infer mass concentrations m of the different aerosol types in the mixture (Ansmann et al. 2010, 2011a, 2012, Tesche et al. 2012, Mamouri and Ansmann 2014, 2017). The key to this step away from purely optical information has been the introduction of extinction-to-mass conversion factors v_f/τ_f and v_c/τ_c for the fine- and coarse-mode aerosol types, respectively. These conversion factors are based on sun photometer observations at sites representative for different aerosol types (Ansmann et al. 2010, 2011a, 2012). The latest, most comprehensive, and regionally resolved collection of such conversion factors is provided in Ansmann et al. (2019a).

After using Eq. (2.14) to separate non-spherical coarse-model aerosol from spherical fine-mode aerosol, the mass-concentration profile for the coarse-mode aerosol type can be derived as

$$m_c = \rho_c \frac{v_c}{\tau_c} \beta^c S^c = \rho_c \frac{v_c}{\tau_c} \alpha^c \tag{2.16}$$

while that of the fine-mode aerosol type can be calculated following

$$m_f = \rho_f \frac{v_f}{\tau_f} \beta^f S^f = \rho_f \frac{v_f}{\tau_f} \alpha^f. \tag{2.17}$$

To obtain the mass-concentration profiles for volcanic ash (index a) and non-ash (index na) particles, Eqs. (2.16) and (2.17) are solved using values of δ^a=0.36±0.02 and δ^{na}=0.01±0.01, respectively. Multiplication with the ash and non-ash lidar ratios of S^a=50±10 sr and S^{na}=40–80 sr, respectively, gives the extinction coefficients corresponding to the two aerosol types. These profiles need to be multiplied with the respective densities (ρ_a and ρ_{na}) and conversion factors (v_a/τ_a and v_{na}/τ_{na}) to yield mass-concentration profiles. In Ansmann et al. (2010), an ash mass density of 2.6 g/cm^{-3} is combined with an ash conversion factor of 0.75×10^{-6} m as representative for mineral dust in the Optical Properties of Aerosols and Clouds (OPAC, Hess et al. 1998) data base. These initial values have been refined to ρ_a=2.6±0.6 g/cm^{-3} and v_a/τ_a=(0.605±0.1)×10^{-6} m in Ansmann et al. (2011a). In addition, values of ρ_a=1.5±0.3 g/cm^{-3} and v_{na}/τ_{na}=(0.177±0.016)×10^{-6} m have been selected for the non-ash fine-mode aerosol in the later stages of studying the Eyjafjallajökull volcanic ash plume (Ansmann et al. 2011a).

Further refinements for ash from the Eyjafjallajökull and Grímsvötn eruptions, for Saharan dust, and for continental aerosol are presented in Ansmann et al. (2012) as the Polarization Lidar Photometer Networking (POLIPHON) technique. This methodology infers realistic ranges of ash mass concentrations also for measurements with less advanced lidar instruments as demonstrated by Tesche et al. (2012) for lidar measurements of the Grímsvötn

Table 2.2: Overview of the equations used to calculate the input parameters for different CCN and INP parametrizations from the aerosol extinction coefficient α related to different aerosol types (index omitted for readability). A comprehensive list of the required conversion factors c and x is provided in Mamouri and Ansmann (2016) and Ansmann et al. (2019a).

	mineral dust	continental pollution	marine aerosol
CCN input	$n_{100,\mathrm{dry}} = c_{100}\alpha^x$	$n_{50,\mathrm{dry}} = c_{60}\alpha^x$	$n_{50,\mathrm{dry}} = c_{100}\alpha^x$
INP input	$n_{250,\mathrm{dry}} = c_{250}\alpha$	$n_{250,\mathrm{dry}} = c_{290}\alpha$	$n_{250,\mathrm{dry}} = c_{500}\alpha$
	$S_{\mathrm{dry}} = c_{\mathrm{s}}\alpha$	$S_{\mathrm{dry}} = c_{\mathrm{s}}\alpha$	$S_{\mathrm{dry}} = c_{\mathrm{s}}/4\alpha$

ash plume over Stockholm, Sweden. In addition, lidar-derived mass concentration profiles of coarse- and fine-mode mineral dust (Mamouri and Ansmann 2014, 2017) provide a useful new tool for assessing dust mobilization and transport modelling (Solomos et al. 2017).

2.2.6 CCN and INP concentrations

Over the years, the POLIPHON technique has been further refined to derive not only mass concentrations from lidar measurements but also the concentrations of particles that are relevant for the formation and development of clouds, i.e. concentrations of cloud condensation nuclei (CCN) and ice nucleating particles (INP) (Mamouri and Ansmann 2016). The key to this development are conversion factors that provide a relation between the aerosol extinction profile for different types of aerosols and the input needed for commonly used parametrizations for inferring CCN and INP concentrations from in-situ measurements of different aerosol types (DeMott et al. 2010, 2015a, 2016, Niemand et al. 2012, Steinke et al. 2015, Ullrich et al. 2017). For different aerosol types such as mineral dust (index d), continental pollution (index c), and marine aerosol (index o), the concentration of particles with dry diameters larger than 100 nm ($n_{100,\mathrm{d,dry}}$) and 50 nm ($n_{50,\mathrm{c,dry}}$, $n_{50,\mathrm{o,dry}}$), respectively, needs to be know to obtain CCN concentrations. Parametrizations for inferring INP concentration are based on either the concentration of particles with dry diameters larger than 250 nm ($n_{250,\mathrm{d,dry}}$, $n_{250,\mathrm{c,dry}}$, and $n_{250,\mathrm{o,dry}}$) or the particle surface area concentration ($S_{\mathrm{d,dry}}$, $S_{\mathrm{c,dry}}$, and $S_{\mathrm{o,dry}}$). These parameters can be obtained from the extinction coefficient related to the respective aerosol types and corresponding conversion factors following the equations in Table 2.2.

The methodology for inferring CCN and INP profiles from lidar measurements marks a paradigm shift in the characterization of aerosols relevant for cloud formation and development. Today, aerosol optical depth (AOD or τ) and aerosol index (AI=$\tau \times \mathring{a}$) as obtained from passive spaceborne remote sensing are still the best proxies of CCN concentration even though their usefulness might be limited (Stier 2016). Even worse, there is currently no remote-sensing based proxy for INP concentrations. Better understanding of aerosol-cloud interactions in warm and cold clouds can only be obtained if the concentrations of CCN and INP are known. Height-resolved observations are the only tool for getting this information. In contrast, proxies based on column-integrated parameters cannot guarantee that the observed aerosols and clouds are actually at the same height level. Cloud droplets are formed when ascending air parcels cool adiabatically until supersaturation over water is reached at cloud base. Cloud glaciation is initiated at cloud top where temperatures are lowest. It is

these two height levels where CCN and INP, respectively, act most efficiently.

2.2.7 Inversion with regularization

The Tikhonov Advanced Regularization Algorithm (TiARA, Müller et al. 2019) uses data from multiwavelength aerosol lidar measurements for the retrieval of microphysical particle properties (Müller et al. 1998, Veselovskii et al. 2002, Ansmann and Müller 2005). This application has been the main driver for the development of advanced multiwavelength aerosol lidars even before the development of the capability for sophisticated aerosol classification. Outputs of TiARA have been thoroughly compared to findings from *in situ* particle sampling (Ansmann et al. 2002b, Wandinger et al. 2002, Müller et al. 2003, 2005, Tesche et al. 2008, Müller et al. 2014, Sawamura et al. 2017). The method has now matured to a level that allows for unsupervised and real-time application to operative multiwavelength aerosol lidar measurements (Chemyakin et al. 2014, Müller et al. 2019).

The relationship between optical and microphysical properties of a population of scattering particles is expressed as a set of Fredholm equations of the first kind which represents an ill-posed, non-linear problem that cannot be solved analytically. The entire inversion procedure is targeted at finding those aerosol number size distributions $n(r)$ that are capable of reproducing the measured optical data. A set of three backscatter and two extinction coefficients, a so-called 3+2 data set, forms the minimum number of input parameters needed to obtain a stable solution (Müller et al. 2001, Veselovskii et al. 2002). It is for this reason that modern aerosol lidars are designed to measure backscatter coefficients at 355, 532, and 1064 nm and extinction coefficients at 355 and 532 nm. Depending on the range and step width of the varied parameters, one input data set can produce hundreds of thousands of mathematical solutions. However, only a fraction of those are physically meaningful results. This necessitates a careful analysis of the inversion output. In the end, several hundred trustworthy solutions are averaged to obtain information on the particle number, surface-area, and volume concentration, the effective radius (r_{eff}) derived from these parameters, the complex refractive index ($m = m_{\mathrm{r}} + im_{\mathrm{i}}$), and the single-scattering albedo (SSA or ω).

The inversion of multiwavelength lidar data is based on using light-scattering kernels that were computed on the basis of Mie theory (Ansmann and Müller 2005). Veselovskii et al. (2010) were the first to investigate the possibility of using spheroid scattering kernels computed for randomly oriented spheroids (Dubovik et al. 2006). This change requires the addition of values of the particle linear depolarization ratio to the set of input data which allows for retrieving the spheroid particle fraction as an additional inversion output parameter. This parameter should be close to unity for measurements under atmospheric conditions in which only non-spherical particles are present.

2.3 Passive remote sensing within AERONET

2.3.1 AERONET sun/sky radiometer observations

The Aerosol Robotic Network (AERONET, Holben et al. 1998, Holben et al. 2001) is a global network of automated radiometers for direct-sun and sky-radiation measurements. Initially

designed as a ground-truth for spaceborne remote sensing, AERONET provides AOD at wavelengths from 340 nm to 1640 nm always including observations at 440, 670, 870, and 1020 nm. The AOD uncertainty is estimated as 0.01 to 0.02 depending on wavelength in the absence of cloud contamination. The calibrated sky radiance measurements typically have uncertainties below 5%. Ångström exponents and the fine-mode fraction (FMF or η, O'Neill et al. 2003) are obtained from the spectral AOD data.

The level 2 product available from the AERONET portal (https://aeronet.gsfc.nasa.gov/) includes inversion results for measurements with a 440-nm AOD larger than 0.4 (Dubovik et al. 2006). The AERONET inversion infers columnar particle properties such as the volume size distribution, the complex refractive index, and the SSA. The uncertainty in SSA is expected to be of the order of 0.03 (Dubovik et al. 2000). Knowledge of SSA is used to determine the fraction of AOD related to light absorption, referred to as absorption aerosol optical depth (AAOD). Detailed information on the AERONET instrumentation and data is provided by Holben et al. (1998), Holben et al. (2001), Dubovik et al. (2002, 2006), Eck et al. (2005), Giles et al. (2019), and Sinyuk et al. (2020).

2.3.2 Retrieval of lidar-specific parameters

Measurements with aerosol lidar and AERONET instruments can be compared to assess the performance of the spheroidal light-scattering model of Dubovik et al. (2006) currently used in the AERONET inversion (Müller et al. 2010a, b, Gasteiger et al. 2011). Such comparisons are of particular interest for aerosol types with non-spherical particle shape (aerosol types with increased δ_λ in Table 2.1) whose light-scattering properties cannot be described by means of Mie theory. Version 3 of the AERONET retrieval added δ_λ and S_λ at 440, 675, 870, and 1020 nm to the list of standard level 2.0 inversion products. The parameter sphericity, which was provided in the AERONET version 2 level 2.0 inversion product, has been discontinued in version 3.

For the retrieval of lidar-specific parameters, the particle size distribution and the refractive index $m = m_{\mathrm{r}} + im_{\mathrm{i}}$ as inferred from the AERONET inversion are used to compute the elements $F_{11,\lambda}(r, m)$ and $F_{22,\lambda}(r, m)$ of the Müller scattering matrix (Bohren and Huffman 1983). The element $F_{11,\lambda}(r, m)$ is proportional to the flux of scattered light in case of unpolarized incident light while $F_{22,\lambda}(r, m)$ strongly depends on the angular and spectral distribution of the radiative intensity. The lidar ratio is computed from the element $F_{11,\lambda}(r, n)$ at the scattering angle of 180° and the concurrently inferred SSA as

$$S_\lambda = \frac{4\pi}{\omega_\lambda F_{11,\lambda}(r, m, 180°)} \,.$$ (2.18)

The calculation of the particle linear depolarization ratio requires knowledge of the elements $F_{11,\lambda}(r, n)$ and $F_{22,\lambda}(r, n)$ at the scattering angle of 180°:

$$\delta_\lambda = \frac{1 - F_{22,\lambda}(r, m, 180°)/F_{11,\lambda}(r, m, 180°)}{1 + F_{22,\lambda}(r, m, 180°)/F_{11,\lambda}(r, m, 180°)} \,.$$ (2.19)

2.3.3 Separation of AOD components in mixed dust plumes

The presence of aerosol mixtures has an even stronger impact on the interpretation of passive remote-sensing data compared to those from active remote-sensing measurements. From the point of view of a column-integrated parameter such as AOD, an aerosol mixture actually refers to two distinct scenarios that can overlap considerably: (i) several aerosol types are present in the same height layer (i.e. a mixed layer as identified in a lidar measurement) or (ii) different types of aerosols are present in distinct, vertically separated layers.

Despite this ambiguity, δ inferred from the AERONET inversion can be used in order to retrieve the AOD and AAOD for dust and non-dust aerosols in mixed dust plumes. This is done by adapting the method of Tesche et al. (2009b) (Section 2.2.4) for application to column-integrated AERONET measurements. Re-arrangement of Eq. (2.14) gives the contribution of dust (R_d) to the particle backscatter coefficient as

$$R_\mathrm{d} = \frac{(\delta - \delta_\mathrm{nd})(1 + \delta_\mathrm{d})}{(\delta_\mathrm{d} - \delta_\mathrm{nd})(1 + \delta)}\,. \tag{2.20}$$

R_d is close to zero for spherical particles such as anthropogenic or smoke particles and increases with increasing dust contribution. The contribution of non-dust is calculated as $R_\mathrm{nd} = 1 - R_\mathrm{d}$.

The ratios R_d and R_nd refer to lidar measurements in the backscatter direction. Application to sun-photometer measurements of column-integrated extinction coefficient therefore requires the use of the total and aerosol-type specific lidar ratios to obtain dust AOD as

$$\tau_\mathrm{d} = \tau R_\mathrm{d} \frac{S_\mathrm{d}}{S}\,. \tag{2.21}$$

The dust contribution to total AOD can now be described by the extinction-related dust ratio

$$\chi_{\mathrm{d},\lambda} = \frac{\tau_{\mathrm{d},\lambda}}{\tau_\lambda} = R_\mathrm{d} \frac{S_\mathrm{d}}{S} \tag{2.22}$$

while the non-dust contribution is defined as $\chi_{\mathrm{nd},\lambda} = 1 - \chi_{\mathrm{d},\lambda}$. Extending the approach to SSA gives the mixing rule

$$\omega_\lambda = \chi_{\mathrm{d},\lambda}\omega_{\mathrm{d},\lambda} + \chi_{\mathrm{nd},\lambda}\omega_{\mathrm{nd},\lambda}\,. \tag{2.23}$$

Re-arranging Eq. (2.23) gives the SSA related to non-dust particles, which in turn can be used to derive the non-dust fraction to AAOD as $AAOD_{\mathrm{nd},\lambda} = (1 - \omega_{\mathrm{nd},\lambda})\tau_{\mathrm{nd},\lambda}$.

It can be assumed that the light-absorbing features of the non-dust part of the aerosol plume are caused primarily by black carbon (BC). However, it has been shown that BC is not an ideal light absorber, i.e. $\omega_{\mathrm{BC},\lambda} \neq 0$, (Bond and Bergstrom 2006, Bond et al. 2013). Thus, $\omega_{\mathrm{BC},\lambda}$ needs to be accounted for to obtain the BC-related AAOD as

$$AAOD_{\mathrm{BC},\lambda} = \tau_{\mathrm{nd},\lambda}(1 - \omega_{\mathrm{nd},\lambda})(1 - \omega_{\mathrm{BC},\lambda}) = AAOD_{\mathrm{nd},\lambda}(1 - \omega_{\mathrm{BC},\lambda})\,. \tag{2.24}$$

Finally, the AAOD of dusty mixtures can be described as

$$AAOD = (1 - (\chi_{\mathrm{d},\lambda}\omega_{\mathrm{d},\lambda} + \chi_{\mathrm{nd},\lambda}\omega_{\mathrm{nd},\lambda}))\tau\,. \tag{2.25}$$

In case of $\chi_\mathrm{d} = 1$, all absorption is caused by mineral dust. As the contribution of dust to the mixture decreases, the overall AAOD increases as a result of the stronger absorption of
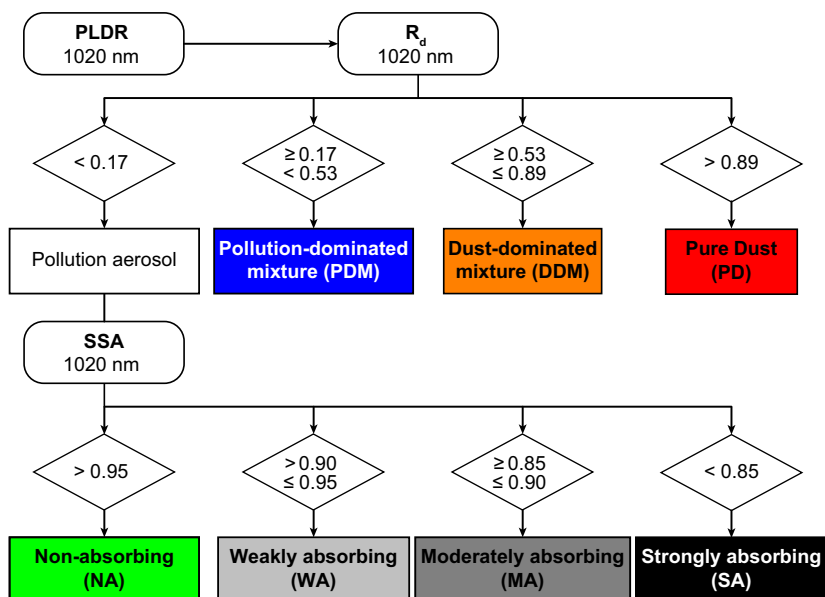
Figure 2.2: Flowchart of the aerosol classification based on R_d and ω_{1020}. The figure is taken from Shin et al. (2019b).

the non-dust particles. The ratio between $AAOD_{nd}$ and total AAOD changes linearly with χ_d in case of equal values of ω_{nd} and ω_d. The relation becomes increasingly non-linear with increasing difference in the absorbing properties of the dust and non-dust particles. This means that total AAOD as provided by AERONET for dusty mixtures is likely to represent the non-dust component at larger wavelengths, where dust is less absorbing, while its interpretation is less ambiguous at shorter wavelengths.

2.3.4 Aerosol typing using lidar parameters

Passive remote-sensing measurements are typically used to classify atmospheric aerosols into four major types according to their size and light-absorbing property. For instance, Lee et al. (2010) used FMF and SSA from the AERONET version 2 level 2.0 inversion products to classify aerosols into absorbing aerosols, mineral dust, non-absorbing particles, and mixed particles. Mineral dust predominately consists of coarse-mode particles, whereas combustion-produced particles are predominantly found in the fine mode. FMF or fine-mode AOD, when used as proxy for identifying non-dust aerosols (Schuster et al. 2006, Lee et al. 2010, Giles et al. 2012), can lead to a systematic overestimation of the contribution of non-dust particles to the total aerosol plume (Shin et al. 2019a) as non-spherical dust particles might also be present in the fine mode (Mamouri and Ansmann 2014, 2017). Sensitivity to particle shape as included in the ratio R_d is hence more important than sensitivity to particle size for quantifying the contribution of mineral dust to mixed dust plumes. After inferring the dust contribution, SSA can be used for a subsequent separation of different types of pollution depending on the respective light-absorbing properties.

Figure 2.2 provides a flowchart of the corresponding aerosol classification method. The contribution of dust in the aerosol mixture is determined based on thresholds of R_d. Pollution particles are defined as showing $R_d < 0.17$ (equivalent to $\delta_{1020} < 0.06$) and mineral dust

as showing $R_{\rm d} > 0.89$ (equivalent to $\delta_{1020} > 0.28$). Values of $R_{\rm d}$ between 0.17 and 0.89 are considered to represent mixtures of mineral dust and pollution aerosols. A threshold of $R_{\rm d} = 0.53$ (equivalent to $\delta_{1020} = 0.16$) is used to further separate between pollution-dominated mixed aerosol (PDM, $R_{\rm d} = 0.17-0.53$) and dust-dominated mixed aerosol (DDM, $R_{\rm d} = 0.53 - 0.89$). The light-absorbing properties and size of PDM is likely to be closer to the characteristics of pollution particles than to DDM. In the same way, the light absorbing properties and size for DDM are more likely to resemble the characteristics of pure dust.

SSA at 440 nm is usually used to identify dust particles (Kim et al. 2007, Lee et al. 2010). This classification uses SSA at 1020 nm as mineral dust and non-dust particles have already been identified based on $R_{\rm d}$. This allows for exploiting the stronger contrast in the SSA of BC and mineral dust at 1020 nm compared to 440 nm. Different absorbing particle types and their mixtures can then be identified based on threshold values adapted from Lee et al. (2010): weakly absorbing (WA, $\omega_{1020} = 0.90 - 0.95$), moderately absorbing (MA, $\omega_{1020} = 0.85 - 0.9$), and strongly absorbing (SA, $\omega_{1020} < 0.85$). For reference, biomass-burning aerosol generally contains a larger fraction of BC (and often brown carbon as well) compared to anthropogenic aerosol, and thus, is likely to fall into the more absorbing categories.

3 Main findings of the included papers

The papers included in this habilitation thesis have been arranged into four themes that describe (i) the evolution of the use of lidar data from focussing on aerosol optical properties to providing parameters of use for the wider scientific community (**Theme 1, Papers I-V**), (ii) the validation of spaceborne lidar data and their use in innovative research (**Theme 2, Papers VI-IX**), (iii) the progress in the inversion of multiwavelength aerosol lidar data for the retrieval of microphysical properties (**Theme 3, Papers X-XI**), and (iv) the use of lidar-specific parameters in the analysis of sun-photometer measurements (**Theme 4, Papers XII-XIV**). This chapter gives an overview of the four themes and summarizes key findings.

3.1 From optical properties to number and mass concentrations

It is only since about the middle of the first decade of this century that the lidar technique has left the niche of a rather small, instrument-focussed group and started to make its full capability available to the wider scientific community. This can be connected to the combined effect of three developments. Most importantly, advances in laser technology and optical elements allowed for a strong decrease in the cost of lidar instruments up to the point of customizable commercially available systems (e.g. Engelmann et al. (2016) or www.raymetrics.com). At the same time, a strong effort was made towards the homogenization and quality-assurance of the products being available from those instruments (Pappalardo et al. 2014, D'Amico et al. 2015, Wandinger et al. 2016). Finally, the first long-term aerosol lidar in space (Winker et al. 2010) now provides a global data set that demonstrates the potential of lidar measurements and opens new pathways for their exploitation.

Within this environment, the eruption of the Eyjafjallajökull volcano on Iceland on 14 April 2010 introduced a new challenge to lidar operators. Suddenly, ground-based lidar observations were an exclusive source of information about the atmospheric concentration of volcanic ash and the dispersion of the ash plume. However, stakeholder such as the Volcanic Ash Advisory Centre (VAAC) in London were not familiar with using the optical parameters inferred from the lidar measurements to assess the potential threat of atmospheric volcanic ash concentrations to aviation safety. This background motivated a further development of lidar-based aerosol-type separation methodologies (Tesche et al. 2009b, 2011b, Tesche 2011) towards the retrieval of mass-concentration profiles of volcanic ash (**Paper I:** Ansmann et al. (2010) and **Paper II:** Ansmann et al. (2011a)) from lidar measurements of optical aerosol properties. The same methodology has also been applied in the aftermath of the eruption of Grímsvötn in May 2011 (**Paper III:** Tesche et al. (2012)). After the generalization for the retrieval of mass concentrations of fine- and coarse-mode particles (**Paper IV:** Ansmann et al. (2012); Mamouri and Ansmann (2014, 2017)), the methodology has been refined even further to infer profiles of the concentration of cloud-condensation nuclei (CCN) and ice nucleating particles (INP) from ground-based lidar measurements (Mamouri and
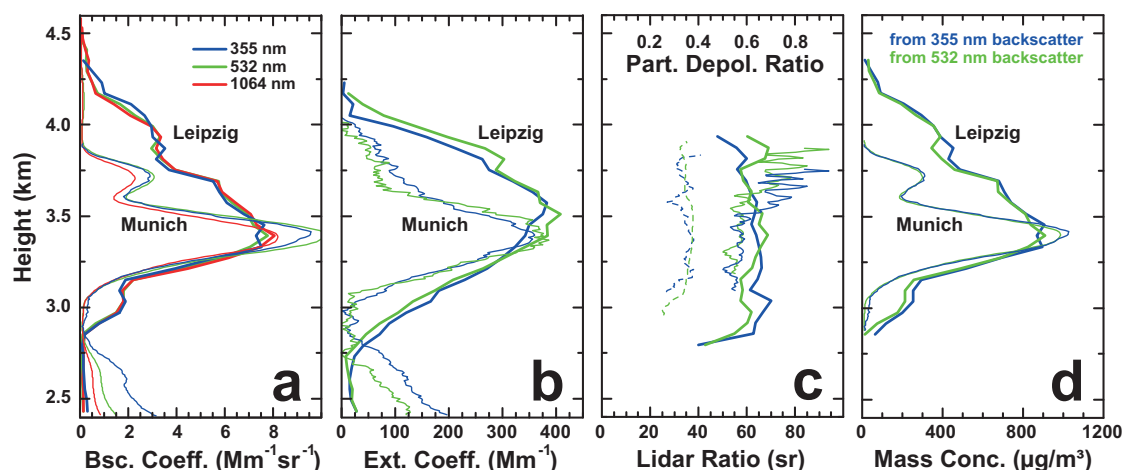
Figure 3.1: (**a**) Backscatter coefficient at 355 (blue), 532 (green), and 1064 nm (red), (**b**) extinction coefficient, (**c**) lidar ratio (Munich, thin lines, Leipzig, thick lines) and particle linear depolarization ratio (Munich, thin dashed lines) at 355 and 532 nm, and (**d**) mass concentration estimates. Profiles refer to cloud-screened averages from 1415 to 1530 UTC on 16 April 2010 at Leipzig and from 0140 to 0230 UTC on 17 April at Munich. The Figure has been adapted from Ansmann et al. (2010).

Ansmann 2015, 2016). A comparison to independent *in-situ* measurements during a field experiment on Cyprus demonstrated the potential of this newly developed capability of active remote sensing with lidar from both ground and space (**Paper V:** Marinou et al. (2019)).

3.1.1 Dust and ash mass concentration profiling

Estimates of the atmospheric concentration of minerals dust during the European airspace closure in the aftermath of the Eyjafjallajökull eruption on 14 April 2010 were of crucial importance for assessing the risk to aviation. At that time, critical exposure levels for the safe operation of aircraft jet engines had been up to debate and underwent revisions almost on a daily basis upon increased pressure from the aviation industry. An example for the observation of the Eyjafjallajökull volcanic ash plume measured at Leipzig on 16 April 2010 and at Munich on 17 April 2010 is shown in Figure 3.1. Values of $\delta_{532} > 0.30$ in the layer of increased backscatter and extinction coefficient between 3.0 and 4.0 km height indicate the presence of non-spherical particles. Backward trajectories show a direct transport pathway from Iceland to Leipzig and Munich. In addition, dispersion modelling shows that the ash plume experienced only marginal amounts of dilution during the two-day transport period to Germany (Vogel et al. 2014). The ash mass concentrations of as much as $1.0 \, \text{mg/m}^3$ presented in Figure 3.1d and Ansmann et al. (2010) were among the first objective estimates of the atmospheric concentration of volcanic ash from the Eyjafjallajökull eruption.

3.1.2 CCN and INP concentration profiling

Over the last decade, great efforts were made to observe mineral dust with both advanced lidar and airborne *in-situ* instruments. The thus obtained data provide an ideal foundation for testing the lidar-based INP retrieval for mineral dust (Mamouri and Ansmann 2016, Ansmann
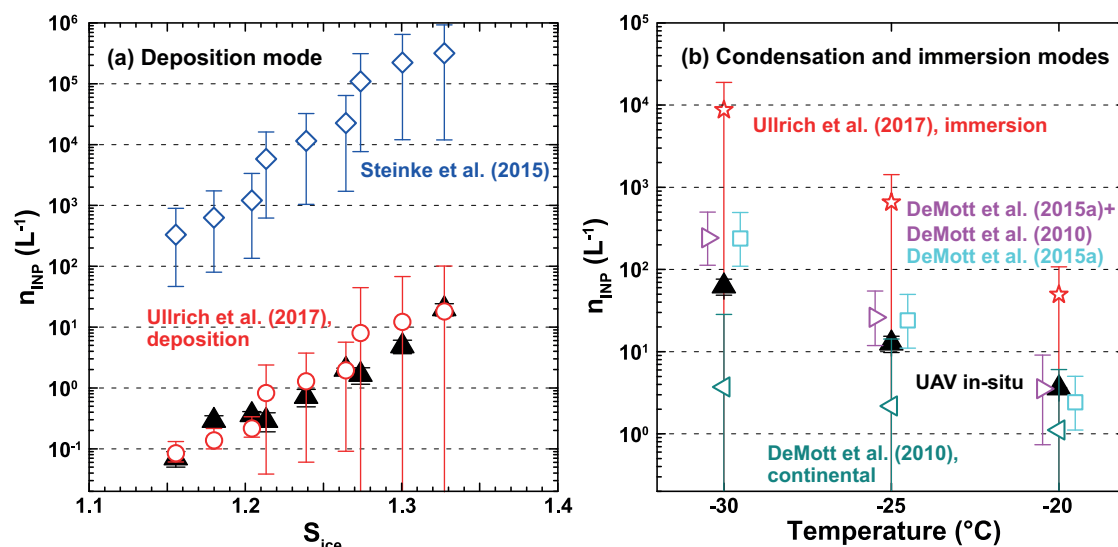
Figure 3.2: INP concentrations (n_{INP}) during pure-dust conditions as estimated from spaceborne CALIPSO lidar measurements on 21 April 2016 (colored symbols for different parametrizations) and UAV-FRIDGE measurements (black triangles) for (**a**) deposition freezing as a function of saturation over ice and (**b**) condensation and immersion freezing as a function of temperature. The dust-related n_{INP} following the immersion parametrization of Ullrich et al. (2017) are based on $S_{\mathrm{d,dry}}$. DeMott et al. (2015a) uses $n_{250,\mathrm{d,dry}}$ as input. The continental-related n_{INP} following De-Mott et al. (2010) are based on $n_{250,\mathrm{c,dry}}$. The values of DeMott et al. (2015a)+DeMott et al. (2010) refer to the total concentration for summing up DeMott et al. (2015a) for mineral dust and DeMott et al. (2010) for continental pollution. The Figure has been adapted from Marinou et al. (2019).

et al. 2019a, ?, Haarig et al. 2019). Marinou et al. (2019) present a particularly comprehensive case study during an experimental campaign at Cyprus in April 2016 in which *in-situ* measurements with an optical particle counter (OPC) aboard an unmanned aerial vehicle (UAV, Mamali et al. 2018) and results of the analysis of collected particles with the FRankfurt Ice nucleation Deposition freezinG Experiment (FRIDGE, Schrod et al. 2016, 2017) INP counter are used to evaluate the accuracy of both the $n_{250,\mathrm{d,dry}}$ and n_{INP} inferred from ground-based and spaceborne lidar measurements.

In the first step of assessing the lidar-based INP retrieval, Marinou et al. (2019) investigate if the lidar-derived concentrations of dry particles with radii larger than 250 nm agree with values obtained from coincident UAV-OPC *in-situ* measurements at the same height levels. For the majority of cases, it is found that *in-situ* observations and remote-sensing estimates of $n_{250,\mathrm{d,dry}}$ are in agreement within their uncertainty ranges (not shown).

In the second step, samples collected with the UAV on 5, 15, and 21 April 2016 and analysed for INP concentrations in the FRIDGE chamber have been used to assess the lidar-based n_{INP}. Figure 3.2 shows the n_{INP} on 21 April as calculated from spaceborne CALIPSO lidar observations and measured from the UAV-FRIDGE samples, for deposition nucleation and for condensation and immersion freezing. Single-particle analysis with scanning electron microscope of the *in-situ* sample collected on 21 April has shown that 99% of the particles were mineral dust (Schrod et al. 2017). This sample was hence used to evaluate the performance of the n_{INP} lidar estimates in a pure-dust case, where (i) the errors originating from separating the extinction profile in dust and non-dust aerosol components are small (about 30%) and (ii) the uncertainties induced from the parametrizations of De-
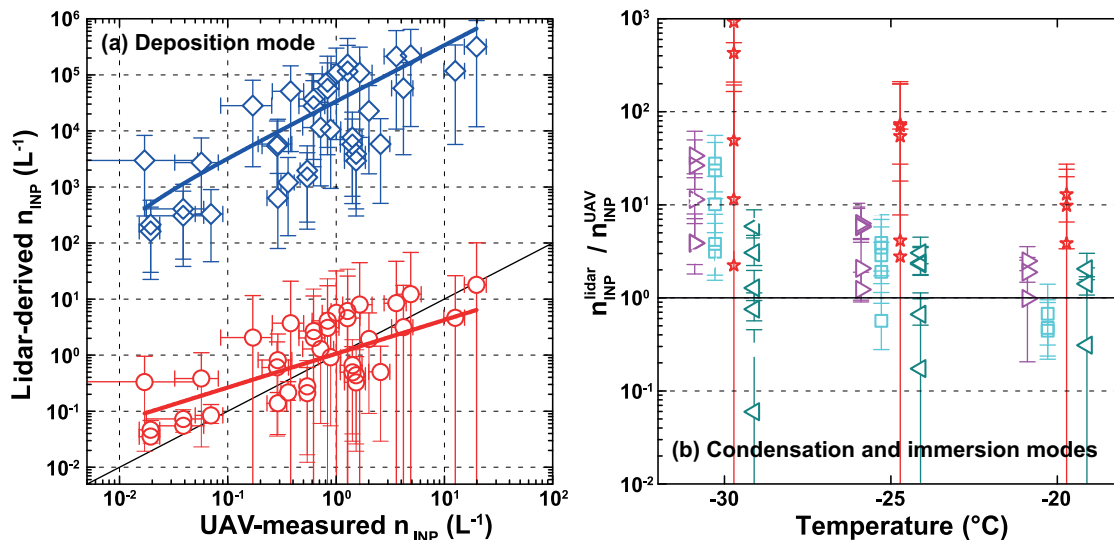
Figure 3.3: Comparison of INP concentrations derived from the CALIPSO and PollyXT lidar observations and UAV-FRIDGE measurements for **(a)** deposition freezing and **(b)** condensation and immersion freezing for cases in the presence of mineral dust and continental aerosol. Colours and symbols refer to the used parametrization. The line in **(a)** marks the $1:1$ line. The colour coding is the same as in Figure 3.2. The Figure has been adapted from Marinou et al. (2019).

Mott et al. (2010) and Ullrich et al. (2017) are minimal. The *in-situ* samples were analysed at –20°C, –25°C, and –30°C. For the investigation of deposition nucleation, samples have been analysed at RH$_w$ of 95%, 97%, and 99% leading to three values of S_{ice} for each temperature (1.16, 1.18, and 1.23 for –20°C; 1.21, 1.24, and 1.26 for –25°C; and 1.27, 1.30, and 1.33 for –30°C). For immersion freezing (Figure 3.2b), samples were analysed at RH$_w$ of 101% giving S_{ice} of 1.23, 1.29, and 1.35 at –20°C, –25°C, and –30°C, respectively. Condensation freezing is associated with RH$_w$ = 101% and S_{ice} = 1.23 at T = –20°C.

Figure 3.3 presents scatter plots of lidar-estimated n_{INP} against the *in-situ* measurements for deposition nucleation as well as condensation and immersion freezing. In contrast to Figure 3.2, this data set also includes cases with mixtures of dust and continental aerosols. In dust and continental cases, 97% of all lidar-derived n_{INP} are within the error bars of the *in-situ* measurements and within a factor of 10 around the 1:1 line when using the deposition freezing parametrization of Ullrich et al. (2017). The n_{INP} sampled with the UAV ranged between 0.02 and 20 L^{-1}. Applying the parametrization of Steinke et al. (2015) to the lidar measurements would lead to n_{INP} values that are 3 to 5 orders of magnitude larger than the *in-situ* measurements in both dust and dust-continental scenarios.

Figures 3.2b and 3.3b show that the lidar-derived n_{INP} using DeMott et al. (2015a) for dust and DeMott et al. (2010) for continental particles agree with the *in-situ* observations within the respective uncertainties for the samples analysed at –20°C and –25°C. The best n_{INP} agreement is found for the pure-dust sample analysed under condensation-freezing conditions of –20°C: *in-situ* measurements of 3.6±0.1 L^{-1} compared to lidar-derived estimates of 3.8 L^{-1} (2.4 L^{-1} related to dust, 1.4 L^{-1} related to non-dust aerosol). Considering all the dust and continental cases for samples analysed under condensation-freezing conditions in Figure 3.3b, the estimated n_{INP} from combining DeMott et al. (2015a) for dust and DeMott et al. (2010) for continental pollution are no more than 2.5 times higher than the *in-situ* measurements. Larger differences are found at temperatures for which immersion
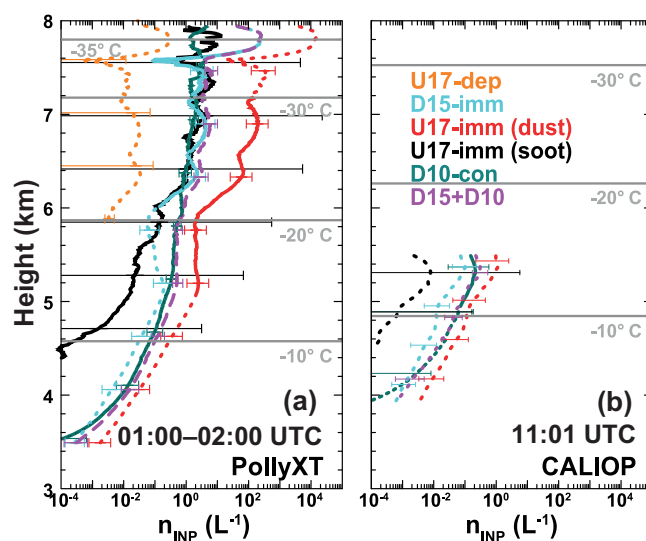
Figure 3.4: INP concentration profiles estimated from the measurements with **(a)** the ground-based PollyXT lidar between 0100 and 0200 UTC on 21 April 2016 and **(b)** the spaceborne CALIOP at 1101 UTC on 21 April 2016. Temperature levels have been taken from re-analysis data. Colours refer to different INP parametrizations. Solid lines mark the temperature range for which the corresponding parametrization has been developed. Dashed lines refer to the extrapolated temperature range. The Figure has been adapted from Marinou et al. (2019).

freezing dominates over condensation freezing as the main INP pathway. In those situations, 1.5–7.0 times larger values are found at –25°C and 4.0–13.0 times larger values are found at –30°C. Overall, in 85% of the analysed cases, the lidar estimates were found to be less than one order of magnitude higher than the UAV measurements of n_{INP}.

The case study of 21 April 2016 in Marinou et al. (2019) not only allows for assessing the feasibility of providing profiles of cloud-relevant aerosol parameters from lidar observations based on independent *in-situ* measurements. During that case, almost the same aerosol situation has been observed with both ground-based (0100–0200 UTC) and spaceborne lidar (1101 UTC). Figure 3.4 shows profiles of n_{INP} derived from the different parametrizations at altitudes between 3 and 8 km. The dust aerosols in the scene contribute to a gradual increase in n_{INP} inside the main dust layer from 0.05 L^{-1} (4.5 km/–10°C) to 0.4 L^{-1} (5.3 km/–14°C) following the parametrization of DeMott et al. (2015a). Then a decrease of 1 order of magnitude is observed up to 6 km (0.06 L^{-1}; –20°C) at the top of the dust layer. Above this altitude, local n_{INP} maxima of 2 L^{-1} (–22°C), 4 L^{-1} (–25°C), and 200 L^{-1} (–33°C) are found at 6.5, 7.0, and 7.9 km, respectively. Use of the immersion freezing parametrization of Ullrich et al. (2017) gives estimates of 60 L^{-1} at –22°C, 200 L^{-1} at –25°C, and 1000 L^{-1} at –33°C. Overall, 91% of the total n_{INP} at altitudes between 6.3 and 8.0 km ($T < $ –21°C) is attributed to dust aerosol. At altitudes between 4.0 and 5.5 km (–6°C to –20°C), only 34% of the total n_{INP} is attributed to dust aerosols (0.06 L^{-1}) while 66% are related to non-dust aerosols (0.12 L^{-1}).

Figure 3.4b shows the n_{INP} derived from CALIPSO lidar observations close to local noon on 21 April 2016. The air temperature increased by 2.7°C to 0.0°C at 3.6 km and –15°C at 5.4 km compared to the ground-based lidar measurements earlier that day. A relatively constant contribution of non-dust particles at these heights with a gradual decrease above 4.6 km is contrasted by a gradual increase in the non-dust n_{INP} with height from 2×10^{-4} L^{-1}

at 4 km (–2°C) to 10^{-2} L^{-1} at 4.4 km (–5°C) to 0.2 L^{-1} at 5.3 km (–12°C) (DeMott et al. (2010) estimates). The dust-related n_{INP} per height are $8{\times}10^{-3}$ L^{-1} at 4 km (–2°C), $3{\times}10^{-3}$ L^{-1} at 4.4 km (–5°C), and 0.1 L^{-1} at 5.3 km (–12°C) according to estimates based on DeMott et al. (2010). Overall, 25% of the total n_{INP} is attributed to dust aerosols and 75% to non-dust aerosols at altitudes between 3.8 and 5.6 km.

3.2 Validation and innovative use of spaceborne lidar data

The CALIPSO lidar (Winker et al. 2009, 2010) is operating since June 2006 and has started a new era for lidar remote sensing of the atmosphere. However, the quality-assurance of the global, decade-long data set of spaceborne lidar observations requires a thorough validation of the provided products on aerosols (**Paper VI:** Tesche et al. 2013) and clouds (**Paper VII:** Achtert and Tesche 2014). In addition, the CALIPSO data set provides the foundation for unprecedented studies that, for instance, enable to bring together height-resolved space-borne aerosol observations with ground-based *in-situ* measurements (**Paper VIII:** Tesche et al. 2014) or provide a view into clouds that could not be studied in the same way with data from passive sensors (**Paper IX:** Tesche et al. 2016).

3.2.1 Validation of CALIPSO level 2 products

CALIOP is an elastic-backscatter lidar and does not allow for a direct measurement of the particle extinction coefficient, which is the parameter of relevance for an assessment of aerosol radiative effects. A priori knowledge of the aerosol type present is essential in the data analysis (see Section 2.2.2). This is a particularly challenging task of an automated re-trieval algorithm and a significant error source. CALIPSO validation studies have dealt with the investigation of the vertical extent of aerosol layers (Liu et al. 2008b, Devasthale et al. 2011) or certain transport regimes and events (Liu et al. 2008a, Ben-Ami et al. 2009), the assessment of feature identification (McGill et al. 2007), and the accuracy of level 1 prod-ucts (Mamouri et al. 2009, Mona et al. 2009, Pappalardo et al. 2010, Rogers et al. 2011). Kittaka et al. (2011) and Redemann et al. (2012) have used observations of the MODerate resolution Imaging Spectroradiometer (MODIS) aboard the Aqua satellite for a global as-sessment of CALIPSO-derived AOD. The initial validation studies of level 2 products (Burton et al. 2010, Kacenelenbogen et al. 2011, Mielonen et al. 2009) were usually performed dur-ing dedicated campaigns or at established lidar sites at mid-latitudes, for example, in the framework of the European Aerosol Research Lidar Network (EARLINET; Pappalardo et al. 2010). These sites are mainly located in urban areas over which complex aerosol mixtures prevail during most of the time. Before Wandinger et al. (2010) and Tesche et al. (2013), little has been known about the performance of the CALIPSO data retrieval in an environment that is dominated by mineral dust or mixtures of dust with other aerosol types.

Measurements with the Backscatter Extinction lidar-Ratio Temperature Humidity Appara-tus (BERTHA) (Althausen et al. 2000, Tesche et al. 2009a) multiwavelength lidar during the second Saharan Mineral Dust Experiment (SAMUM-2) (Ansmann et al. 2011a, Tesche et al. 2011a) at Cape Verde provided the unique opportunity to validate CALIPSO level 2 prod-ucts for mineral dust with ground-based lidar measurements. Tesche et al. (2013) compare
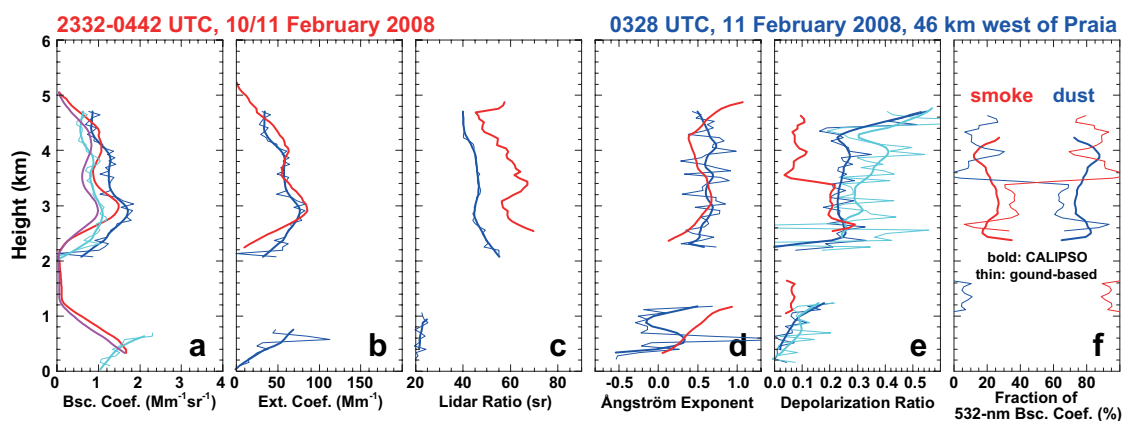
2332-0442 UTC, 10/11 February 2008   **0328 UTC, 11 February 2008, 46 km west of Praia**

Figure 3.5: Height profiles of the backscatter coefficients at (**a**) 532 (red and blue) and 1064 nm (magenta and cyan), the (**b**) extinction coefficient and (**c**) lidar ratio at 532 nm, the (**d**) backscatter-related Ångström exponent for the wavelength pair 532/1064 nm, the (**e**) particle depolarization ratio at 532 nm, and (**f**) relative contributions of dust (blue) and smoke (red) to the 532-nm backscatter coefficient (ground-based: thin) and CALIPSO: bold) as measured with ground-based lidar (red) between 2332 and 0442 UTC on 10/11 February 2008 and CALIPSO (blue) during an overpass at 0328 UTC on 11 February 2008 about 46 km to the west of the lidar site at Praia, Cape Verde. Thin and thick lines denote unsmoothed and smoothed (660 m) profiles, respectively. Particle depolarization ratio profiles measured with BERTHA are compared to the ones given in the CALIPSO level 2 files (cyan in e) and calculated from the total and perpendicularly-polarized backscatter coefficients (dark blue in Figure 3e). The Figure has been adapted from Tesche et al. (2013).

BERTHA measurements at Cape Verde with CALIPSO overpasses at distances of less than 500 km from the ground site. Figure 3.5 shows reasonable agreement between the profiles of both the backscatter and extinction coefficients measured from ground and space. However, there is a clear mismatch of the lidar ratio and the particle linear depolarization ratio. Figure 3.5e shows two CALIPSO-derived δ-profiles: one from the level 2 files and one calculated from the perpendicular and total backscatter coefficients. This comparison revealed a coding error in the CALIPSO data analysis that could be quickly resolved. The difference in the lidar ratio is the result of multiple-scattering effects (Wandinger et al. 2010). The value of 40 sr used in the CALIPSO retrieval during version 2 and 3 actually represents an efficient lidar ratio that accounts for multiple scattering, and consequently, leads to reasonable backscatter coefficients. However, even the revised value of $S_{532}=44\pm9$ sr for mineral dust in the current version 4 of the CALIPSO retrieval (Kim et al. 2018) does not account for the regional differences of this parameter that have been verified over the last decade (Schuster et al. 2012, Mamouri et al. 2013, Nisantzi et al. 2015, Shin et al. 2018).

3.2.2 Validation of CALIPSO PSC classification

Another frontier for the validation of spaceborne lidar measurements are observations of polar stratospheric clouds (PSCs). From the ground, PSCs have been observed only at a handful of Arctic and Antarctic sites. In addition, these observations – as all ground-based lidar measurements – have been performed at the mercy of tropospheric clouds. CALIPSO observations therefore provide the first pole-wide view of both Arctic and Antarctic PSCs. However, the analysis of CALIPSO PSC measurements required the development of a customised classification scheme. Schemes for classifying different types of PSCs from

lidar measurement typically apply the backscatter ratio (ratio of total to molecular backscatter coefficient, R_T) as a measure of the strength of the return signal and δ to quantify the state of polarization of the backscattered light (David et al. 1998, Santecesaria et al. 2001, Adriani et al. 2004, Blum et al. 2005, Massoli et al. 2006, Pitts et al. 2009, 2013).

The purpose of PSC classification is to relate the optical properties of the measured cloud particles to their size, shape, and chemical composition. The first lidar-based classification of Antarctic PSCs (Poole and McCormick 1988) separated between two types of PSC: Type I with $R_T < 5$ and $\delta < 0.05$ and Type II with $R_T > 5$ and $\delta > 0.20$. These findings were in accordance with the theoretical understanding of PSC formation at that time (Toon et al. 1986, Crutzen and Arnold 1986). In the following two decades, lidar-based PSC classification evolved into very elaborate schemes that rank up to six different types and sub-types of PSCs. Type I was split into two subclasses. Type Ia (small R_T, large δ) consists of nitric acid trihydrate crystals (NAT) while Type Ib (large R_T, small δ) is made up of supercooled liquid ternary solutions (STS) that consist of H_2SO_4, HNO_3, and H_2O, and occur at temperatures below 195 K (Peter 1997). Type II PSCs were found to be formed below the ice-frost point and to consists of water ice crystals (Poole and McCormick 1988). In addition to the three traditional PSC types several sub-types of PSC with low to moderate R_T and moderate to high δ have been described in the literature. Type Ia enhanced (Tsias et al. 1999), Type Ic (Tabazadeh and Toon 1996, Toon et al. 2000), Type Id (Stein et al. 1999), NAT rocks (Fahey et al. (2001), Brooks et al. (2003)), or intermediate PSCs with lidar signals ranging between those typical for Types Ia and Ib (David et al. 2005) are expected to consist of the same constituents as the main types but show different scattering characteristics.

The latest generation of the CALIPSO PSC classification scheme employs light-scattering calculations with spherical and non-spherical particles to relate sets of optical parameters to microphysical properties (Pitts et al. 2009, 2013, 2018). A validation of different PSC classification schemes based on a 16-year time series of lidar measurements at Esrange (68°N, 21°E), Sweden, has been presented by Achtert and Tesche (2014). This effort was needed to assess the comparability of different, strongly instrument-dependent PSC climatologies and to harmonise findings from ground-based observations with the CALIPSO PSC data set. Achtert and Tesche (2014) found that PSC classification differs substantially depending on the applied scheme. These discrepancies result from varying threshold values of lidar-derived parameters used to define certain PSC types in the different methods.

Figure 3.6 shows the frequency of PSC types extracted from the 16-year Esrange lidar time series according to seven different classification schemes. The oldest schemes have the biggest problems regarding the number of unclassified cases. A minority of 0.1% to 2.2% of all observations cannot be classified according to the second-generation schemes based on ground-based observations. The CALIPSO scheme leaves no data bin unclassified. Figure 3.6 presents a strong variation in the lidar-based classification of PSC types derived from measurements of ground-based and spaceborne instruments. Publications by the CALIPSO PSC team (P11 and references therein) state that their scheme was designed for spaceborne CALIPSO observations. Consequently, it needs to consider lower signal-to-noise ratio (SNR) and threshold values that are adapted to different horizontal averaging lengths. However, there is no reason why the optical properties of different PSC types should vary when observed from ground and space. Figure 3.6 actually shows that the performance of P11 applied to ground-based lidar measurements is comparable to that of B05 – especially when it comes to the detection of ice PSCs. It is likely that using only
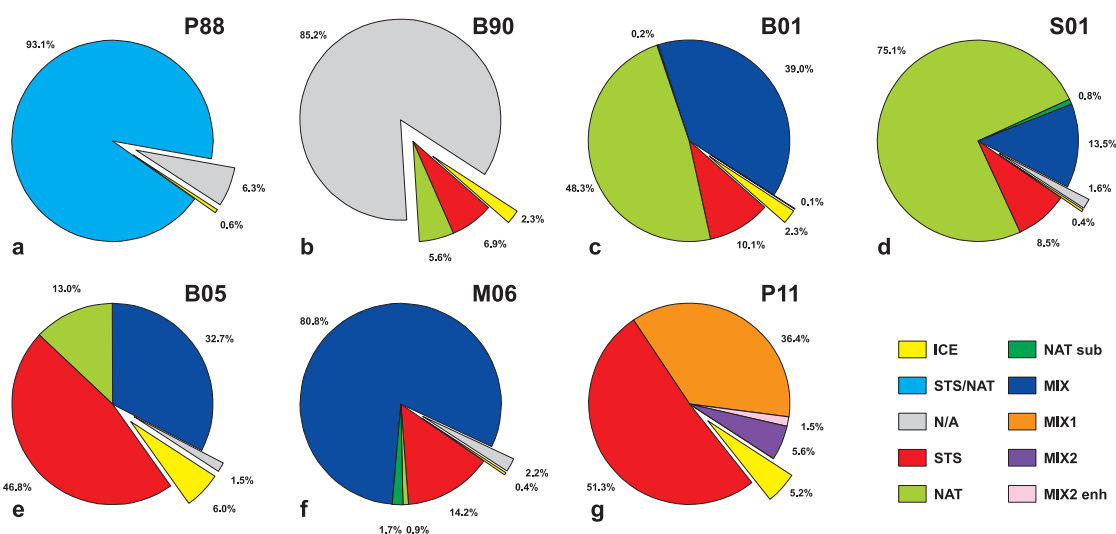
Figure 3.6: Frequency of PSC types extracted from the 16-year Esrange lidar time series according to the seven classification schemes of Poole and McCormick (1988) (P88), Browell et al. (1990) (B90), Biele et al. (2001) (B01), Santecesaria et al. (2001) (S01), Blum et al. (2005) (B05), Massoli et al. (2006) (M06), and Pitts et al. (2011) (P11). The colours refer to different PSC constituents. The exploded parts of the pie charts refer to unclassified (grey), ice (yellow, Type II), and STS and/or NAT (remaining colours, Type Ia, Type Ib, and mixtures) to allow for a comparison of early schemes with later and more detailed ones. Note that STS/NAT (light blue) is only featured in P88; NAT subtype (dark green) is only classified by B01, S01, and M06, while the detailed separation of different MIX classes (orange, purple, and pink) is only incorporated in P11. The Figure has been adapted from Achert and Tesche (2014).

intensive parameters as in the case of aerosol measurements rather than a combination of intensive and extensive scattering properties will enable more reliable PSC classification.

3.2.3 Matching ground-based and spaceborne observations

The large amount of data collected from spaceborne lidar observations, particularly at the poles, together with the possibility to obtain height-resolved information from these measurements enables new studies on combining aerosol observations from ground and space. Tesche et al. (2014) reconcile continuously recorded aerosol extinction coefficients derived from dry *in-situ* measurements with a differential mobility particle sizer (DMPS), a particle soot absorption photometer (PSAP), and an integrating nephelometer (TSI model 3563) at Zeppelin station (78.92 °N, 11.85 °; 475 m above sea level), Ny-Ålesund, Svalbard, that are recalculated to ambient relative humidity, as well as simultaneous ambient observations with the CALIPSO lidar. This represents the first study that compares spaceborne lidar measurements to optical aerosol properties from short-term *in-situ* observations on a case-by-case basis. Finding suitable comparison cases requires an elaborate screening and matching of the CALIOP data with respect to the location of Zeppelin station as well as the selection of temporal and spatial averaging intervals for both the ground-based and spaceborne observations. Reliable reconciliation of these data cannot be achieved with the closest-approach method often used in CALIPSO validation studies. Hence, backward trajectories were used to establish a connection between spaceborne and ground-based observations in the region of interest around Svalbard (0 to 25 °E, 75 to 82 °N) in the considered year of 2008.
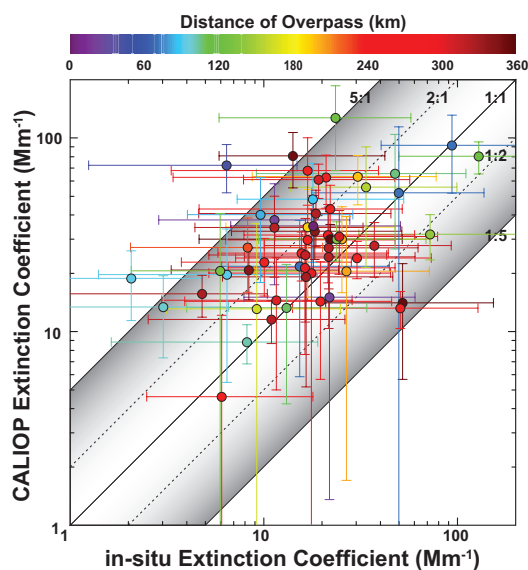
Figure 3.7: Comparison of the ambient 550-nm extinction coefficient from humidification of neph-elometer and PSAP measurements versus the ambient 532-nm extinction coefficient extracted from CALIPSO overpasses for 57 suitable cases. The color coding describes the distance of the CALIPSO observation from the ground site. Error bars refer to the results of using the lower and upper estimate in the value for humidification and the standard deviation from averaging over nine 60-m CALIPSO height bins between 250 and 730 m, respectively. Ratios of 1:1, 1:2, and 1:5 are marked by solid and dashed lines and the shaded area. The figure is from Tesche et al. (2014).

Figure 3.7 shows 57 suitable cases (of a total of 2018 CALIPSO overpasses) for com-paring extinction coefficients spaceborne and ground-based measurements. Even though CALIOP extinction coefficients are generally larger than the ones derived from the *in-situ* measurements, most comparisons can be reconciled to a factor of 1 to 5, with the majority not exceeding a factor of 2. The colour coding in Figure 3.7 gives no indication that a closer distance between satellite ground track and ground site (or a smaller time lag, not shown) would lead to a better outcome of the matching procedure. Successful reconciliation actually occurs for many cases associated with overpasses at larger distances from the ground site. Tesche et al. (2014) have also investigated effects of relative humidity at Zeppelin station and at the crossing point of the satellite ground track and trajectories, the occurrence of clouds and rain along the trajectory, and the wind direction at the ground site but find that only the latter parameter could be linked to the outliers in Figure 3.7. The largest difference in the ambient extinction coefficients from CALIOP and *in-situ* measurements occurs during westerly flow. Aerosol conditions for air masses approaching Zeppelin station from the north and via ice-covered ocean could be more stable compared to over open water to the west.

3.2.4 Aviation effects on already existing cirrus clouds

Air traffic is known to have an immediate and noticeable effect on clouds in the upper tropo-sphere. New clouds that form due to aircraft effluent are called contrails (Appleman 1953, Stubenrauch and Schumann 2005), and may develop into more persistent and widespread contrail cirrus. While optically thick cirrus clouds have a net cooling effect on surface tem-perature, optically thin cirrus clouds, like greenhouse gases, can have a warming effect.
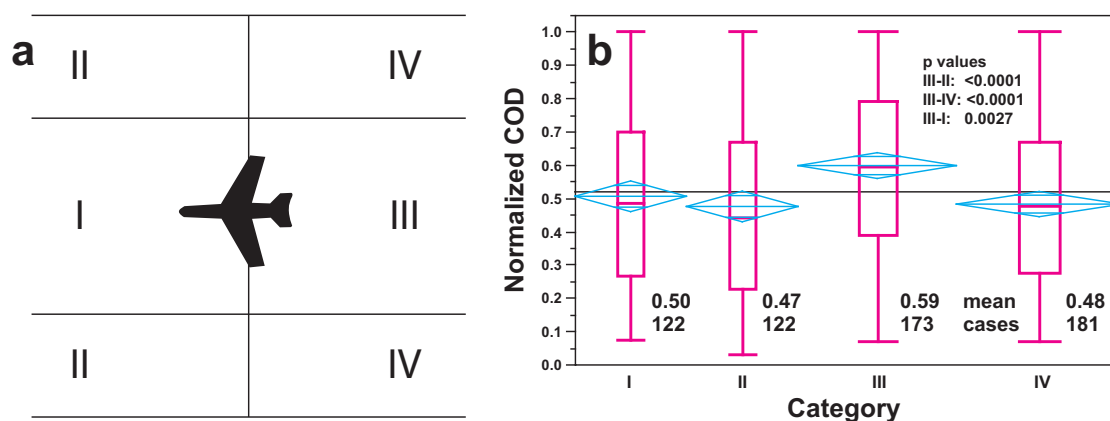
Figure 3.8: (**a**) Categories for data analysis. Category I: inside the flight track, ahead of the aircraft. Category II: outside the flight track, ahead of the aircraft. Category III: inside the flight track, behind the aircraft. Category IV: outside the flight track, behind the aircraft. (**b**) nCOD per category for a maximum cirrus geometrical depth of 2.5 km. The magenta box-and-whisker plots show the quantiles for the data in each category from a one-way analysis of variance using the JMP software package. Cyan diamonds indicate 95% confidence intervals for the mean values. If the upper and lower horizontal lines overlap, there is no statistically significant difference in means. Numbers in the lower part of the figure give the mean value and number of observations in each category. The horizontal line is the overall mean value. The Figure has been adapted from Tesche et al. (2016).

Boucher (1999) was the first to realize that aviation might have a strong influence on the occurrence rate of cirrus clouds. Aircraft emissions and contrails at cirrus altitudes have the potential to either cause optically thin cirrus clouds to form or increase the optical thickness of existing clouds (or induce new optically thick clouds). Studies of contrail optical properties are either based on passive remote sensing in which contrails are identified as linear features in scenes of brightness temperature differences (Minnis et al. 1999, 2005, Duda et al. 2013) or modelling studies in which contrails are formed when favourable meteorological conditions are reached (Schumann 2012). The life cycle of contrails and aviation-induced cirrus, their radiative forcing and feedback on natural clouds have been studied by treating them as an independent cloud class in a climate model (Burkhardt and Kärcher 2011). In general, aviation-induced clouds are optically thin and their climatic effects are estimated to be minor (Minnis et al. 1999, Sassen 1997, Schumann 2005) even when considering their entire life cycle (Burkhardt and Kärcher 2011). However, the effect of contrails embedded in natural cirrus (Gierens 2012) is a mechanism that currently has neither been studied nor assessed for its radiative effect (Lee et al. 2009). So far, only Iwabuchi et al. (2012) have made use of height-resolved observations from spaceborne lidar measurements to investigate the physical and optical properties of contrails.

Tesche et al. (2016) quantify the effect of aircraft on the optical thickness of already-existing cirrus clouds by matching actual aircraft flight tracks to satellite lidar measurements. Flight track data for commercial airline connections between Seattle (KSEA), San Francisco (KSFO), Los Angeles (KLAX), and Honolulu (PHNL) in the years 2010 and 2011 have been used to test the hypothesis that contrails formed within natural cirrus clouds have no measurable immediate effect on cirrus optical depth (COD) inside and outside flight tracks in the upper troposphere. CALIPSO lidar observations of COD, cloud base and top height, and cloud geometrical depth have been classified into four categories as illustrated in Figure 3.8a. Due to the skewness of the COD data, this parameter has been normalised (nCOD) to

the maximum value observed for individual matches. If the hypothesis that aircraft have no observable effect on cirrus cloud properties is true, then there should be no statistically significant differences in nCOD between the four categories. If the hypothesis is false, and aircraft emissions do have an impact on cloud properties, clouds in category III should have a different nCOD compared to the other categories.

The results of this analysis for cases in which the maximum geometrical cirrus depth of 2.5 km are shown in Figure 3.8b. The mean nCOD for category III (0.59) is significantly higher than for the other three categories (III–II: P<0.0001; III–IV: P<0.0001; III–I: P=0.0027). In terms of true COD, the category III mean value was 0.30, while the means of the other categories were as follows: I, 0.27; II, 0.26; IV, 0.26. Differences between the other categories were not statistically significant. This pattern has also been found for different maximum cloud layer depths. Overall, Tesche et al. (2016) show that there is a systematic, statistically significant increase in nCOD for mid-latitude cirrus close to flight tracks compared with adjacent areas unperturbed by the passing aircraft. Given the broad coverage of air traffic corridors in the northern hemisphere together with the continuous growth of the aviation industry, embedded contrails are potentially an important, yet unconsidered contributor to the non-CO_2 effects of aviation on climate (Lee et al. 2009).

3.3 Advances in the inversion of lidar data

The lack of an adequate theory for the description of light scattering by non-spherical particles is still a major challenge for both active and passive remote sensing of mineral dust and volcanic ash aerosols. While a variety of model particles has been proposed for this purpose (Kahnert et al. 2014, Nousiainen and Kandler 2015) there has not yet been a breakthrough in finding a method that is universally applicable for a variety of non-spherical particles. The closest solution to the problem is the light-scattering model developed for application to sun photometer measurements in the framework of AERONET (Dubovik et al. 2006). The Dubovik model considers rather simplified particle shapes, i.e. rotational symmetric spheroids with (i) a defined axis-ratio distribution and (ii) a fixed mixture of oblates and prolates. While this model is not capable of producing some of the light-scattering properties simulated by using irregularly shaped particles (Gasteiger et al. 2011) or observed with lidar (Müller et al. 2010b), it covers a large range of size parameters and can be implemented straightforwardly into other applications.

The TiARA inversion (Section 2.2.7) has so far been applied almost exclusively to atmospheric scenarios dominated by spherical particles. The first implementation of the spheroid Dubovik model for the inversion of lidar measurements of mineral dust has been presented by Veselovskii et al. (2010). The application requires values of δ_{532} as additional input. This new setup has been evaluated using lidar, sun-photometer, and *in-situ* measurements of pure dust and mixed dust-smoke plumes (**Paper X:** Müller et al. (2013)). Three variations of inversion input have been considered in this study: (i) the conventional 3+2 data set with spherical kernels (i.e. a spheroid fraction of 0%), (ii) the conventional 3+2 input with the spheroid fraction set to 100%, and (iii) a 3+2+1 data set in which δ_{532} is used to infer the spheroid fraction. Setup (ii) is similar to Veselovskii et al. (2010) who first identify pure dust conditions, set the spheroid fraction to 100%, and run the inversion with spheroid kernels.

Table 3.1: Combinations of δ_λ used as inversion input. The bottom part of the table provides the slope, intercept, and squared correlation coefficients (R^2) for the linear fits between dust ratio and spheroid fraction presented in Figure 3.9. The table has been adapted from Tesche et al. (2019).

Data set	I	II	III	IV	V	VI	VII	VIII
355 nm	-	X	-	-	X	X	-	X
532 nm	-	-	X	-	X	-	X	X
1064 nm	-	-	-	X	-	X	X	X
linear fits in Figure 3.9								
Slope	0.13	0.87	0.41	0.09	0.94	0.90	0.42	0.95
Intercept	18	8	58	80	9	11	62	13
R^2	0.17	0.69	0.33	0.03	0.73	0.68	0.46	0.73

The variation in the optical input was found to lead to differences of the inferred microphysical properties (Müller et al. 2013). For cases of pure mineral dust, the results of using different input data are consistent and confirm the validity of the spheroid particle model for data inversion. The use of spheroid kernels was found to give higher real parts and lower imaginary parts of the refractive index compared to the use of spherical kernels. Consequently, the use of spheroid kernels leads to increased SSA compared to the conventional inversion setup based on Mie scattering. In addition, real parts for pure dust inferred with setup (ii), and partly with setup (iii), were found to be in much better agreement with independent *in-situ* observations than those obtained from using setup (i).

Cases with a mixture of dust and biomass-burning smoke led to more limitations in the retrieval accuracy. In principle, using the 3+2+1 input enables the inversion of measurements in the presence of non-spherical particles without first having to separate the contributions of spherical and non-spherical particles as suggested by Tesche et al. (2009b, 2011b). However, a consistent investigation of using different depolarization information in the inversion of lidar data (**Paper XI:** Tesche et al. 2019) has been missing for two reasons. On the one hand, the inversion of lidar data using spheroid kernels and depolarization input had been focussed on cases of pure dust (Veselovskii et al. 2010, DiGirolamo et al. 2012, Papayannis et al. 2012, Müller et al. 2013). On the other hand, there are still few instruments with the capability for triple-wavelength depolarization measurements (e.g. Burton et al. 2015, Haarig et al. 2017a, or Hu et al. 2019). Consequently, few δ_λ measurements in the presence of mineral dust have been available for testing the effect of using different depolarization input in the inversion of lidar data.

To address both issues, Tesche et al. (2019) have used measurements with the NASA Langley Research Center's High Spectral Resolution Lidar 2 (HSRL-2, Hair et al. 2008, Burton et al. 2012, Müller et al. 2014, Burton et al. 2018) conducted in the framework of the DISCOVER-AQ project (Deriving Information on Surface Conditions from Column and VERtically Resolved Observations Relevant to Air Quality, https://discover-aq.larc.nasa.gov/) and data taken with BERTHA (Haarig et al. 2017a, b, 2018) during the Saharan Aerosol Longrange Transport and Aerosol-Cloud-Interaction Experiment (SALTRACE, Weinzierl et al. 2017). Both instruments are capable of providing 3+2+3 data sets that allow for a comprehensive characterization of different aerosol types. Measurements with increased δ_λ were used for inversion runs with depolarization input ranging from zero to three wavelengths. This gives eight inversion runs per measurement height bin as outlined in Table 3.1.
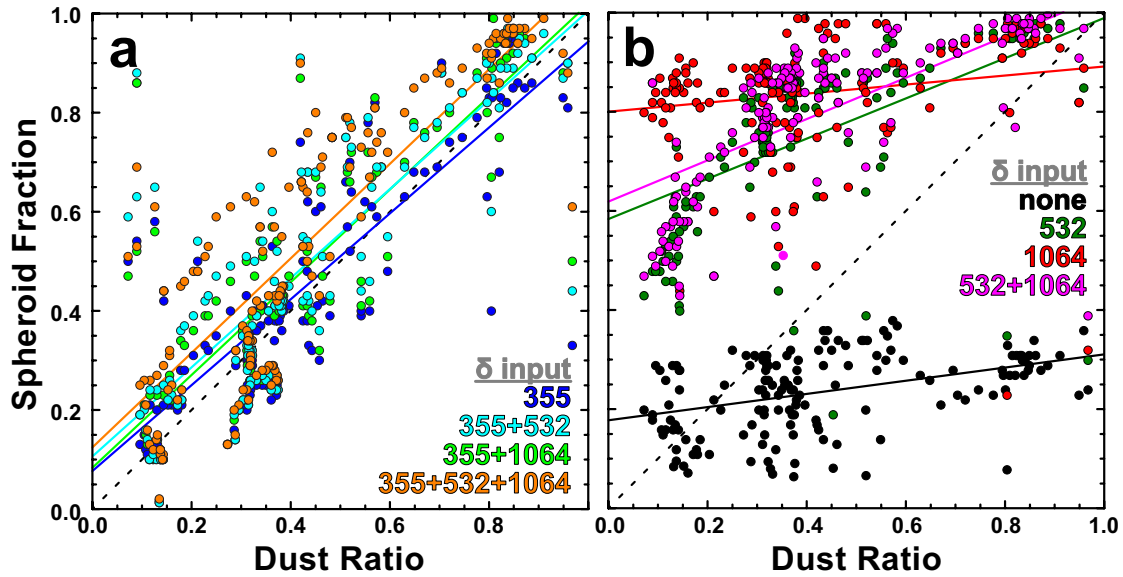
Figure 3.9: Connection between the retrieved spheroid fraction (from inversion) and the ratio of non-spherical particles to the 532-nm backscatter coefficient (from lidar measurements of δ_{532}) for the input data sets listed in Table 3.1. The figure has been adapted from Tesche et al. (2019).

The choice of δ_λ in the input data set has a strong effect on the retrieved spheroid fraction, and thus, on the contribution of spheroid kernels in the inversion calculation as shown in Figure 3.9. The spheroid fraction is considered as the microphysical manifestation of the optically-derived dust ratio defined in Eq. (2.20). Figure 3.9 shows that only input data sets that include δ_{355} lead to any meaningful correlation between dust ratio and spheroid fraction. The parameters of the linear regressions presented in Figure 3.9 are listed in the bottom half of Table 3.1. The steepest slope and largest values of the squared correlation coefficients are found for Sets II, V, VI, and VIII, i.e. the sets that use values for δ_λ at 355. Figure 3.9b confirms that (i) spheroid fractions above 40% are impossible to obtain from traditional 3+2 data sets, (ii) the data sets without δ_{355} give spheroid fractions that are poorly correlated to the obtained dust ratios, and (iii) data sets that include δ_{532} but not δ_{355} result in increased spheroid fractions that increase with increasing dust ratio but rarely stay below 40%. While it needs to be emphasized that the spheroid fraction as inferred from the inversion is an artificial, non-physical parameter, it might be considered as the ratio of the concentration of dust to total particles for this particular study. It therefore appears that in the case of using the spheroid model of Dubovik et al. (2006) to describe light scattering by non-spherical particles in the inversion of lidar, δ_{355} has a regulating effect on the inversion output and that data sets that include δ_{355} appear to be more trustworthy with respect to the spheroid fraction than those that do not include δ_{355}.

The choice of depolarization input has little effect on the retrieval of extensive parameters such as the volume concentration and the effective radius. The use of depolarization input at any wavelength generally increases the retrieved values of ω_{532} and leads to lower values of the imaginary part of the refractive index compared to traditional 3+2 input. Tesche et al. (2019) conclude that any inversion input that includes δ_{355} seems to provide more reasonable results than data sets without δ_{355} or any depolarization information at all. No significant advantage was found for using 3δ over using δ at fewer wavelengths. Hence, the most suitable input data set for lidar inversion using the Dubovik model appears to be 3+2+δ_{355}.

3.4 Use of lidar parameters to analyse sun photometer data

The availability of accurate measurements of aerosol-specific lidar parameters for the main aerosol species together with advancements in passive remote-sensing with sun photometers allows for adapting lidar-specific methodologies to the latter. Specifically, S_λ and δ_λ as provided in the AERONET version 3 level 2.0 aerosol inversion product can be used for (i) obtaining reference values of pure aerosol types in regions where a long-term deployment of lidar instruments is not feasible (**Paper XII:** Shin et al. 2018), (ii) inferring AOD and AAOD of the dust and non-dust components in dust-containing mixed aerosol plumes (**Paper XIII:** Shin et al. 2019a), and (iii) a refined aerosol-type classification that is capable of accurately separating between spherical and non-spherical particles as well as between absorbing and non-absorbing particles (**Paper XIV:** Shin et al. 2019b).

3.4.1 AERONET-derived lidar-specific parameters for mineral dust

The groundwork for making use of lidar-specific parameters as obtained from AERONET observations has been laid when lidar measurements during SAMUM (Ansmann et al. 2011b) were used to evaluate the performance of the AERONET inversion with the spheroid model of Dubovik et al. (2006). Müller et al. (2010b, 2012, 2013) were the first to compare AERONET-derived S_λ and δ_λ for Saharan dust to independent lidar measurements during pure dust conditions (Freudenthaler et al. 2009, Tesche et al. 2009a). However, these studies were limited to the one-month SAMUM field experiments in Morocco. In addition, lidar-specific parameters had to be retrieved outside of the AERONET processing chain as they were not a standard AERONET inversion output before the release of version 3 in 2016.

Lidar measurements of δ_λ are generally performed at 355 or 532 nm and triple-wavelength measurements are only presented by Freudenthaler et al. (2009), Burton et al. (2015), Haarig et al. (2017a), and Hu et al. (2019). Lidar measurements show that δ_λ differs with origin and age of the observed dust plume. Burton et al. (2015) find a maximum of δ_{1064} of 0.38 and lower values of 0.37 and 0.24 at 532 and 355 nm, respectively, for local North American dust. In contrast with this, transported Saharan dust shows a peak of 0.30 at 532 nm with smaller δ_λ of 0.27 and 0.25 at 1064 and 355 nm, respectively (Burton et al. 2015). Haarig et al. (2017a) report a similar spectral pattern in δ_λ for aged Saharan dust with a clear maximum of 0.28 at 532 nm and lower values of 0.25 at 355 nm and 0.23 at 1064 nm. The values for fresh Saharan dust observed by Freudenthaler et al. (2009) are almost identical to those of long-range-transported Saharan dust by Burton et al. (2015). All four scenarios agree on a δ_{355} of about 0.25.

Shin et al. (2018) have used AERONET data for pure dust conditions ($\mathring{a} < 0.4$ and $\eta < 0.1$) at sites in the Gobi, Saharan, Arabian, Great Basin, and Great Victoria deserts to obtain spectral S_λ and δ_λ and compared the findings to the literature of lidar observations of mineral dust at multiple wavelengths. Figure 3.10a shows that AERONET-derived δ_λ have a maximum of 0.26-0.31 at 1020 nm and decreasing values as wavelength decreases. AERONET-derived δ_λ at 870 and 1020 nm are in line with the lidar reference while values of 0.19-0.24 at 440 nm are smaller than the independent lidar observations by a difference of 0.03 to 0.08. This general behaviour is consistent with earlier studies based on AERONET version 2 products (Müller et al. 2010b).
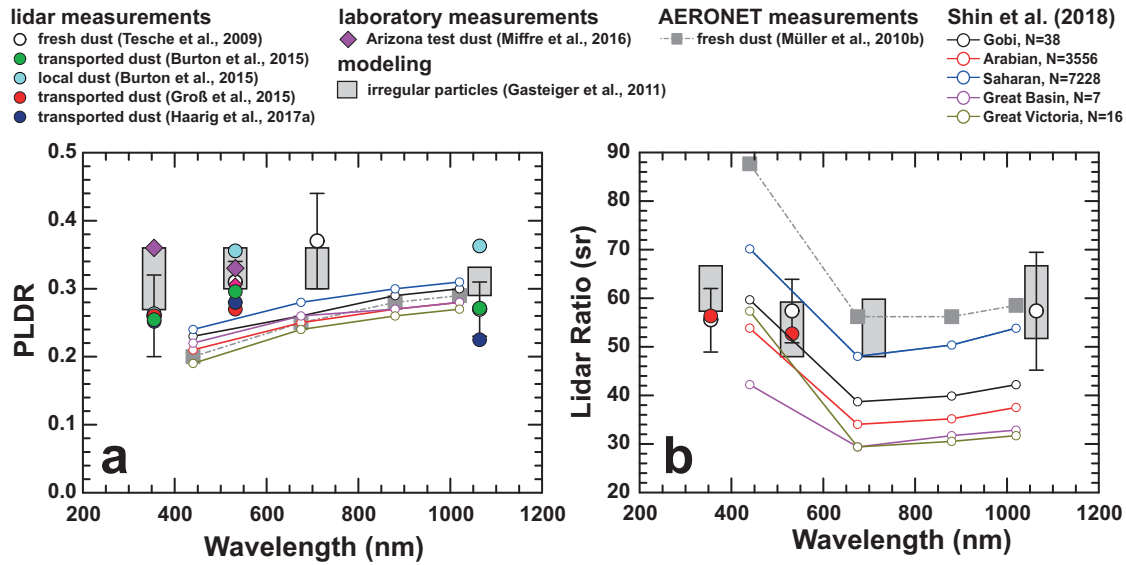
Figure 3.10: Spectral variation of (**a**) δ_λ and (**b**) S_λ as derived from AERONET observations for pure dust (open circles and lines) compared to published values from lidar observations (circles), laboratory measurements (magenta diamonds), light-scattering modelling using irregularly shaped particles (grey areas), and the AERONET-derived values of Müller et al. (2010b) (grey squares and line). The figure has been adapted from Shin et al. (2018) and Tesche et al. (2019).

The AERONET-derived S_λ at 675, 870, and 1020 nm in Figure 3.10b are in reasonable agreement with available lidar observations while those at 440 nm are up to 10 sr higher than the lidar reference. The focus of lidar observations has so far been on dust from the Sahara with mean values varying in a range of as much as 8 sr at both 355 and 532 nm. Direct measurements of S_{1064} are not available to date though the technique to achieve this has been developed recently (Haarig et al. 2016). Saharan dust clearly shows the highest values at any considered wavelength while values at 440 nm are generally highest for any considered region. The lowest values are found for the Great Basin and Great Victoria deserts, followed by the Arabian and Gobi deserts. The closure studies for Saharan dust of Müller et al. (2010b, 2012) provide an extensive discussion of the limitations of AERONET-derived lidar ratios – which are related mostly to the challenge of properly inferring the imaginary part of the complex refractive index. Compared to these studies, it appears that AERONET version 3 values of S_λ for Saharan dust moved much closer to the lidar observations at 532 nm as well as to model simulations that apply particle shapes of greater complexity than the Dubovik model (Gasteiger et al. 2011). It seems that AERONET-derived values at 675, 870, and 1020 nm are rather reliable while S_{440} likely exceeds the actual values, though no longer as much as in Müller et al. (2010b). While observations of Arabian and Asian dust are becoming more common, there are no literature values for the Great Basin and Great Victoria deserts. Consequently, the AERONET-derived lidar ratios presented by Shin et al. (2018) might provide a reference for future lidar observations of mineral dust from these regions.

3.4.2 Aerosol-type separation applied to AERONET data

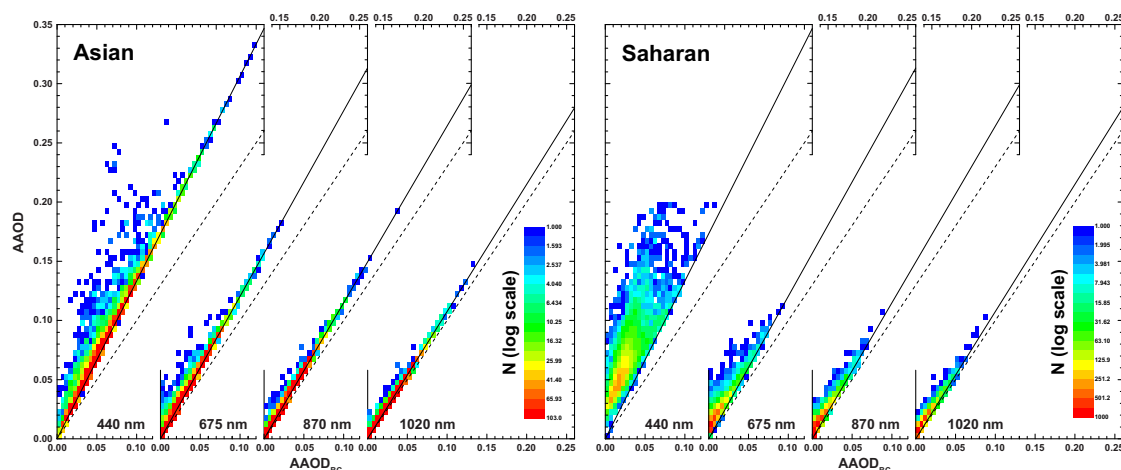Shin et al. (2019a) separate the contribution of dust and non-dust aerosol to total AOD

Figure 3.11: 2d histograms of AAOD and AAOD_{BC} at the four AERONET standard wavelengths for selected Asian (left) and Saharan (right) stations. Solid lines refer to the theoretical values of AAOD_{BC} in the absence of mineral dust. Dashed lines mark the 1:1 line that would be valid only if BC was a perfect absorber, i.e. $\omega_{\text{BC}} = 0$. The Figure has been adapted from Shin et al. (2019a).

in AERONET version 3 level 2.0 data at AERONET sites that are frequently affected by aerosol plumes that contain a mixture of Saharan or Asian mineral dust and biomass-burning smoke or anthropogenic pollution, respectively. Shin et al. (2019a) went on to derive the AAOD related to the non-dust component in the dusty mixture as well as to the fraction of BC. AAOD provides a measure of the light-absorbing properties of the columnar aerosol loading. However, it can be an ambiguous parameter if several types of absorbing aerosols, for instance BC and mineral dust, are present in a mixed aerosol plume. The connection between AAOD and AAOD_{BC} as inferred from using Eq. 2.24 is presented in Figure 3.11 for observations at the Asian and Saharan AERONET sites considered in Shin et al. (2019a). Absolute values of AAOD are generally larger for Asian compared to Saharan sites. The contribution of mineral dust to aerosol absorption at all wavelengths is generally larger at Saharan compared to Asian sites. A majority of AAOD_{BC} values at Asian sites follow the theoretical curve for dust-free situations ($\chi_{\text{dust}} = 0$), and the connection between AAOD and AAOD_{BC} is almost linear – particularly at longer wavelengths and larger AAOD_{BC}. For the same AAOD, larger χ_{dust} leads to a smaller AAOD_{BC}, and the corresponding observations are further away from the solid line in Figure 3.11. The abundance of pure dust conditions at the Saharan sites therefore leads to the larger spread of AAOD_{BC} in Figure 3.11 which is particularly pronounced at 440 nm.

The quality of the AAOD_{BC} retrieval can be evaluated through a comparison with the Copernicus Atmospheric Monitoring System aerosol re-analysis (CAMS, Inness et al. 2013). In Figure 3.12, these comparisons for three Asian AERONET sites are layered according to situations in which total AOD from AERONET and CAMS agree within 30%, 10%, and 5% of each other. These thresholds are introduced to assess that the considered cases actually represent situations in which the modelled aerosol is resembling the observations. The slopes of the linear fits between AERONET-derived and modelled AAOD_{BC} are reasonably close to the 1:1 line. This holds particularly when requiring less than 5% difference in measured and modelled AOD. No correlation was found for Saharan sites (not shown) that are frequently affected by a considerable contribution of anthropogenic pollution (Shin et al. 2019a).
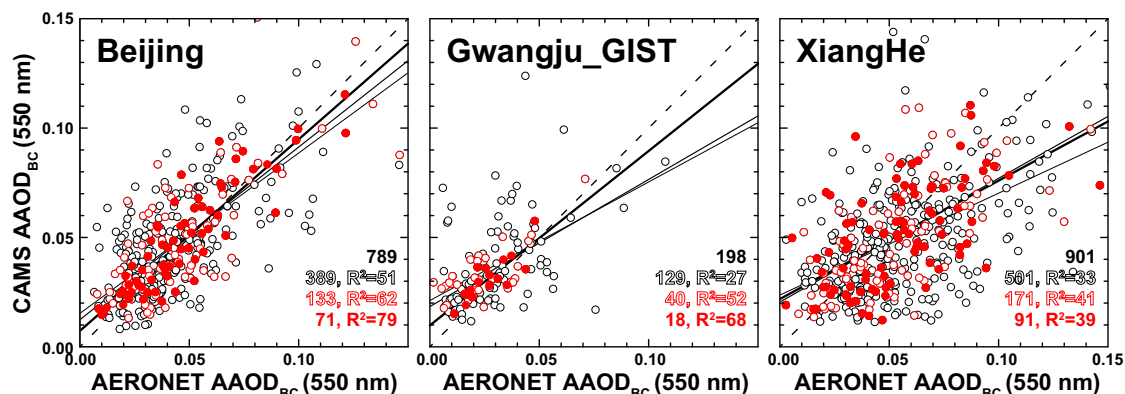
Figure 3.12: Comparison of AERONET-derived AAOD$_{BC}$ with CAMS model estimates for three AERONET sites in East Asia for cases in which the total AOD from CAMS and AERONET agrees within 30% (black circles, thin lines), 10% (red circles, medium lines), and 5% (red dots, bold lines). Dashed lines mark the 1:1 line. Solid lines are linear fits of the data. Numbers in the plots refer to the number of collocations and squared correlation coefficients for all cases (solid black, no R^2 given) and those with an AOD agreement within 30% (open black), 10% (open red), and 5% (solid red). The Figure has been adapted from Shin et al. (2019a).

Note that Shin et al. (2019a) present a very selective analysis of AERONET observations as a proof of concept of the proposed methodology. More conclusive findings require a thorough investigation of observations at a much larger set of AERONET sites. Nevertheless, their methodology is a useful tool for a more detailed calibration and validation of spaceborne remote-sensing observations and aerosol dispersion modelling with AERONET measurements. It is particularly valuable at locations with a frequent occurrence of complex mixtures of mineral dust and anthropogenic pollution.

3.4.3 AERONET aerosol-type classification using lidar parameters

The aerosol-type classification presented in Section 2.3.4 marks an improvement upon methods that use FMF and SSA to discriminate between different aerosol types (Lee et al. 2010, Giles et al. 2012) as it allows for a better separation between spherical and non-spherical particles as well as between particles with different light-absorbing characteristics. It therefore has the potential to provide improved information on aerosol type in regions where various types of aerosol are frequently present in the form of complex mixtures. Application of the novel aerosol-typing method to the global AERONET data base can also provide useful information for the validation of chemical transport modelling as well as spaceborne aerosol observations.

Shin et al. (2019b) evaluate their aerosol classification though a comparison to findings at AERONET stations representative for (1) anthropogenic particles: Goddard Space Flight Centre (GSFC, USA), Ispra (Italy), and Mexico City (Mexico), (2) biomass-burning smoke: Alta Floresta (Brazil), Mongu (Zambia), and Abracos Hill (Brazil), and (3) Saharan dust: Capo Verde (Cape Verde), Banizoumbou (Niger), and Dakar (Senegal). Figure 3.13 presents the mean spectral SSA and volume particle size distributions for these sites in comparison to the aerosol types defined in the new classification method. Dust particles are strongly absorbing at short wavelengths and less so at visible and near IR wavelengths.
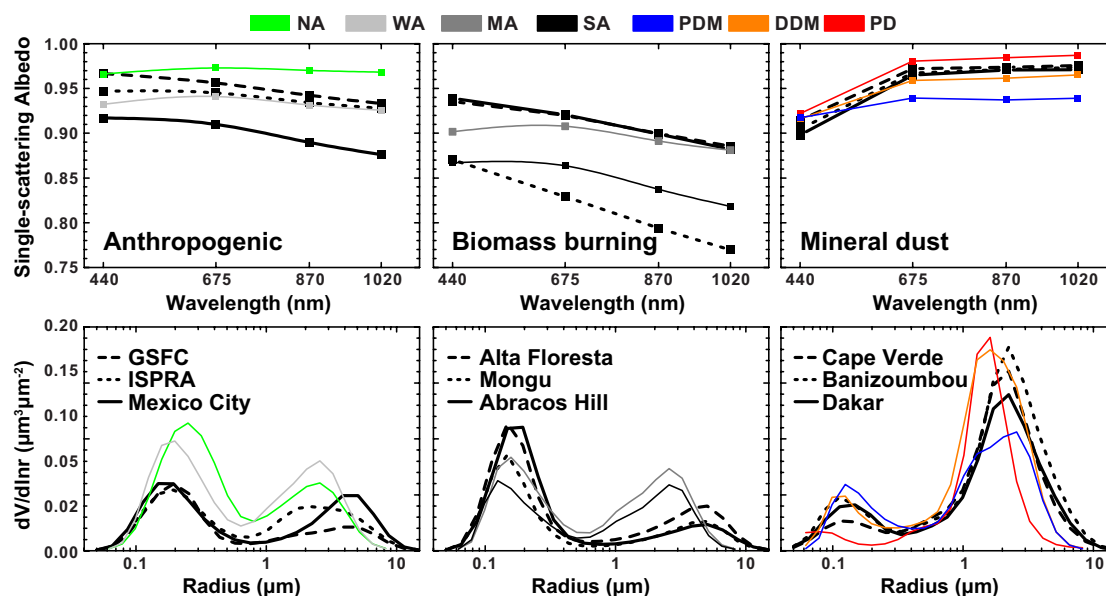
Figure 3.13: Mean spectral SSA (upper row) and mean particle size distributions (lower row) for AERONET sites that are considered as representative for different aerosol types as well as for the aerosol types defined in this study (see Figure 2.2 for color coding). Note that the size distribution for pure mineral dust (red line) has been scaled to 50% to fit the plot. The Figure has been adapted from Shin et al. (2019b).

Fine-mode particles and hygroscopic particles such as sulphate show nearly neutral spectral SSA and overall stronger scattering, i.e. higher SSA (Dubovik et al. 2002). BC has the strongest absorption properties in the near IR wavelength region. Organic and brown carbon absorb stronger at UV and visible wavelengths (Eck et al. 2009). The SSA for NA is higher than SSA at the anthropogenic sites at all wavelengths except for the observation at GSFC at 440 nm. The SSA for WA is similar to values obtained at GSFC and Ispra. It can be concluded from this that NA – in view of the definition of aerosol type – consists to a large degree of scattering particles. Similarly, WA represents aerosols that contain both scattering and absorbing particles with the former dominating. The spectral SSA of MA is similar to the values found at Alta Floresta and Abracos Hill except at the short wavelength. Consequently, MA is an aerosol mixture in which absorbing particles have a stronger impact, likely related to the contribution of organic carbon. Finally, the spectral SSA of SA is closest to the observations at Mongu and suggests that the absorbing properties of SA are related to a strong contribution of BC. The spectral SSA of DDM and PD is similar to the one found at the dust sites. However, the SSA of DDM is slightly lower than SSA of PD and of the AERONET dust sites as a result of mixing with pollutant particles. Accordingly, the SSA of PDM are even lower than of PD, DDM, and AERONET dust sites as it is defined to feature a larger contribution of pollutants.

The volume size distributions show a dominance of coarse-mode particles at the dust sites. Coarse-mode particles also contribute strongly to the total volume size distribution for PD and DDM, whereas a lower contribution of coarse-mode particles is found for PDM. This result is in line with an increased concentration of anthropogenic pollution or biomass-burning smoke which, in the PDM type, are typically considered to be fine-mode particles (Eck et al. 1999). Fine-mode particles contribute most strongly to the total volume size distribution at biomass-burning sites. Additionally, the contributions of fine and coarse modes are

distributed evenly in the total volume size distribution for MA and SA. Reid et al. (1998) found from studies in rain forest regions of Brazil that fresh smoke particles are significantly smaller than well-aged smoke particles. Hence, fresh smoke particles contribute significantly at the biomass-burning sites, whereas MA and SA detected over East Asia are affected not only by fine-mode particles but also a considerable amount of coarse-mode particles, in contrast to the source regions of biomass burning. The contributions of fine-mode and coarse-mode particles to the total volume size distributions are rather similar for the anthropogenic sites. However the contribution of fine-mode particles to the total volume size distributions is dominant for NA.

4 Summary and outlook

This thesis provides an overview of recent advances in the remote-sensing of aerosols and clouds with lidar and lidar-based methodologies along four themes; all of which provide great potential for ongoing and future research. This section summarizes the main advancements as well as suggested lines of future research for the different themes.

The work on the use of lidar measurements for the retrieval of CCN and INP concentrations **[Theme 1]** has only just begun. Several issues will need to be addressed in the future. First, it needs to be assessed in how far the methodologies developed for ground-based lidar can be adopted for spaceborne measurements. While Mamouri and Ansmann (2015) and Marinou et al. (2019) have presented reasonable agreement in INP concentrations obtained from ground-based and spaceborne lidar measurements as well as airborne *in-situ* sampling, it is still unclear if this will also be possible for CCN profiling. In particular, it will be necessary to bound the range of aerosol load (in terms of extinction coefficient and AOD) for which lidar-derived CCN and INP concentrations should be considered as a meaningful product. Second, further coordinated measurement campaigns and experiments with synergistic measurement setup will be needed to achieve closure between CCN and INP concentration from *in-situ* sampling and lidar profiling for different aerosol types to a degree that is in line with our level of scientific understanding. In that context, agreement within an order of magnitude might be the best we will ever get for this complex problem. Particularly as the also required information in ambient relative humidity cannot be derived from remote-sensing observations with the precision that is needed to account for small changes in supersaturation over water and ice. Nevertheless, this course of action will also help to resolve issues related to the first item. Finally, it needs to be assessed if today's CCN and INP parametrizations are indeed the end of the line or if more unified relationships can be obtained to describe the connection between the concentration of the total aerosol ensemble and the fraction that acts as CCN and INP.

It therefore might take a few more years before the methodologies presented here are likely to lead to the first global, height-resolved, and aerosol-type specific climatology on the concentration of particles that are relevant for the formation and evolution of clouds. Such information is of crucial importance for studying aerosol-cloud interactions which are still one of the largest factors of uncertainty in our understanding of anthropogenic climate change. While this line of research is already been pursued through the synergistic combination of aerosol lidar, cloud radar, and passive radiometers from both ground and space, information on CCN and INP concentrations at cloud level is still the missing piece of the puzzle. The combination of this information with cloud parameters retrieved from spaceborne remote sensing forms a main line of study of the authors current work within the *Make Our Planet Great Again–German Research Initiative* (MOPGA-GRI) Senior Research Project PACIFIC.

The availability of the first long-term data set of spaceborne lidar observations together with the novelty of the obtained form of information for the wider scientific community are the foundation of the two branches described in **[Theme 2]**: the evaluation of spaceborne lidar

observations and their application in innovative studies that could not be attempted with passive sensors. The need for assessing the performance of spaceborne lidar measurements with ground-truth observations is of particular importance for CALIPSO follow-up missions such as Aeolus (Reitebuch 2012) and EarthCARE (Illingworth et al. 2015). This is why such activities are now an essential part in the respective planning procedures. The CALIPSO data set will remain a treasure chest for innovative research for years to come, particularly when combined with other data sets. Ideally, the research initiated by Tesche et al. (2016) will be continued in the framework of the three-year research project *Properties and Effects of Embedded ContrAils from spaceBOrne Observations (PEECABOO)* – a proposal that has been submitted to the German Science Foundation (DFG) in February 2020. Together with project partners at the German Aerospace Center (DLR), a much larger set of flight tracks will be investigated over a longer time period together with a focus on height-resolved parameters for pristine cirrus and those parts that are affected by embedded contrails. The analysis of spaceborne lidar data will be complemented with case studied of airborne lidar measurements conducted in the framework of the Midlatitude Cirrus experiment (ML-CIRRUS, Voigt et al. 2017). In addition, modelling will be used to assess the impact of an increase in cloud optical depth on the Earth's radiative budget. A preliminary study has already shown that a model capable of resolving contrail microphysics can reproduce the observations of Tesche et al. (2016).

Over the last 20 years, the retrieval of aerosol microphysical properties from multiwavelength lidar data **[Theme 3]** has matured to a stage that allows for automated and unsupervised operation in near-real time (Chemyakin et al. 2014, Müller et al. 2019) and with reasonable accuracy when compared to *in-situ* measurements (Sawamura et al. 2017). Taking the methodology beyond the current – though well established – proof-of-concept stage requires two main advancements: (i) an automated and unified application to the abundance of 3+2 lidar instruments in the framework of the current observational networks with data access comparable to the AERONET level 2.0 inversion product and (ii) the universal applicability to observations of all aerosol types including mineral dust and volcanic ash. The latter remains the bigger challenge as the required methodologies for an adequate description of light-scattering by non-spherical particles for lidar applications is still not available.

The lidar-specific methods for the analysis of sun-photometer observations within AERONET **[Theme 4]** have so far been applied only to a few sites. In future, dedicated experiments that combine AERONET measurements with advanced aerosol lidar observations and height-resolved *in-situ* profiling, e.g. with unmanned aerial vehicles or from tethered balloons, will be needed to assess the retrieval of BC-related AAOD and to investigate if the AERONET aerosol typing based on lidar parameters is in line with the more comprehensive lidar observations. The latter point is of particular relevance as what is referred to as a mixed plume in an AERONET measurement might actually be several spatially well-separated layers of different aerosol types as would easily be observable as such with lidar. Nevertheless, the methodologies described here will have to be expanded to the entire AERONET data base with the scope of a more thorough assessment if AERONET-derived BC-related AAOD that can be used for the evaluation of aerosol transport models. Such an evaluation is currently not possible as it is often hard to reconcile the optically defined aerosol types used in atmospheric remote sensing with the chemically defined aerosol types considered in aerosol transport models. In addition, future work will also have to focus on the application of the lidar-based aerosol typing to the AERONET data base together with radiative-transfer calculations to study the aerosol-type specific radiative forcing and use the

findings to corroborate the quality of corresponding model estimates.

Despite the manifold need for further improvement outlined above, the lidar technique and its application in atmospheric science have become a tremendous force for innovation in research on aerosols, clouds, and aerosol-cloud interactions. The increased visibility of the value of atmospheric lidar observations together with the ongoing development towards compact advanced system for continuous ground-based measurements and the increased recognition of the need for spaceborne observations form a solid base for taking the next step in unleashing the full potential of lidar observations in atmospheric research within the coming decade.

5 Appendix

5.1 List of Abbreviations and Acronyms

Abbreviation	Description
AERONET	Aerosol Robotic Network
AI	aerosol index
AAOD	absorption aerosol optical depth
AOD	aerosol optical depth
BC	black carbon
BERTHA	Backscatter Extinction lidar-Ratio Temperature Humidity Apparatus
CALIOP	Cloud-Aerosol Lidar with Orthogonal Polarization
CALIPSO	Cloud-Aerosol Lidar and Infrared Pathfinder Satellite Observation
CAMS	Copernicus Atmosphere Monitoring Service
CCN	cloud condensation nuclei
COD	cirrus optical depth
DDM	dust-dominated mixture
DFG	German Science Foundation
DISCOVER-AQ	Deriving Information on Surface Conditions from Column and VERtically Resolved Observations Relevant to Air Quality
DLR	German Aerospace Center
DMPS	differential mobility particle sizer
EARLINET	European Aerosol Research Lidar Network
FMF	fine-mode fraction
FRIDGE	FRankfurt Ice nucleation Deposition freezinG Experiment
GSFC	Goddard Space Flight Center
HSRL	high spectral resolution lidar
HYSPLIT	hybrid single-particle Lagrangian integrated trajectories model
INP	ice nucleating particles
IR	infrared
lidar	light detection and ranging
MA	moderately absorbing
ML-CIRRUS	Midlatitude Cirrus experiment
MODIS	Moderate Resolution Imaging Spectroradiometer
MOPGA-GRi	Make Our Planet Great Again–German Research Initiative
NA	non-absorbing
NAT	nitric acid trihydrate
nCOD	normalised cirrus optical depth
Nd:YAG	neodym-doted yttrium-aluminium-granat
OPAC	Optical Properties of Aerosols and Clouds
OPC	optical particle counter

PD	pure dust
PDM	pollution-dominated mixture
POLIPHON	Polarization Lidar Photometer Networking
PSAP	particle soot absorption photometer
PSC	Polar Stratospheric Cloud
SA	strongly absorbing
SALTRACE	Saharan Aerosol Long-range Transport and Aerosol-Cloud-Interaction Experiment
SAMUM	Saharan Mineral Dust Experiment
SNR	signal-to-noise ratio
SSA	single-scattering albedo
STS	supercooled ternary solutions
TiARA	Tikhonov Advanced Regularization Algorithm
UAV	unmanned aerial vehicle
UV	ultraviolet
UTC	universal time coordinated
VAAC	Volcanic Ash Advisory Centre
WA	weakly absorbing

5.2 List of Symbols

Symbol	Description	Unit
Indices		
$\parallel$	the co–polarized component of a quantity	
$\perp$	the cross–polarized component of a quantity	
$_\mathrm{a}$	ash	
$_\mathrm{BC}$	black carbon	
$_\mathrm{c}$	coarse	
$_\mathrm{c}$	continental pollution	
$_\mathrm{d}$	dust	
$_\mathrm{dry}$	dried particles	
$_\mathrm{f}$	fine	
$_\mathrm{ice}$	ice	
$_\mathrm{m}$	molecules	
$_\mathrm{na}$	non-ash	
$_\mathrm{nd}$	non-dust	
$_\mathrm{o}$	marine	
$_\mathrm{p}$	particles	
$_\mathrm{T}$	total	
$_\mathrm{v}$	volume	
$_\mathrm{w}$	water	
$_\mathrm{s}$	smoke	
Greek Symbols		
α_λ	extinction coefficient	$\mathrm{m^{-1}}$
β_λ	backscatter coefficient	$\mathrm{m^{-1}sr^{-1}}$
δ_λ	linear depolarization ratio	
η	fine-mode fraction	
τ	aerosol optical depth	
Θ	scattering zenith angle	$^\circ$
λ	wavelength	m
λ_0	laser wavelength	m
σ_ext	extinction cross section	$\mathrm{m^2}$
σ_sca	scattering cross section	$\mathrm{m^2}$
Φ	scattering azimuth angle	$^\circ$
ρ	density	$\mathrm{kg\ m^{-3}}$
ω	single-scattering albedo	
χ	ratio of an aerosol species to AOD	
Latin Symbols		
$\mathring{a}_{\lambda_1,\lambda_2}$	Ångström exponent	
$\mathring{a}_{\lambda_1,\lambda_2}^{\alpha}$	extinction–related Ångström exponent	
$\mathring{a}_{\lambda_1,\lambda_2}^{\beta}$	backscatter–related Ångström exponent	
$\mathring{a}_{\lambda_1,\lambda_2}^{S}$	lidar–ratio–related Ångström exponent	
c	speed of light	m/s
E_λ	lidar system term	

$\boldsymbol{E}$	electric field vector	
$\boldsymbol{F}(\Theta, \Phi)$	4×4 transformation matrix	
$F_{ij}(\Theta, \Phi)$	elements of $\boldsymbol{F}(\Theta)$	
I	Stokes parameter of total intensity	
m	mass concentration	kg m^{-3}
m	complex refractive index	
m_{i}	imaginary part of the complex refractive index	
m_{r}	real part of the complex refractive index	
n	number concentration	m^{-3}
n_{INP}	INP concentration	L^{-1}
$n(r)$	particle number size distribution	m^{-3}
O_{λ}	overlap function	
$p(\Theta, \Phi)$	scattering phase function	
$P_{0,\lambda}$	emitted laser energy	W
P_{λ}	lidar signal/detected energy	W
Q	Stokes parameter of intensity along the x and y axes	
r	particle radius	m
r_{eff}	effective particle radius	m
R	range	m
R	backscatter ratio	
R	ratio of an aerosol species to the particle backscatter coefficient	
$\boldsymbol{S}_0$	Stokes vector of incident light	
$\boldsymbol{S}$	Stokes vector of scattered light	
RH	relative humidity	%
S	particle surface-area concentration	m^{2}m^{-3}
S	supersaturation	
S_{λ}	lidar ratio	sr
t	time	s
T	temperature	°C
U	Stokes parameter of intensity along the $-45°/+45°$ axes	
v/τ	extinction-to-mass conversion factor	m
V	Stokes parameter of right– and left–hand circular intensity	
x	Cartesian coordinate	
y	Cartesian coordinate	
z	Cartesian coordinate	

Bibliography

Achtert, P. and M. Tesche, 2014: Assessing lidar-based classification schemes for Polar Stratospheric Clouds based on 16 years of measurements at Esrange, Sweden. *J. Geophys. Res.*, **119**, 1386–1405, 10.1002/2013JD020355.

Ackermann, J., 1998: The extinction–to–backscatter ratio of tropospheric aerosol: A numerical study. *J. Atmos. Oceanic Technol.*, **15**, 1043–1050.

Adriani, A., P. Massoli, G. Di Donfrancesco, F. Cairo, M. L. Moriconi, and M. Snels, 2004: Climatology of Polar Stratospheric Clouds based on lidar observations from 1993 to 2001 over McMurdo Station, Antarctica. *J. Geophys. Res.*, **109**, 10.1029/2004JD004800.

Althausen, D., D. Müller, A. Ansmann, U. Wandinger, H. Hube, E. Clauder, and S. Zörner, 2000: Scanning 6–wavelength 11–channel aerosol lidar. *J. Atmos. Oceanic Technol.*, **17**, 1469–1482.

Ångström, A., 1964: The parameters of atmospheric turbidity. *Tellus*, **16**, 64–76, 10.1111/j.2153-3490.1964.tb00144.x.

Ansmann, A., F. Wagner, D. Müller, D. Althausen, A. Herber, and coauthors, 2002b: European pollution outbreaks during ACE 2: Optical particle properties inferred from multiwavelength lidar and star–Sun photometry. *J. Geophys. Res.*, **107**, 10.1029/2001JD001109.

Ansmann, A. and D. Müller, 2005: *Lidar and Atmospheric Aerosol Particles*, in: LIDAR: Range–Resolved Optical Remote Sensing of the Atmosphere, ed. by C. Weitkamp, Springer. 105–142.

Ansmann, A., M. Tesche, S. Groß, V. Freudenthaler, P. Seifert, A. Hiebsch, J. Schmidt, U. Wandinger, I. Mattis, D. Müller, and M. Wiegner, 2010: The 16 April 2010 major volcanic ash plume over central Europe: EARLINET lidar and AERONET photometer observations at Leipzig and Munich, Germany. *Geophys. Res. Lett.*, **37**, 10.1029/2010GL043809.

Ansmann, A., M. Tesche, P. Seifert, S. Groß, V. Freudenthaler, A. Apituley, K. M. Wilson, I. Serikov, H. Linné, B. Heinold, A. Hiebsch, F. Schnell, J. Schmidt, I. Mattis, U. Wandinger, and M. Wiegner, 2011a: Ash and fine-mode particle mass profiles from EARLINET-AERONET observations over central Europe after the eruptions of the Eyjafjallajökull volcano in 2010. *J. Geophys. Res.*, **116**, 10.1029/2010JD015567.

Ansmann, A., A. Petzold, K. Kandler, I. Tegen, M. Wendisch, D. Müller, B. Weinzierl, T. Müller, and J. Heintzenberg, 2011b: Saharan Mineral Dust Experiments SAMUM1 and SAMUM2: What have we learned? *Tellus*, **63B**, 403–429, 10.1111/j.1600-0889.2011.00555.x.

Ansmann, A., P. Seifert, M. Tesche, and U. Wandinger, 2012: Profiling of fine and coarse particle mass: Case studies of Saharan dust and Eyjafjallajökull/Grimsvötn volcanic plumes. *Atmos. Chem. Phys.*, **12**, 9399–9415, 10.5194/acp-12-9399-2012.

Ansmann, A., R.-E. Mamouri, J. Hofer, H. Baars, D. Althausen, and S. F. Abdullaev, 2019a: Dust mass, cloud condensation nuclei, and ice-nucleating particle profiling with polarization lidar: Updated POLIPHON conversion factors from global AERONET analysis. *Atmos. Meas. Techn.*, **12**, 4849–4865, 10.5194/amt-12-4849-2019.

Ansmann, A., R.-E. Mamouri, J. Bühl, P. Seifert, R. Engelmann, J. Hofer, A. Nisantzi, J. D. Atkinson, Z. A. Kanji, B. Sierau, M. Vrekoussis, and J. Sciare, 2019: Ice-nucleating particle versus ice crystal number concentration in altocumulus and cirrus layers embedded in Saharan dust: a closure study. *Atmos. Chem. Phys.*, **19**, 15087–15115, 10.5194/acp-19-15087-2019.

Appleman, H., 1953: The Formation of Exhaust Condensation Trails by Jet Aircraft. *Bull. Am. Meteorol. Soc.*, **34**, 14–20.

Belegante, L., J. A. Bravo-Aranda, V. Freudenthaler, D. Nicolae, A. Nemuc, D. Ene, L. Alados-Arboledas, A. Amodeo, G. Pappalardo, G. D'Amico, F. Amato, R. Engelmann, H. Baars, U. Wandinger, A. Papayannis, P. Kokkalis, and S. N. Pereira, 2018: Experimental techniques for the calibration of lidar depolarization channels in EARLINET. *Atmos. Meas. Techn.*, **11**, 1119–1141, 10.5194/amt-11-1119-2018.

Ben-Ami, Y., I. Koren, and O. Altaratz, 2009: Patterns of North African dust transport over the Atlantic: winter vs. summer, based on CALIPSO first year data. *Atmos. Chem. Phys.*, **9**, 10.5194/acp-9-7867-2009.

Biele, J., A. Tsias, B. P. Luo, K. S. Carslaw, R. Neuber, G. Beyerle, and T. Peter, 2001: Nonequilibrium co-existence of solid and liquid particles in Arctic stratospheric clouds. *J. Geophys. Res.*, **106**, 22991–23007, 10.1029/2001JD900188.

Blum, U., K. H. Fricke, K. P. Müller, J. Siebert, and G. Baumgarten, 2005: Long-term lidar observations of Polar Stratospheric Clouds at Esrange in northern Sweden. *Tellus*, **57B**, 412–422, 10.3402/tellusb.v57i5.16562.

Bohren, C. F. and D. R. Huffman, 1983: *Absorption and Scattering of Light by Small Particles*. John Wiley, New York, 544 pp.

Bond, T. C. and R. W. Bergstrom, 2006: Light absorption by carbonaceous particles: An investigative review. *Aero. Sci. Techn.*, **40**, 27–67, 10.1080/02786820500421521.

Bond, T. C., S. J. Doherty, D. W. Fahey, P. M. Forster, T. Berntsen, B. J. DeAngelo, M. G. Flanner, S. Ghan, B. Kärcher, D. Koch, S. Kinne, Y. Kondo, P. K. Quinn, M. C. Sarofim, M. G. Schultz, M. Schulz, C. Venkataraman, H. Zhang, S. Zhang, N. Bellouin, S. K. Guttikunda, P. K. Hopke, M. Z. Jacobson, J. W. Kaiser, Z. Klimont, U. Lohmann, J. P. Schwarz, D. Shindell, T. Storelvmo, S. G. Warren, and C. S. Zender, 2013: Bounding the role of black carbon in the climate system: A scientific assessment. *J. Geophys. Res.*, **118**, 5380–5552, 10.1002/jgrd.50171.

Boucher, O., 1999: Air traffic may increase cirrus cloudiness. *Nature*, **397**, 1476–4687, 10.1038/16169.

Bravo-Aranda, J. A., L. Belegante, V. Freudenthaler, L. Alados-Arboledas, D. Nicolae, M. J. Granados-Muñoz, J. L. Guerrero-Rascado, A. Amodeo, G. D'Amico, R. Engelmann, G. Pappalardo, P. Kokkalis, R. Mamouri, A. Papayannis, F. Navas-Guzmán, F. J. Olmo, U. Wandinger, F. Amato, and M. Haeffelin, 2016: Assessment of lidar depolarization uncertainty by means of a polarimetric lidar simulator. *Atmos. Meas. Techn.*, **9**, 4935–4953, 10.5194/amt-9-4935-2016.

Brooks, S. D., D. Baumgardner, B. Gandrud, J. E. Dye, M. J. Northway, D. W. Fahey, T. P. Bui, O. B. Toon, and M. A. Tolbert, 2003: Measurements of large stratospheric particles in the Arctic polar vortex. *J. Geophys. Res.*, **108**, 10.1029/2002JD003278.

Browell, E. V., C. F. Butler, S. Ismail, P. A. Robinette, A. F. Carter, N. S. Higdon, O. B. Toon, M. R. Schoeberl, and A. F. Tuck, 1990: Airborne lidar observations in the wintertime Arctic stratosphere: Polar Stratospheric Clouds. *Geophys. Res. Lett.*, **17**, 385–388, 10.1029/GL017i004p00385.

Bucholtz, A., 1995: Rayleigh–scattering calculations for the terrestrial atmosphere. *Appl. Opt.*, **34**, 10.1364/AO.34.002765.

Burton, S. P., R. A. Ferrare, C. A. Hostetler, J. W. Hair, C. Kittaka, M. A. Vaughan, M. D. Obland, R. R. Rogers, A. L. Cook, D. B. Harper, and L. A. Remer, 2010: Using airborne high spectral resolution lidar data to evaluate combined active plus passive retrievals of aerosol extinction profiles. *J. Geophys. Res.*, **115**, 10.1029/2009JD012130.

Burton, S. P., R. A. Ferrare, C. A. Hostetler, J. W. Hair, R. R. Rogers, M. D. Obland, C. F. Butler, A. L. Cook, D. B. Harper, and K. D. Froyd, 2012: Aerosol classification using airborne High Spectral Resolution Lidar measurements – methodology and examples. *Atmos. Meas. Techn.*, **5**, 73–98, 10.5194/amt-5-73-2012.

Burton, S. P., R. A. Ferrare, M. A. Vaughan, A. H. Omar, R. R. Rogers, C. A. Hostetler, and J. W. Hair, 2013: Aerosol classification from airborne HSRL and comparisons with the CALIPSO vertical feature mask. *Atmos. Meas. Techn.*, **6**, 1397–1412, 10.5194/amt-6-1397-2013.

Burton, S. P., J. W. Hair, M. Kahnert, R. A. Ferrare, C. A. Hostetler, A. L. Cook, D. B. Harper, T. A. Berkoff, S. T. Seaman, J. E. Collins, M. A. Fenn, and R. R. Rogers, 2015: Observations of the spectral dependence of linear particle depolarization ratio of aerosols using NASA Langley airborne High Spectral Resolution Lidar. *Atmos. Chem. Phys.*, **15**, 13453–13473, 10.5194/acp-15-13453-2015.

Burton, S. P., C. A. Hostetler, A. L. Cook, J. W. Hair, S. T. Seaman, S. Scola, D. B. Harper, J. A. Smith, M. A. Fenn, R. A. Ferrare, P. E. Saide, E. V. Chemyakin, and D. Müller, 2018: Calibration of a High Spectral Resolution Lidar using a Michelson interferometer, with data examples from ORACLES. *Appl. Opt.*, **57**, 6061–6075, 10.1364/AO.57.006061.

Burton, S. P., M. A. Vaughan, R. A. Ferrare, and C. A. Hostetler, 2014: Separating mixtures of aerosol types in airborne High Spectral Resolution Lidar data. *Atmos. Meas. Techn.*, **7**, 419–436, 10.5194/amt-7-419-2014.

Burkhardt, U. and B. Kärcher, 2011: Global radiative forcing from contrail cirrus. *Nature Climate Change*, **1**, 1758–6798, 10.1038/nclimate1068.

Chemyakin, E., D. Müller, S. Burton, A. Kolgotin, C. Hostetler, and R. Ferrare, 2014: Arrange and average algorithm for the retrieval of aerosol parameters from multiwavelength High Spectral Resolution Lidar/Raman lidar data. *Appl. Opt.*, **53**, 7252–7266, 10.1364/AO.53.007252.

Crutzen, P. J. and F. Arnold, 1986: Nitric acid cloud formation in the cold Antarctic stratosphere: A major cause

for the springtime ozone hole. *Nature*, **324**, 10.1038/324651a0.

D'Amico, G., A. Amodeo, H. Baars, I. Binietoglou, V. Freudenthaler, I. Mattis, U. Wandinger, and G. Pappalardo, 2015: EARLINET Single Calculus Chain overview on methodology and strategy. *Atmos. Meas. Techn.*, **8**, 4891–4916, 10.5194/amt-8-4891-2015.

David, C., S. Bekki, N. Berdunov, M. Marchand, M. Snels, and G. Mégie, 2005: Classification and scales of Antarctic Polar Stratospheric Clouds using wavelet decomposition. *J. Atmos. Sol.-Ter. Phys.*, **67**, 293 – 300, https://doi.org/10.1016/j.jastp.2004.07.043.

David, C., S. Bekki, S. Godin, G. Mégie, and M. P. Chipperfield, 1998: Polar Stratospheric Clouds climatology over Dumont d'Urville between 1989 and 1993 and the influence of volcanic aerosols on their formation. *J. Geophys. Res.*, **103**, 22163–22180, 10.1029/98JD01692.

DeMott, P. J., T. C. J. Hill, C. S. McCluskey, K. A. Prather, D. B. Collins, R. C. Sullivan, M. J. Ruppel, R. H. Mason, V. E. Irish, T. Lee, C. Y. Hwang, T. S. Rhee, J. R. Snider, G. R. McMeeking, S. Dhaniyala, E. R. Lewis, J. J. B. Wentzell, J. Abbatt, C. Lee, C. M. Sultana, A. P. Ault, J. L. Axson, M. Diaz Martinez, I. Venero, G. Santos-Figueroa, M. D. Stokes, G. B. Deane, O. L. Mayol-Bracero, V. H. Grassian, T. H. Bertram, A. K. Bertram, B. F. Moffett, and G. D. Franc, 2016: Sea spray aerosol as a unique source of ice nucleating particles. *Proc. Nat. Acad. Sci.*, **113**, 5797–5803, 10.1073/pnas.1514034112.

DeMott, P. J., A. J. Prenni, X. Liu, S. M. Kreidenweis, M. D. Petters, C. H. Twohy, M. S. Richardson, T. Eidhammer, and D. C. Rogers, 2010: Predicting global atmospheric ice nuclei distributions and their impacts on climate. *Proc. Nat. Acad. Sci.*, **107**, 11217–11222, 10.1073/pnas.0910818107.

DeMott, P. J., A. J. Prenni, G. R. McMeeking, R. C. Sullivan, M. D. Petters, Y. Tobo, M. Niemand, O. Möhler, J. R. Snider, Z. Wang, and S. M. Kreidenweis, 2015a: Integrating laboratory and field data to quantify the immersion freezing ice nucleation activity of mineral dust particles. *Atmos. Chem. Phys.*, **15**, 393–409, 10.5194/acp-15-393-2015.

Devasthale, A., M. Tjernström, and A. H. Omar, 2011: The vertical distribution of thin features over the Arctic analysed from CALIPSO observations. *Tellus B*, **63**, 86–95, 10.1111/j.1600-0889.2010.00517.x.

DiGirolamo, P., D. Summa, R. Bhawar, T. D. Iorio, M. Cacciani, I. Veselovskii, O. Dubovik, and A. Kolgotin, 2012: Raman lidar observations of a Saharan dust outbreak event: Characterization of the dust optical properties and determination of particle size and microphysical parameters. *Atmos. Environ.*, **50**, 66–78, https://doi.org/10.1016/j.atmosenv.2011.12.061.

Dubovik, O., B. Holben, T. F. Eck, A. Smirnov, Y. J. Kaufman, M. D. King, D. Tanré, and I. Slutsker, 2002: Variability of absorption and optical properties of key aerosol types observed in worldwide locations. *J. Atmos. Sci.*, **59**, 590–608, 10.1175/1520-0469(2002)059<0590:VOAAOP>2.0.CO;2.

Dubovik, O., A. Sinyuk, T. Lapyonok, B. N. Holben, M. Mishchenko, P. Yang, T. F. Eck, H. Volten, O. Muñoz, B. Veihelmann, W. J. van der Zande, J.-F. Leon, M. Sorokin, and I. Slutsker, 2006: Application of spheroid models to account for aerosol particle nonsphericity in remote sensing of desert dust. *J. Geophys. Res.*, **111**, 10.1029/2005JD006619.

Dubovik, O., A. Smirnov, B. N. Holben, M. D. King, Y. J. Kaufman, T. F. Eck, and I. Slutsker, 2000: Accuracy assessments of aerosol optical properties retrieved from Aerosol Robotic Network (AERONET) Sun and sky radiance measurements. *J. Geophys. Res.*, **105**, 9791–9806, 10.1029/2000JD900040.

Duda, D. P., P. Minnis, K. Khlopenkov, T. L. Chee, and R. Boeke, 2013: Estimation of 2006 Northern Hemisphere contrail coverage using MODIS data. *Geophys. Res. Lett.*, **40**, 612–617, 10.1002/grl.50097.

Eck, T. F., B. N. Holben, J. S. Reid, O. Dubovik, A. Smirnov, N. T. O'Neill, I. Slutsker, and S. Kinne, 1999: Wavelength dependence of the optical depth of biomass burning, urban, and desert dust aerosols. *J. Geophys. Res.*, **104**, 10.1029/1999JD900923.

Eck, T. F., B. N. Holben, O. Dubovik, A. Smirnov, P. Goloub, H. B. Chen, B. Chatenet, L. Gomes, X.-Y. Zhang, S.-C. Tsay, Q. Ji, D. Giles, and I. Slutsker, 2005: Columnar aerosol optical properties at AERONET sites in central eastern Asia and aerosol transport to the tropical mid-Pacific. *J. Geophys. Res.*, **110**, 10.1029/2004JD005274.

Eck, T. F., B. N. Holben, J. S. Reid, A. Sinyuk, E. J. Hyer, N. T. O'Neill, G. E. Shaw, J. R. Vande Castle, F. S. Chapin, O. Dubovik, A. Smirnov, E. Vermote, J. S. Schafer, D. Giles, I. Slutsker, M. Sorokine, and W. W. Newcomb, 2009: Optical properties of boreal region biomass burning aerosols in central Alaska and seasonal variation of aerosol optical depth at an Arctic coastal site. *J. Geophys. Res.*, **114**, 10.1029/2008JD010870.

Eck, T. F., B. N. Holben, A. Sinyuk, R. T. Pinker, P. Goloub, H. Chen, B. Chatenet, Z. Li, and coauthors, 2010: Climatological aspects of the optical properties of fine/coarse mode aerosol mixtures. *J. Geophys. Res.*, **115**, 10.1029/2010JD014002.

Eloranta, E. E., 2005: *High Spectral Resolution Lidar*, in: LIDAR: Range–Resolved Optical Remote Sensing of

the Atmosphere, ed. by C. Weitkamp, Springer. 143–163.

Engelmann, R., T. Kanitz, H. Baars, B. Heese, D. Althausen, A. Skupin, U. Wandinger, M. Komppula, I. S. Stachlewska, V. Amiridis, E. Marinou, I. Mattis, H. Linné, and A. Ansmann, 2016: The automated multiwavelength Raman polarization and water-vapor lidar Polly^{XT}: the neXT generation. *Atmos. Meas. Techn.*, **9**, 1767–1784, 10.5194/amt-9-1767-2016.

Fahey, D. W., R. S. Gao, K. S. Carslaw, J. Kettleborough, P. J. Popp, M. J. Northway, J. C. Holecek, S. C. Ciciora, R. J. McLaughlin, T. L. Thompson, R. H. Winkler, D. G. Baumgardner, B. Gandrud, P. O. Wennberg, S. Dhaniyala, K. McKinney, T. Peter, R. J. Salawitch, T. P. Bui, J. W. Elkins, C. R. Webster, E. L. Atlas, H. Jost, J. C. Wilson, R. L. Herman, A. Kleinböhl, and M. von König, 2001: The detection of large HNO3-containing particles in the winter Arctic stratosphere. *Science*, **291**, 1026–1031, 10.1126/science.1057265.

Fernald, F. G., 1984: Analysis of atmospheric lidar observations: Some comments. *Appl. Opt.*, **23**, 10.1364/AO.23.000652.

Freudenthaler, V., 2016: About the effects of polarising optics on lidar signals and the △90 calibration. *Atmos. Meas. Techn.*, **9**, 4181–4255, 10.5194/amt-9-4181-2016.

Freudenthaler, V., M. Esselborn, M. Wiegner, B. Heese, M. Tesche, A. Ansmann, D. Müller, D. Althausen, M. Wirth, A. Fix, G. Ehret, P. Knippertz, C. Toledano, J. Gasteiner, M. Garhammer, and M. Seefeldner, 2009: Depolarization–ratio profiling at several wavelengths in pure Saharan dust during SAMUM 2006. *Tellus*, **61B**, 10.1111/j.1600-0889.2008.00396.x.

Gasteiger, J., M. Wiegner, C. Toledano, S. Groß, V. Freudenthaler, M. Tesche, and K. Kandler, 2011: Modelling of scattering properties of non–spherical particles. *Tellus*, **63B**, 725–741, 10.1111/j.1600-0889.2011.00559.x.

Gierens, K., 2012: Selected topics on the interaction between cirrus clouds and embedded contrails. *Atmos. Chem. Phys.*, **12**, 11943–11949, 10.5194/acp-12-11943-2012.

Giles, D. M., B. N. Holben, T. F. Eck, A. Sinyuk, A. Smirnov, I. Slutsker, R. R. Dickerson, A. M. Thompson, and J. S. Schafer, 2012: An analysis of AERONET aerosol absorption properties and classifications representative of aerosol source regions. *J. Geophys. Res.*, **117**, 10.1029/2012JD018127.

Giles, D. M., A. Sinyuk, M. G. Sorokin, J. S. Schafer, A. Smirnov, I. Slutsker, T. F. Eck, B. N. Holben, J. R. Lewis, J. R. Campbell, E. J. Welton, S. V. Korkin, and A. I. Lyapustin, 2019: Advancements in the Aerosol Robotic Network (AERONET) Version 3 database – automated near-real-time quality control algorithm with improved cloud screening for Sun photometer aerosol optical depth (AOD) measurements. *Atmos. Meas. Techn.*, **12**, 169–209, 10.5194/amt-12-169-2019.

Groß, S., V. Freudenthaler, M. Wiegner, A. Greiß, M. Tesche, J. Gasteiger, A. Schladitz, and C. Toledano, 2011b: Characterization of the planetary boundary layer during SAMUM–2 by means of lidar measurements. *Tellus*, **63B**, 695–705, 10.1111/j.1600-0889.2011.00557.x.

Groß, S., M. Esselborn, B. Weinzierl, M. Wirth, A. Fix, and A. Petzold, 2013: Aerosol classification by airborne High Spectral Resolution Lidar observations. *Atmos. Chem. Phys.*, **13**, 2487–2505, 10.5194/acp-13-2487-2013.

Haarig, M., R. Engelmann, A. Ansmann, I. Veselovskii, D. N. Whiteman, and D. Althausen, 2016: 1064 nm rotational Raman lidar for particle extinction and lidar-ratio profiling: Cirrus case study. *Atmos. Meas. Techn.*, **9**, 4269–4278, 10.5194/amt-9-4269-2016.

Haarig, M., A. Ansmann, D. Althausen, A. Klepel, S. Groß, V. Freudenthaler, C. Toledano, R.-E. Mamouri, D. A. Farrell, D. A. Prescod, E. Marinou, S. P. Burton, J. Gasteiger, R. Engelmann, and H. Baars, 2017a: Triple-wavelength depolarization-ratio profiling of Saharan dust over Barbados during SALTRACE in 2013 and 2014. *Atmos. Chem. Phys.*, **17**, 10767–10794, 10.5194/acp-17-10767-2017.

Haarig, M., A. Ansmann, J. Gasteiger, K. Kandler, D. Althausen, H. Baars, M. Radenz, and D. A. Farrell, 2017b: Dry versus wet marine particle optical properties: RH dependence of depolarization ratio, backscatter, and extinction from multiwavelength lidar measurements during SALTRACE. *Atmos. Chem. Phys.*, **17**, 14199–14217, 10.5194/acp-17-14199-2017.

Haarig, M., A. Ansmann, H. Baars, C. Jimenez, I. Veselovskii, R. Engelmann, and D. Althausen, 2018: Depolarization and lidar ratios at 355, 532, and 1064 nm and microphysical properties of aged tropospheric and stratospheric Canadian wildfire smoke. *Atmos. Chem. Phys.*, **18**, 11847–11861, 10.5194/acp-18-11847-2018.

Haarig, M., A. Walser, A. Ansmann, M. Dollner, D. Althausen, D. Sauer, D. Farrell, and B. Weinzierl, 2019: CCN concentration and INP-relevant aerosol profiles in the Saharan Air Layer over Barbados from polarization lidar and airborne in situ measurements. *Atmos. Chem. Phys.*, **19**, 13773–13788, 10.5194/acp-19-13773-2019.

Hair, J. W., C. A. Hostetler, A. L. Cook, D. B. Harper, R. A. Ferrare, T. L. Mack, W. Welch, L. R. Izquierdo, and F. E. Hovis, 2008: Airborne High Spectral Resolution Lidar for profiling aerosol optical properties. *Appl. Opt.*,

47, 6734–6752, 10.1364/AO.47.006734.

Hess, M., P. Koepke, and I. Schult, 1998: Optical Properties of Aerosols and Clouds: The Software Package OPAC. *Bull. Am. Meteorol. Soc.*, **79**, 831–844, 10.1175/1520-0477(1998)079<0831:OPOAAC>2.0.CO;2.

Holben, B. N., T. F. Eck, I. Slutsker, D. Tanré, J. P. Buis, A. Setzer, E. Vermote, J. A. Reagan, Y. J. Kaufman, T. Nakajima, F. Lavenu, I. Jankowiak, and A. Smirnov, 1998: AERONET—A federated instrument network and data archive for aerosol characterization. *Remote Sens. Environm.*, **66**, 10.1016/S0034-4257(98)00031-5.

Holben, B. N., D. Tanré, A. Smirnov, T. F. Eck, I. Slutsker, N. Abuhassan, W. W. Newcomb, J. S. Schafer, B. Chatenet, F. Lavenu, Y. J. Kaufman, J. V. Castle, A. Setzer, B. Markham, D. Clark, R. Frouin, R. Halthore, A. Karneli, N. T. O'Neill, C. Pietras, R. T. Pinker, K. Voss, and G. Zibordi, 2001: An emerging ground-based aerosol climatology: Aerosol optical depth from AERONET. *J. Geophys. Res.*, **106**, 12067–12097, 10.1029/2001JD900014.

Hu, Q., P. Goloub, I. Veselovskii, J.-A. Bravo-Aranda, I. E. Popovici, T. Podvin, M. Haeffelin, A. Lopatin, O. Dubovik, C. Pietras, X. Huang, B. Torres, and C. Chen, 2019: Long-range-transported Canadian smoke plumes in the lower stratosphere over northern France. *Atmos. Chem. Phys.*, **19**, 1173–1193, 10.5194/acp-19-1173-2019.

Illingworth, A. J., H. W. Barker, A. Beljaars, M. Ceccaldi, H. Chepfer, N. Clerbaux, J. Cole, J. Delanoë, C. Domenech, D. P. Donovan, S. Fukuda, M. Hirakata, R. J. Hogan, A. Huenerbein, P. Kollias, T. Kubota, T. Nakajima, T. Y. Nakajima, T. Nishizawa, Y. Ohno, H. Okamoto, R. Oki, K. Sato, M. Satoh, M. W. Shephard, A. Velázquez-Blázquez, U. Wandinger, T. Wehr, and G.-J. van Zadelhoff, 2015: The EarthCARE Satellite: The next step forward in global measurements of clouds, aerosols, precipitation, and radiation. *Bull. Am. Meteorol. Soc.*, **96**, 1311–1332, 10.1175/BAMS-D-12-00227.1.

Inness, A., F. Baier, A. Benedetti, I. Bouarar, S. Chabrillat, H. Clark, C. Clerbaux, P. Coheur, R. J. Engelen, Q. Errera, J. Flemming, M. George, C. Granier, J. Hadji-Lazaro, V. Huijnen, D. Hurtmans, L. Jones, J. W. Kaiser, J. Kapsomenakis, K. Lefever, J. Leitão, M. Razinger, A. Richter, M. G. Schultz, A. J. Simmons, M. Suttie, O. Stein, J.-N. Thépaut, V. Thouret, M. Vrekoussis, C. Zerefos, and the MACC team, 2013: The MACC reanalysis: An 8 yr data set of atmospheric composition. *Atmos. Chem. Phys.*, **13**, 4073–4109, 10.5194/acp-13-4073-2013.

Iwabuchi, H., P. Yang, K. N. Liou, and P. Minnis, 2012: Physical and optical properties of persistent contrails: Climatology and interpretation. *J. Geophys. Res.*, **117**, 10.1029/2011JD017020.

Kacenelenbogen, M., M. A. Vaughan, J. Redemann, R. M. Hoff, R. R. Rogers, R. A. Ferrare, P. B. Russell, C. A. Hostetler, J. W. Hair, and B. N. Holben, 2011: An accuracy assessment of the CALIOP/CALIPSO version 2/version 3 daytime aerosol extinction product based on a detailed multi-sensor, multi-platform case study. *Atmos. Chem. Phys.*, **11**, 3981–4000, 10.5194/acp-11-3981-2011.

Kahnert, M., T. Nousiainen, and H. Lindqvist, 2014: Review: Model particles in atmospheric optics. *J. Quant. Spectr. Rad. Transf.*, **146**, 41–58, https://doi.org/10.1016/j.jqsrt.2014.02.014.

Kim, J., J. Lee, H. C. Lee, A. Higurashi, T. Takemura, and C. H. Song, 2007: Consistency of the aerosol type classification from satellite remote sensing during the Atmospheric Brown CloudEast Asia Regional Experiment campaign. *J. Geophys. Res.*, **112**, 10.1029/2006JD008201.

Kim, M.-H., A. H. Omar, J. L. Tackett, M. A. Vaughan, D. M. Winker, C. R. Trepte, Y. Hu, Z. Liu, L. R. Poole, M. C. Pitts, J. Kar, and B. E. Magill, 2018: The CALIPSO version 4 automated aerosol classification and lidar ratio selection algorithm. *Atmos. Meas. Techn.*, **11**, 6107–6135, 10.5194/amt-11-6107-2018.

Kittaka, C., D. M. Winker, M. A. Vaughan, A. Omar, and L. A. Remer, 2011: Intercomparison of column aerosol optical depths from CALIPSO and MODIS-Aqua. *Atmos. Meas. Techn.*, **4**, 131–141, 10.5194/amt-4-131-2011.

Klett, J. D., 1981: Stable analytical inversion solution for processing lidar returns. *Appl. Opt.*, **20**, 10.1364/AO.20.000211.

Klett, J. D., 1985: Lidar inversion with variable backscatter/extinction ratios. *Appl. Opt.*, **24**, 10.1364/AO.24.001638.

Lee, D. S., D. W. Fahey, P. M. Forster, P. J. Newton, R. C. Wit, L. L. Lim, B. Owen, and R. Sausen, 2009: Aviation and global climate change in the 21st century. *Atmos. Environ.*, **43**, 3520 – 3537, https://doi.org/10.1016/j.atmosenv.2009.04.024.

Lee, J., J. Kim, C. Song, S. Kim, Y. Chun, B. Sohn, and B. Holben, 2010: Characteristics of aerosol types from AERONET sunphotometer measurements. *Atmos. Environ.*, **44**, 3110– 3117, https://doi.org/10.1016/j.atmosenv.2010.05.035.

Liu, D., Z. Wang, Z. Liu, D. Winker, and C. Trepte, 2008a: A height resolved global view of dust aerosols from the first year CALIPSO lidar measurements. *J. Geophys. Res.*, **113**, 10.1029/2007JD009776.

Liu, Z., A. Omar, M. Vaughan, J. Hair, C. Kittaka, Y. Hu, K. Powell, C. Trepte, D. Winker, and coauthors, 2008b: CALIPSO lidar observations of the optical properties of Saharan dust: A case study of long–range transport. *J. Geophys. Res.*, **113**, 10.1029/2007JD008878.

Mamali, D., E. Marinou, J. Sciare, M. Pikridas, P. Kokkalis, M. Kottas, I. Binietoglou, A. Tsekeri, C. Keleshis, R. Engelmann, H. Baars, A. Ansmann, V. Amiridis, H. Russchenberg, and G. Biskos, 2018: Vertical profiles of aerosol mass concentration derived by unmanned airborne in situ and remote sensing instruments during dust events. *Atmos. Meas. Techn.*, **11**, 2897–2910, 10.5194/amt-11-2897-2018.

Mamouri, R. E., V. Amiridis, A. Papayannis, E. Giannakaki, G. Tsaknakis, and D. S. Balis, 2009: Validation of CALIPSO space-borne-derived attenuated backscatter coefficient profiles using a ground-based lidar in Athens, Greece. *Atmos. Meas. Techn.*, **2**, 513–522, 10.5194/amt-2-513-2009.

Mamouri, R. E. and A. Ansmann, 2014: Fine and coarse dust separation with polarization lidar. *Atmos. Meas. Techn.*, **7**, 3717–3735, 10.5194/amt-7-3717-2014.

— 2015: Estimated desert-dust ice nuclei profiles from polarization lidar: Methodology and case studies. *Atmos. Chem. Phys.*, **15**, 3463–3477, 10.5194/acp-15-3463-2015.

— 2016: Potential of polarization lidar to provide profiles of CCN- and INP-relevant aerosol parameters. *Atmos. Chem. Phys.*, **16**, 5905–5931, 10.5194/acp-16-5905-2016.

— 2017: Potential of polarization/Raman lidar to separate fine dust, coarse dust, maritime, and anthropogenic aerosol profiles. *Atmos. Meas. Techn.*, **10**, 3403–3427, 10.5194/amt-10-3403-2017.

Mamouri, R. E., A. Ansmann, A. Nisantzi, P. Kokkalis, A. Schwarz, and D. Hadjimitsis, 2013: Low Arabian dust extinction-to-backscatter ratio. *Geophys. Res. Lett.*, **40**, 4762–4766, 10.1002/grl.50898.

Marinou, E., M. Tesche, A. Nenes, A. Ansmann, J. Schrod, D. Mamali, A. Tsekeri, M. Pikridas, H. Baars, R. Engelmann, K.-A. Voudouri, S. Solomos, J. Sciare, S. Groß, F. Ewald, and V. Amiridis, 2019: Retrieval of ice-nucleating particle concentrations from lidar observations and comparison with UAV in situ measurements. *Atmos. Chem. Phys.*, **19**, 11315–11342, 10.5194/acp-19-11315-2019.

Massoli, P., M. Maturilli, and R. Neuber, 2006: Climatology of Arctic polar stratospheric clouds as measured by lidar in Ny-Ålesund, Spitsbergen (79°N, 12°E). *J. Geophys. Res.*, **111**, 10.1029/2005JD005840.

Mattis, I., M. Tesche, M. Grein, V. Freudenthaler, and D. Müller, 2009: Systematic error of lidar profiles caused by a polarization–dependent receiver transmission: quantification and error correction scheme. *Appl. Opt.*, **48**, 10.1364/AO.48.002742.

McGill, M. J., M. A. Vaughan, C. R. Trepte, W. D. Hart, D. L. Hlavka, D. M. Winker, and R. Kuehn, 2007: Airborne validation of spatial properties measured by the CALIPSO lidar. *J. Geophys. Res.*, **112**, 10.1029/2007JD008768.

Mie, G., 1908: Beiträge zur Optik trüber Medien, speziell kolloidaler Metallösungen. *Ann. Phys.*, **25**, 377–447.

Mielonen, T., A. Arola, M. Komppula, J. Kukkonen, J. Koskinen, G. de Leeuw, and K. E. J. Lehtinen, 2009: Comparison of CALIOP level 2 aerosol subtypes to aerosol types derived from AERONET inversion data. *Geophys. Res. Lett.*, **36**, 10.1029/2009GL039609.

Minnis, P., R. Palikonda, B. J. Walter, J. K. Ayers, and H. Mannstein, 2005: Contrail properties over the eastern North Pacific from AVHRR data. *Meteorologische Zeitschrift*, **14**, 515–523, 10.1127/0941-2948/2005/0056.

Minnis, P., U. Schumann, D. R. Doelling, K. M. Gierens, and D. W. Fahey, 1999: Global distribution of contrail radiative forcing. *Geophys. Res. Lett.*, **26**, 1853–1856, 10.1029/1999GL900358.

Mona, L., G. Pappalardo, A. Amodeo, G. D'Amico, F. Madonna, A. Boselli, A. Giunta, F. Russo, and V. Cuomo, 2009: One year of CNR-IMAA multi-wavelength Raman lidar measurements in coincidence with CALIPSO overpasses: Level 1 products comparison. *Atmos. Chem. Phys.*, **9**, 7213–7228, 10.5194/acp-9-7213-2009.

Müller, D., U. Wandinger, D. Althausen, I. Mattis, and A. Ansmann, 1998: Retrieval of physical particle properties from lidar observations of extinction and backscatter at multiple wavelengths. *Appl. Opt.*, **37**, 2260–2263, 10.1364/AO.37.002260.

Müller, D., U. Wandinger, D. Althausen, and M. Fiebig, 2001: Comprehensive particle characterization from three–wavelength Raman–lidar observations: Case study. *Appl. Opt.*, **40**, 10.1364/AO.40.004863.

Müller, D., I. Mattis, U. Wandinger, A. Ansmann, D. Althausen, O. Dubovik, S. Eckhardt, and A. Stohl, 2003: Saharan dust over a central European EARLINET–AERONET site: Combined observations with Raman lidar and Sun photometer. *J. Geophys. Res.*, **108**, 10.1029/2002JD002918.

Müller, D., I. Mattis, U. Wandinger, A. Ansmann, D. Althausen, and A. Stohl, 2005: Raman lidar observations of aged Siberian and Canadian forest fire smoke in the free troposphere over Germany in 2003: Microphysical particle characterization. *J. Geophys. Res.*, **110**, 10.1029/2004JD005756.

Müller, D., A. Ansmann, I. Mattis, M. Tesche, U. Wandinger, D. Althausen, and G. Pisani, 2007: Aerosol–type–dependent lidar ratio observed with Raman lidar. *J. Geophys. Res.*, **112**, 10.1029/2006JD008292.

Müller, D., B. Weinzierl, A. Petzold, K. Kandler, A. Ansmann, T. Müller, M. Tesche, V. Freudenthaler, M. Esselborn, B. Heese, D. Althausen, A. Schladitz, S. Otto, and P. Knippertz, 2010a: Mineral dust observed with AERONET Sun photometer, Raman lidar, and in situ instruments during SAMUM 2006: Shape–independent particle properties. *J. Geophys. Res.*, **115**, 10.1029/2009JD012520.

Müller, D., A. Ansmann, V. Freudenthaler, K. Kandler, C. Toledano, A. Hiebsch, J. Gasteiger, M. Esselborn, M. Tesche, B. Heese, D. Althausen, B. Weinzierl, A. Petzold, and W. von Hoyningen-Huene, 2010b: Mineral dust observed with AERONET Sun photometer, Raman lidar, and in situ instruments during SAMUM 2006: Shape–dependent particle properties. *J. Geophys. Res.*, **115**, 10.1029/2009JD012523.

Müller, D., K.-H. Lee, J. Gasteiger, M. Tesche, B. Weinzierl, K. Kandler, T. Müller, C. Toledano, S. Otto, D. Althausen, and A. Ansmann, 2012: Comparison of optical and microphysical properties of pure Saharan mineral dust observed with AERONET Sun photometer, Raman lidar, and in situ instruments during SAMUM 2006. *J. Geophys. Res.*, **117**, 10.1029/2011JD016825.

Müller, D., I. Veselovskii, A. Kolgotin, M. Tesche, A. Ansmann, and O. Dubovik, 2013: Vertical profiles of pure dust and mixed smoke-dust plumes inferred from inversion of multiwavelength Raman/polarization lidar data and comparison to AERONET retrievals and in situ observations. *Appl. Opt.*, **52**, 3178–3202, 10.1364/AO.52.003178.

Müller, D., C. A. Hostetler, R. A. Ferrare, S. P. Burton, E. Chemyakin, A. Kolgotin, J. W. Hair, A. L. Cook, D. B. Harper, R. R. Rogers, R. W. Hare, C. S. Cleckner, M. D. Obland, J. Tomlinson, L. K. Berg, and B. Schmid, 2014: Airborne Multiwavelength High Spectral Resolution Lidar (HSRL-2) observations during TCAP 2012: vertical profiles of optical and microphysical properties of a smoke/urban haze plume over the northeastern coast of the US. *Atmos. Meas. Techn.*, **7**, 3487–3496, 10.5194/amt-7-3487-2014.

Müller, D., E. Chemyakin, A. Kolgotin, R. A. Ferrare, C. A. Hostetler, and A. Romanov, 2019: Automated, unsupervised inversion of multiwavelength lidar data with TiARA: Assessment of retrieval performance of microphysical parameters using simulated data. *Appl. Opt.*, **58**, 4981–5008, 10.1364/AO.58.004981.

Niemand, M., O. Möhler, B. Vogel, H. Vogel, C. Hoose, P. Connolly, H. Klein, H. Bingemer, P. DeMott, J. Skrotzki, and T. Leisner, 2012: A particle-surface-area-based parameterization of immersion freezing on desert dust particles. *J. Atmos. Sci.*, **69**, 3077–3092, 10.1175/JAS-D-11-0249.1.

Nisantzi, A., R. E. Mamouri, A. Ansmann, G. L. Schuster, and D. G. Hadjimitsis, 2015: Middle East versus Saharan dust extinction-to-backscatter ratios. *Atmos. Chem. Phys.*, **15**, 7071–7084, 10.5194/acp-15-7071-2015.

Nousiainen, T. and K. Kandler, 2015: *Light Scattering Reviews 9*, Springer, chapter Light scattering by atmospheric mineral dust particles.

Omar, A. H., D. M. Winker, C. Kittaka, M. A. Vaughan, Z. Liu, Y. Hu, C. R. Trepte, R. R. Rogers, R. A. Ferrare, and coauthors, 2009: The CALIPSO automated aerosol classification and lidar ratio selection algorithm. *J. Atmos. Oceanic Technol.*, **26**, 10.1175/2009JTECHA1231.1.

O'Neill, N. T., T. F. Eck, A. Smirnov, B. N. Holben, and S. Thulasiraman, 2003: Spectral discrimination of coarse and fine mode optical depth. *J. Geophys. Res.*, **108**, 10.1029/2002JD002975.

Papayannis, A., R. E. Mamouri, V. Amiridis, E. Remoundaki, G. Tsaknakis, P. Kokkalis, I. Veselovskii, A. Kolgotin, A. Nenes, and C. Fountoukis, 2012: Optical-microphysical properties of Saharan dust aerosols and composition relationship using a multi-wavelength Raman lidar, in situ sensors and modelling: a case study analysis. *Atmos. Chem. Phys.*, **12**, 4011–4032, 10.5194/acp-12-4011-2012.

Pappalardo, G., A. Amodeo, A. Apituley, A. Comeron, V. Freudenthaler, H. Linné, A. Ansmann, J. Bösenberg, G. D'Amico, I. Mattis, L. Mona, U. Wandinger, V. Amiridis, L. Alados-Arboledas, D. Nicolae, and M. Wiegner, 2014: EARLINET: towards an advanced sustainable European aerosol lidar network. *Atmos. Meas. Techn.*, **7**, 2389–2409, 10.5194/amt-7-2389-2014.

Pappalardo, G., U. Wandinger, L. Mona, A. Hiebsch, I. Mattis, A. Amodeo, A. Ansmann, P. Seifert, H. Linné, A. Apituley, L. Alados Arboledas, D. Balis, A. Chaikovsky, G. D'Amico, F. De Tomasi, V. Freudenthaler, E. Giannakaki, A. Giunta, I. Grigorov, M. Iarlori, F. Madonna, R.-E. Mamouri, L. Nasti, A. Papayannis, A. Pietruczuk, M. Pujadas, V. Rizi, F. Rocadenbosch, F. Russo, F. Schnell, N. Spinelli, X. Wang, and M. Wiegner, 2010: EARLINET correlative measurements for CALIPSO: First intercomparison results. *J. Geophys. Res.*, **115**, 10.1029/2009JD012147.

Peter, T., 1997: MIicrophysics and heteorogeneous chemistry of Polar Stratospheric Clouds. *Annual Review of Physical Chemistry*, **48**, 785–822, 10.1146/annurev.physchem.48.1.785, pMID: 15012456.

Pitts, M. C., L. R. Poole, and L. W. Thomason, 2009: CALIPSO polar stratospheric cloud observations: Second-generation detection algorithm and composition discrimination. *Atmos. Chem. Phys.*, **9**, 7577–7589, 10.5194/acp-9-7577-2009.

Pitts, M. C., L. R. Poole, A. Dörnbrack, and L. W. Thomason, 2011: The 20092010 Arctic Polar Stratospheric Cloud season: A CALIPSO perspective. *Atmos. Chem. Phys.*, **11**, 2161–2177, 10.5194/acp-11-2161-2011.

Pitts, M. C., L. R. Poole, A. Lambert, and L. W. Thomason, 2013: An assessment of CALIOP Polar Stratospheric Cloud composition classification. *Atmos. Chem. Phys.*, **13**, 2975–2988, 10.5194/acp-13-2975-2013.

Pitts, M. C., L. R. Poole, and R. Gonzalez, 2018: Polar Stratospheric Cloud climatology based on CALIPSO spaceborne lidar measurements from 2006 to 2017. *Atmos. Chem. Phys.*, **18**, 10881–10913, 10.5194/acp-18-10881-2018.

Poole, L. R. and M. P. McCormick, 1988: Airborne lidar observations of Arctic polar stratospheric clouds: Indications of two distinct growth stages. *Geophys. Res. Lett.*, **15**, 21–23, 10.1029/GL015i001p00021.

Redemann, J., M. A. Vaughan, Q. Zhang, Y. Shinozuka, P. B. Russell, J. M. Livingston, M. Kacenelenbogen, and L. A. Remer, 2012: The comparison of MODIS-Aqua (C5) and CALIOP (V2 & V3) aerosol optical depth. *Atmos. Chem. Phys.*, **12**, 3025–3043, 10.5194/acp-12-3025-2012.

Reid, J. S., P. V. Hobbs, R. J. Ferek, D. R. Blake, J. V. Martins, M. R. Dunlap, and C. Liousse, 1998: Physical, chemical, and optical properties of regional hazes dominated by smoke in Brazil. *J. Geophys. Res.*, **103**, 32059–32080, 10.1029/98JD00458.

Reitebuch, O., 2012: *The Spaceborne Wind Lidar Mission ADM-Aeolus*, Springer Berlin Heidelberg, Berlin, Heidelberg. 815–827.

Rogers, R. R., C. A. Hostetler, J. W. Hair, R. A. Ferrare, Z. Liu, M. D. Obland, D. B. Harper, A. L. Cook, K. A. Powell, M. A. Vaughan, and D. M. Winker, 2011: Assessment of the CALIPSO lidar 532 nm attenuated backscatter calibration using the NASA LaRC airborne High Spectral Resolution Lidar. *Atmos. Chem. Phys.*, **11**, 1295–1311, 10.5194/acp-11-1295-2011.

Santecesaria, V., A. R. MacKenzie, and L. Stefanutti, 2001: A climatological study of Polar Stratospheric Clouds (1989–1997) from LIDAR measurements over Dumont d'Urville (Antarctica). *Tellus*, **53B**, 306–321, 10.1034/j.1600-0889.2001.01155.x.

Sasano, Y., E. V. Browell, and S. Ismail, 1985: Error caused by using a constant extinction/backscattering ratio in the lidar solution. *Appl. Opt.*, **24**, 10.1364/AO.24.003929.

Sassen, K., 2005: *Polarization in Lidar*, in: LIDAR: Range–Resolved Optical Remote Sensing of the Atmosphere, ed. by C. Weitkamp, Springer. 19–42.

Sassen, K., 1997: Contrail-Cirrus and Their Potential for Regional Climate Change. *Bull. Am. Meteorol. Soc.*, **78**, 1885–1904, 10.1175/1520-0477(1997)078<1885:CCATPF>2.0.CO;2.

Sawamura, P., R. H. Moore, S. P. Burton, E. Chemyakin, D. Müller, A. Kolgotin, R. A. Ferrare, C. A. Hostetler, L. D. Ziemba, A. J. Beyersdorf, and B. E. Anderson, 2017: HSRL-2 aerosol optical measurements and microphysical retrievals vs. airborne in situ measurements during DISCOVER-AQ 2013: an intercomparison study. *Atmos. Chem. Phys.*, **17**, 7229–7243, 10.5194/acp-17-7229-2017.

Schotland, R. M., K. Sassen, and R. Stone, 1971: Observations by lidar of linear depolarization ratios for hydrometeors. *J. Appl. Meteor*, **10**, 1011–1017.

Schrod, J., A. Danielczok, D. Weber, M. Ebert, E. S. Thomson, and H. G. Bingemer, 2016: Re-evaluating the Frankfurt isothermal static diffusion chamber for ice nucleation. *Atmos. Meas. Techn.*, **9**, 1313–1324, 10.5194/amt-9-1313-2016.

Schrod, J., D. Weber, J. Drücke, C. Keleshis, M. Pikridas, M. Ebert, B. Cvetković, S. Nickovic, E. Marinou, H. Baars, A. Ansmann, M. Vrekoussis, N. Mihalopoulos, J. Sciare, J. Curtius, and H. G. Bingemer, 2017: Ice nucleating particles over the Eastern Mediterranean measured by unmanned aircraft systems. *Atmos. Chem. Phys.*, **17**, 4817–4835, 10.5194/acp-17-4817-2017.

Schumann, U., 2005: Formation, properties and climatic effects of contrails. *Comptes Rendus Physique*, **6**, 549–565, https://doi.org/10.1016/j.crhy.2005.05.002, aircraft trailing vortices.

— 2012: A contrail cirrus prediction model. *Geosci. Mod. Dev.*, **5**, 543–580, 10.5194/gmd-5-543-2012.

Schuster, G. L., O. Dubovik, and B. N. Holben, 2006: Angstrom exponent and bimodal aerosol size distributions. *J. Geophys. Res.*, **111**, 10.1029/2005JD006328.

Schuster, G. L., M. Vaughan, D. MacDonnell, W. Su, D. Winker, O. Dubovik, T. Lapyonok, and C. Trepte, 2012: Comparison of CALIPSO aerosol optical depth retrievals to AERONET measurements, and a climatology for the lidar ratio of dust. *Atmos. Chem. Phys.*, **12**, 7431–7452, 10.5194/acp-12-7431-2012.

Shimizu, A., N. Sugimoto, I. Matsui, K. Arao, I. Uno, T. Muramaya, N. Kagawa, K. Aoki, A. Uchiyama, and A. Yamazaki, 2004: Continuous observations of Asian dust and other aerosols by polarization lidars in China and Japan during ACE–Asia. *J. Geophys. Res.*, **109**, 10.1029/2002JD003253.

Shin, S.-K., M. Tesche, K. Kim, M. Kezoudi, B. Tatarov, D. Müller, and Y. Noh, 2018: On the spectral depolarisation and lidar ratio of mineral dust provided in the AERONET version 3 inversion product. *Atmos. Chem. Phys.*, **18**, 12735–12746, 10.5194/acp-18-12735-2018.

Shin, S.-K., M. Tesche, D. Müller, and Y. Noh, 2019a: Technical note: Absorption aerosol optical depth components from AERONET observations of mixed dust plumes. *Atmos. Meas. Techn.*, **12**, 607–618, 10.5194/amt-12-607-2019.

Shin, S.-K., M. Tesche, Y. Noh, and D. Müller, 2019b: Aerosol-type classification based on AERONET version 3 inversion products. *Atmos. Meas. Techn.*, **12**, 3789–3803, 10.5194/amt-12-3789-2019.

Sinyuk, A., B. N. Holben, T. F. Eck, D. M. Giles, I. Slutsker, S. Korkin, J. S. Schafer, A. Smirnov, M. Sorokin, and A. Lyapustin, 2020: The AERONET Version 3 aerosol retrieval algorithm, associated uncertainties and comparisons to Version 2. *Atmos. Meas. Techn. Disc.*, **2020**, 1–80, 10.5194/amt-2019-474.

Solomos, S., A. Ansmann, R.-E. Mamouri, I. Binietoglou, P. Patlakas, E. Marinou, and V. Amiridis, 2017: Remote sensing and modelling analysis of the extreme dust storm hitting the Middle East and eastern Mediterranean in September 2015. *Atmos. Chem. Phys.*, **17**, 4063–4079, 10.5194/acp-17-4063-2017.

Stein, B., C. Wedekind, H. Wille, F. Immler, M. Müller, L. Wöste, M. del Guasta, M. Morandi, L. Stefanutti, A. Antonelli, P. Agostini, V. Rizi, G. Readelli, V. Mitev, R. Matthey, R. Kivi, and E. Kyrö, 1999: Optical classification, existence temperatures, and coexistence of different Polar Stratospheric Cloud types. *J. Geophys. Res.*, **104**, 23983–23993, 10.1029/1999JD900064.

Steinke, I., C. Hoose, O. Möhler, P. Connolly, and T. Leisner, 2015: A new temperature- and humidity-dependent surface site density approach for deposition ice nucleation. *Atmos. Chem. Phys.*, **15**, 3703–3717, 10.5194/acp-15-3703-2015.

Stier, P., 2016: Limitations of passive remote sensing to constrain global cloud condensation nuclei. *Atmos. Chem. Phys.*, **16**, 6595–6607, 10.5194/acp-16-6595-2016.

Stubenrauch, C. J. and U. Schumann, 2005: Impact of air traffic on cirrus coverage. *Geophys. Res. Lett.*, **32**, 10.1029/2005GL022707.

Sugimoto, N., I. Uno, M. Nishikawa, A. Shimizu, I. Matsui, X. Dong, Y. Chen, and H. Quan, 2003: Record heavy Asian dust in Beijing in 2002: Observations and model analysis of recent events. *Geophys. Res. Lett.*, **30**, 10.1029/2002GL016349.

Tabazadeh, A. and O. B. Toon, 1996: The presence of metastable HNO3/H2O solid phases in the stratosphere inferred from ER 2 data. *J. Geophys. Res.*, **101**, 9071–9078, 10.1029/96JD00062.

Tesche, M., D. Müller, A. Ansmann, M. Hu, and Y. Zhang, 2008: Retrieval of microphysical properties of aerosol particles from one–wavelength Raman lidar and multiwavelength Sun photometer observations. *Atmos. Environ.*, **42**, 10.1016/j.atmosenv.2008.02.014.

Tesche, M., A. Ansmann, D. Müller, D. Althausen, I. Mattis, B. Heese, V. Freudenthaler, M. Wiegner, M. Esselborn, G. Pisani, and P. Knippertz, 2009a: Vertical profiling of Saharan dust with Raman lidars and airborne HSRL in southern Morocco during SAMUM. *Tellus*, **61B**, 10.1111/j.1600-0889.2008.00390.x.

Tesche, M., A. Ansmann, D. Müller, D. Althausen, R. Engelmann, V. Freudenthaler, and S. Groß, 2009b: Vertically resolved separation of dust and smoke over Cape Verde by using multiwavelength Raman and polarization lidars during Saharan Mineral Dust Experiment 2008. *J. Geophys. Res.*, **114**, 10.1029/2009JD011862.

Tesche, M., A. Ansmann, D. Müller, D. Althausen, S. Groß, V. Freudenthaler, and M. Esselborn, 2011a: Profiling of Saharan dust and biomass–burning smoke with multiwavelength polarization Raman lidar at Cape Verde. *Tellus*, **63B**, 649–676, 10.1111/j.1600-0889.2011.00548.x.

Tesche, M., A. Ansmann, D. Müller, A. Althausen, I. Mattis, V. Freudenthaler, S. Groß, B. Weinzierl, and A. Petzold, 2011b: Optical and microphysical properties of smoke over Cape Verde inferred from multiwavelength lidar measurements. *Tellus*, **63B**, 677–694, 10.1111/j.1600-0889.2011.00549.x.

Tesche, M., 2011: *Vertical profiling of aerosol optical properties with multiwavelength aerosol lidar during the Saharan Mineral Dust Experiments*. Ph.D. Thesis, Universität Leipzig.
URL `https://nbn-resolving.org/urn:nbn:de:bsz:15-qucosa-71257`

Tesche, M., P. Glantz, C. Johansson, M. Norman, A. Hiebsch, A. Ansmann, D. Althausen, R. Engelmann, and P. Seifert, 2012: Volcanic ash over Scandinavia originating from the Grímsvötn eruptions in May 2011. *J. Geophys. Res.*, **117**, 10.1029/2011JD017090.

Tesche, M., U. Wandinger, A. Ansmann, D. Althausen, D. Müller, and A. H. Omar, 2013: Ground-based validation of CALIPSO observations of dust and smoke in the Cape Verde region. *J. Geophys. Res.*, **118**, 2889–2902, 10.1002/jgrd.50248.

Tesche, M., P. Zieger, N. Rastak, R. J. Charlson, P. Glantz, P. Tunved, and H.-C. Hansson, 2014: Reconciling aerosol light extinction measurements from spaceborne lidar observations and in situ measurements in the Arctic. *Atmos. Chem. Phys.*, **14**, 7869–7882, 10.5194/acp-14-7869-2014.

Tesche, M., P. Achtert, P. Glantz, and K. J. Noone, 2016: Aviation effects on already-existing cirrus clouds. *Nature Communications*, **7**, 10.1038/ncomms12016.

Tesche, M., A. Kolgotin, M. Haarig, S. P. Burton, R. A. Ferrare, C. A. Hostetler, and D. Müller, 2019: $3 + 2 + X$: what is the most useful depolarization input for retrieving microphysical properties of non-spherical particles from lidar measurements using the spheroid model of Dubovik et al. (2006)? *Atmos. Meas. Techn.*, **12**, 4421–4437, 10.5194/amt-12-4421-2019.

Toon, O. B., P. Hamill, R. P. Turco, and J. Pinto, 1986: Condensation of HNO3 and HCl in the winter polar stratospheres. *Geophys. Res. Lett.*, **13**, 1284–1287, 10.1029/GL013i012p01284.

Toon, O. B., A. Tabazadeh, E. V. Browell, and J. Jordan, 2000: Analysis of lidar observations of Arctic Polar Stratospheric Clouds during January 1989. *J. Geophys. Res.*, **105**, 20589–20615, 10.1029/2000JD900144.

Tsias, A., M. Wirth, K. S. Carslaw, J. Biele, H. Mehrtens, J. Reichardt, C. Wedekind, V. Weiß, W. Renger, R. Neuber, U. von Zahn, B. Stein, V. Santacesaria, L. Stefanutti, F. Fierli, J. Bacmeister, and T. Peter, 1999: Aircraft lidar observations of an enhanced type Ia polar stratospheric clouds during APE-POLECAT. *J. Geophys. Res.*, **104**, 23961–23969, 10.1029/1998JD100055.

Ullrich, R., C. Hoose, O. Möhler, M. Niemand, R. Wagner, K. Höhler, N. Hiranuma, H. Saathoff, and T. Leisner, 2017: A new ice nucleation active site parameterization for desert dust and soot. *J. Atmos. Sci.*, **74**, 699–717, 10.1175/JAS-D-16-0074.1.

van de Hulst, H. C., 1957: *Light Scattering by Small Particles*. Dover Publications, 470 pages.

Veselovskii, I., O. Dubovik, A. Kolgotin, T. Lapyonok, P. Di Girolamo, D. Summa, D. N. Whiteman, M. Mishchenko, and D. Tanré, 2010: Application of randomly oriented spheroids for retrieval of dust particle parameters from multiwavelength lidar measurements. *J. Geophys. Res.*, **115**, 10.1029/2010JD014139.

Veselovskii, I., A. Kolgotin, V. Griaznov, D. Müller, U. Wandinger, and D. N. Whiteman, 2002: Inversion with regularization for the retrieval of tropospheric aerosol parameters from multiwavelength Raman lidar sounding. *Appl. Opt.*, **41**, 10.1364/AO.41.003685.

Vogel, H., J. Förstner, B. Vogel, T. Hanisch, B. Mühr, U. Schättler, and T. Schad, 2014: Time-lagged ensemble simulations of the dispersion of the Eyjafjallajökull plume over Europe with COSMO-ART. *Atmos. Chem. Phys.*, **14**, 7837–7845, 10.5194/acp-14-7837-2014.

Voigt, C., U. Schumann, A. Minikin, A. Abdelmonem, A. Afchine, S. Borrmann, M. Boettcher, B. Buchholz, L. Bugliaro, A. Costa, J. Curtius, M. Dollner, A. Dörnbrack, V. Dreiling, V. Ebert, A. Ehrlich, A. Fix, L. Forster, F. Frank, D. Fütterer, A. Giez, K. Graf, J.-U. Grooß, S. Groß, K. Heimerl, B. Heinold, T. Hüneke, E. Järvinen, T. Jurkat, S. Kaufmann, M. Kenntner, M. Klingebiel, T. Klimach, R. Kohl, M. Krämer, T. C. Krisna, A. Luebke, B. Mayer, S. Mertes, S. Molleker, A. Petzold, K. Pfeilsticker, M. Port, M. Rapp, P. Reutter, C. Rolf, D. Rose, D. Sauer, A. Schäfler, R. Schlage, M. Schnaiter, J. Schneider, N. Spelten, P. Spichtinger, P. Stock, A. Walser, R. Weigel, B. Weinzierl, M. Wendisch, F. Werner, H. Wernli, M. Wirth, A. Zahn, H. Ziereis, and M. Zöger, 2017: ML-CIRRUS: The Airborne Experiment on Natural Cirrus and Contrail Cirrus with the High-Altitude Long-Range Research Aircraft HALO. *Bull. Am. Meteorol. Soc.*, **98**, 271–288, 10.1175/BAMS-D-15-00213.1.

Wandinger, U., D. Müller, C. Böckmann, D. Althausen, V. Matthias, J. Bösenberg, V. Weiß, M. Fiebig, M. Wendisch, A. Stohl, and A. Ansmann, 2002: Optical and microphysical characterization of biomass–burning and industrial pollution aerosols from multiwavelength lidar and aircraft measurements. *J. Geophys. Res.*, **107**, 10.1029/2000JD000202.

Wandinger, U., 2005a: *Introduction to Lidar*, in: LIDAR: Range–Resolved Optical Remote Sensing of the Atmosphere, ed. by C. Weitkamp, Springer. 1–18.

Wandinger, U., 2005b: *Raman Lidar*, in: LIDAR: Range–Resolved Optical Remote Sensing of the Atmosphere, ed. by C. Weitkamp, Springer. 241–271.

Wandinger, U., M. Tesche, P. Seifert, A. Ansmann, D. Müller, and D. Althausen, 2010: Size matters: Influence of multiple scattering on CALIPSO light–extinction profiling in desert dust. *Geophys. Res. Lett.*, **37**, 10.1029/2010GL042527.

Wandinger, U., H. Baar, R. E. A. Hünerbein, S. Horn, T. Kanitz, D. Donovan, G. van Zadelhoff, D. Daou, J. Fischer, J. von Bismarck, F. Filipitsch, N. Docter, M. Eisinger, D. Lajas, and T. Wehr, 2016: HETEAC: The Aerosol

Classification Model for EarthCARE. *EPJ Web of Conferences*, **119**, 01004, 10.1051/epjconf/201611901004.

Wandinger, U., V. Freudenthaler, H. Baars, A. Amodeo, R. Engelmann, I. Mattis, S. Groß, G. Pappalardo, A. Giunta, G. D'Amico, A. Chaikovsky, F. Osipenko, A. Slesar, D. Nicolae, L. Belegante, C. Talianu, I. Serikov, H. Linné, F. Jansen, A. Apituley, K. M. Wilson, M. de Graaf, T. Trickl, H. Giehl, M. Adam, A. Comerón, C. Muñoz Porcar, F. Rocadenbosch, M. Sicard, S. Tomás, D. Lange, D. Kumar, M. Pujadas, F. Molero, A. J. Fernández, L. Alados-Arboledas, J. A. Bravo-Aranda, F. Navas-Guzmán, J. L. Guerrero-Rascado, M. J. Granados-Muñoz, J. Preißler, F. Wagner, M. Gausa, I. Grigorov, D. Stoyanov, M. Iarlori, V. Rizi, N. Spinelli, A. Boselli, X. Wang, T. Lo Feudo, M. R. Perrone, F. De Tomasi, and P. Burlizzi, 2016: EARLINET instrument intercomparison campaigns: overview on strategy and results. *Atmos. Meas. Techn.*, **9**, 1001–1023, 10.5194/amt-9-1001-2016.

Weinzierl, B., A. Ansmann, J. M. Prospero, D. Althausen, N. Benker, F. Chouza, M. Dollner, D. Farrell, W. K. Fomba, V. Freudenthaler, J. Gasteiger, S. Groß, M. Haarig, B. Heinold, K. Kandler, T. B. Kristensen, O. L. Mayol-Bracero, T. Müller, O. Reitebuch, D. Sauer, A. Schäfler, K. Schepanski, A. Spanu, I. Tegen, C. Toledano, and A. Walser, 2017: The Saharan Aerosol Long-Range Transport and AerosolCloud-Interaction Experiment: Overview and selected highlights. *Bull. Am. Meteorol. Soc.*, **98**, 1427–1451, 10.1175/BAMS-D-15-00142.1.

Weitkamp, C., Ed., 2005: *LIDAR: Range–resolved optical remote sensing of the atmosphere*. Springer, 460 pages.

Winker, D. M., M. A. Vaughan, A. Omar, Y. Hu, K. A. Powell, Z. Liu, W. H. Hunt, and S. A. Young, 2009: Overview of the CALIPSO mission and CALIOP data processing algorithms. *J. Atmos. Oceanic Technol.*, **26**, 10.1175/2009JTECHA1281.1.

Winker, D. M., J. Pelon, J. A. Coakley, S. A. Ackerman, R. J. Charlson, P. R. Colarco, P. Flamant, Q. Fu, R. M. Hoff, C. Kittaka, T. L. Kubar, H. Le Treut, M. P. Mccormick, G. Mégie, L. Poole, K. Powell, C. Trepte, M. A. Vaughan, and B. A. Wielicki, 2010: The CALIPSO Mission. *Bull. Am. Meteorol. Soc.*, **91**, 1211–1230, 10.1175/2010BAMS3009.1.

About the Author

Curriculum Vitae

Matthias Tesche
Leipzig Institute for Meteorology   phone: +49 (0)341 97 36660
Leipzig University   matthias.tesche@uni-leipzig.de
Stephanstrasse 3   https://home.uni-leipzig.de/mtesche/personal
04103 Leipzig
Germany

Work experience

since 01/2019	Research Group leader Aerosols and Clouds, Leipzig Institute for Meteorology (LIM), University of Leipzig, Germany
2017/03 – 2019/09	Senior Lecturer at the School of Physics, Astronomy and Mathematics (PAM) at the University of Hertfordshire, United Kingdom
2015/10 – 2017/02	Lecturer in Physics at the School of Physics, Astronomy and Mathematics (PAM) at the University of Hertfordshire, United Kingdom
2014/10 – 2015/09	Research Scientist in the Atmospheric Remote Sensing Laboratory at the School of Physics, Astronomy and Mathematics (PAM) at the University of Hertfordshire, United Kingdom
2011/06 – 2014/09	Post–Doc in the Atmospheric Research Unit at Department of Applied Environmental Science (ITM) of Stockholm University, Sweden
2011/03 – 2011/05	Research associate at Leibniz Institute for Tropospheric Research, Leipzig, Germany
2006/07 – 2011/02	PhD student at Leibniz Institute for Tropospheric Research, Leipzig, Germany
2003/10 – 2005/10	student Research assistant at Leibniz Institute for Tropospheric Research, Leipzig, Germany

Education

2011	Doctor Rerum Naturalium (*Dr. rer. nat.*) in Meteorology (grade *magna cum laude*), Thesis: *Vertical profiling of aerosol optical properties with multiwavelength aerosol lidar during the Saharan Mineral Dust Experiments*, Supervisor: Dr. Albert Ansmann
2006/07 – 2011/02	PhD student at Leibniz Institute for Tropospheric Research, Leipzig, Germany

2006	Diploma in Meteorology (grade *very good*; 1.3 on a range from 1.0 to 5.0), Thesis: *Optical and microphysical properties of aerosols in southern (Pearl River Delta) and northern China (Beijing) observed with Raman lidar and Sun photometer*, Supervisors: Dr. Albert Ansmann and Prof. Jost Heintzenberg
2000/10 – 2006/05	Study of meteorology at Leipzig Institute for Meteorology (LIM) of Leipzig University, Leipzig, Germany

Leave of Absence

2017/01 - 2017/03	paternity leave

measurement campaigns

2017/04	PRE-TECT and A-LIFE: *mineral dust profiling with balloon-borne OPCs* Finokalia, Crete and Paphos, Cyprus
2014/07 – 2014/09	CAESAR 2014: *Cloud Aerosol Experiment Åre*, Åre, Sweden
2011-2014, in Jan.	PSC measurements with the Esrange lidar, Esrange, Sweden
2010 – 2014	regular Raman lidar measurements at Stockholm, Sweden
2007 – 2010	CALIPSO validation: *measurements during CALIPSO overpasses*, Leipzig, Germany
2006 – 2010	EARLINET: *regular measurements according to the EARLINET schedule*, Leipzig, Germany
2009/05	EARLI09: *EARLINET Lidar Intercomparison 2009*, Leipzig, Germany
2008/05 – 2008/06	SAMUM–2: *Saharan Mineral Dust Experiment 2*, Phase 2, Praia, Cape Verde
2008/01 – 2008/02	SAMUM–2: *Saharan Mineral Dust Experiment 2*, Phase 1, Praia, Cape Verde
2007/05 – 2007/09	COPS: *Convective and Orographically Induced Precipitation Studies*, Black Forest, Germany
2006/05 – 2006/06	SAMUM–1: *Saharan Mineral Dust Experiment 1*, Ouarzazate, Morocco
2005/09 – 2005/10	LAUNCH–2005: *International Lindenberg Campaign for Assessment of Humidity and Cloud Profiling Systems and its Impact on High–Resolution Modeling*, Ziegendorf, Germany
2005/01	Raman lidar measurements at Beijing, China

Teaching experience

at Leipzig University
Demonstrator in the second year *Meteorologisches Praktikum* labs

at the University of Hertfordshire
Teaching in the framework of the fourth year course *An introduction to atmospheric physics*
Design and supervision of the laboratory exercises supporting the fourth year course *An introduction to atmospheric physics*

Demonstrator in the first year *Contemporary Physics* labs
Demonstrator in the first year *Laboratory Physics* labs
Module Tutor in the third year *Computational Physics* labs

at Stockholm University
Teaching in the framework of the MSc/PhD course *An introduction to atmospheric remote sensing*
Teaching in the framework of the MSc/PhD course *Aerosol, Clouds and Climate*

at Uppsala University
Lecture on *The lidar technique and applications for measurements of the planetary boundary layer*

Supervision

Post-Docs: Peggy Achtert (since 2019), Peter Bräuer (since 2019), Torsten Seelig (since 2019), Sung-Kyun Shin (2017–2019)
PhD students: Yuanyuan Hu (since 2020), Fani Alexandri (since 2019), Goutam Choudhury (since 2019), John Tolladay (since 2018), Maria Kezoudi (2016–2019, now at the Cyprus Institute, Nicosia, Cyprus)
MSc students: Therese Gadd (2015)
BSc students: Annika Burzik (2020), Hanna Weikert (2020), Ewa Johansson (2013)
student researchers: Pascal Hirsche, Hanna Weikert

Grants

2018: *Particles in Aerosol Cloud Interactions: stratification, CCN/INP concentrations, and Cloud lifecycle (PACIFIC)*, funded by a DAAD MOPGA-GRI Senior Research Project grant of 1.479.241 EUR
2016: *Profiling mineral dust size distributions in the eastern Mediterranean with the balloon-borne Universal Cloud and Aerosol Sonde System (UCASS)*, funded by a Royal Society Research Grant of 14.520 GBP
2013: *The influence of aircraft emissions on sub-visible cirrus clouds in the upper troposphere*, funded by the Swedish Science Foundation (Vetenskapsrådet), granted funding: 1.6 mio SEK, Co-applicant (main applicant: Prof. Kevin Noone)

small grants

NERC travel grant for participation in the MOSAiC implementation meeting in St Petersburg, Russia (2017)
ACTRIS-2 Trans-National Access to perform balloon-borne OPC measurements at Finokalia, Crete (2017)
Bolin Centre for Climate Research funding for an aerosol optical closure study at Stockholm University (2013)
travel grant for the International Laser Radar Conference (ILRC 24) in Boulder, Colorado (2008)
travel grant for the International Laser Radar Conference (ILRC 23) in Nara, Japan (2006)

Fellowships

since 02/2018: Fellow of the Royal Meteorological Society (FRMetS), United Kingdom
since 08/2015: Fellow of the Higher Education Academy (FHEA), United Kingdom

Commissions of trust

2020: Academy of Finland, research grant review panel Atmospheric Sciences
2019: Academy of Finland, research grant review panel Atmospheric Sciences
2018: main organiser of the 4th ACTRIS WP2 workshop in Hatfield, United Kingdom
2018: NERC Special Program Area scoping group: Reducing uncertainty in climate sensitivity due to clouds
2018: Scientific Committee of the first European Lidar Conference (www.elc2018.eu)
since 2014: Editorial Board of Atmospheric Chemistry and Physics (ACP)
since 2007: Reviewer for leading scientific journals in my field of research (about 10 reviews/year): *Applied Optics, Atmospheric Environment, Atmospheric Chemistry and Physics, Atmospheric Measurement Techniques, Atmospheric Research, Geophysical Research Letters, Geoscientific Model Development, Journal of Geophysical Research, Journal of Quantitative Spectroscopy and Radiative Transfer, Optics Express, Remote Sensing, Tellus B*
Reviewer for grant proposals submitted to NERC and Academy of Finland

Membership of scientific societies

since 2019: Deutsche Meteorologische Gesellschaft (DMG)
since 2018: Royal Meteorological Society (RMetS)
since 2015: American Geophysical Union (AGU)
since 2009: European Geosciences Union (EGU)

List of Publications

ORCID ID: https://orcid.org/0000-0003-0096-4785
Scopus Author ID: https://www.scopus.com/authid/detail.uri?authorId=15059495000
Research Gate: https://www.researchgate.net/profile/Matthias_Tesche
h-index of 40 from 79 peer-reviewed papers, Scopus, 23 January 2020

Glantz, P., E. Freud, C. Johansson, K. Noone, and **M. Tesche** (2019), Trends in MODIS and AERONET derived aerosol optical thickness over Northern Europe, *Tellus*, **71B**, 16000889.2018.1554414.

Marinou, E., **M. Tesche**, A. Nenes, A. Ansmann, J. Schrod, D. Mamali, A. Tsekeri, M. Pikridas, H. Baars, R. Engelmann, K.-A. Voudouri, S. Solomos, J. Sciare, S. Groß, and V. Amiridis (2019), Retrieval of ice-nucleating particle concentrations from lidar observations and comparison with UAV in situ measurements, *Atmos. Chem. Phys.*, **19**, 11315-11342, acp-19-11315-2019.

Shin, S.-K., **M. Tesche**, Y. Noh, and D. Müller (2019), Aerosol-type classification based on AERONET version 3 inversion products, *Atmos. Meas. Techn.*, **12**, 3789-3803, amt-12-3789-2019.

Shin, S.-K., **M. Tesche**, D. Müller, and Y. Noh (2019), Technical note: Absorption aerosol optical depth components from AERONET observations of mixed dust plumes, *Atmos. Meas. Techn.*, **12**, 607-618, amt-12-607-2019.

Tesche, M., A. Kolgotin, M. Haarig, S. P. Burton, R. A. Ferrare, C. A. Hostetler, and D. Müller (2019), 3+2+X: What is the most useful depolarisation input for retrieving microphysical properties of non-spherical particles from lidar measurements using the spheroid model of Dubovik et al. (2006)?, *Atmos. Meas. Techn.*, **12**, 4421-4437, amt-12-4421-2019.

Shin, S.-K., **M. Tesche**, K. Kim, M. Kezoudi, B. Tatarov, D. Müller, and Y. Noh (2018), On the spectral depolarisation and lidar ratio of mineral dust provided in the AERONET version 3 inversion product, *Atmos. Chem. Phys.*, **18**, 12735-12746, acp-18-12735-2018.

Tesche, M., B. Tatarov, Y. Noh, and D. Müller (2018), Lidar sprectroscopy instrument (LISSI): An infrastructure facility for chemical aerosol profiling at the University of Hertfordshire, EPJ Web of Conferences, 176, 10.1051/epjconf/201817601008.

Tesche, M., P. Glantz, and C. Johansson (2016), Spaceborne observations of low surface aerosol concentrations in the Stockholm region, *Tellus*, **68B**, tellusb.v68.28951.

Tesche, M., P. Achtert, P. Glantz, and K. Noone (2016), Aviation effects on already-existing cirrus clouds, *Nature Comms.*, **7**, NCOMMS12016.

Baars, H., T. Kanitz, R. Engelmann, D. Althausen, B. Heese, M. Komppula, J. Preißler, **M. Tesche**, A. Ansmann, U. Wandinger, J.-H. Lim, J. Y. Ahn, I. S. Stachlewska, V. Amiridis, E. Marinou, P. Seifert, J. Hofer, A. Skupin, F. Schneider, S. Bohlmann, A. Foth, S. Bley, A. Pfüller, E. Giannakaki, H. Lihavainen, Y. Viisanen, R. K. Hooda, S. Pereira, D. Bortoli, F. Wagner, I. Mattis, L. Janicka, K. M. Markowicz, P. Achtert, P. Artaxo, T. Pauliquevis, R. Souza, V. P. Sharma, P. G. van Zyl, J. P. Beukes, J. Sun, E. G. Rohwer, R. Deng, R. E. Mamouri, and F. Zamorano (2016), An overview of the first decade of Polly$^{\mathrm{NET}}$: An emerging network of automated Raman-polarization lidars for continuous aerosol profiling, *Atmos. Chem. Phys.*, **16**, 5111-5137, acp-16-5111-2016.

Zieger, P., P. P. Aalto, V. Aaltonen, M. Äijälä, J. Backman, J. Hong, M. Komppula, R. Krejci, M. Laborde, J. Lampilahti, G. de Leeuw, A. Pfüller, B. Rosati, **M. Tesche**, P. Tunved, R. Väänänen, and T. Petäjä (2015), Low hygroscopic scattering enhancement of boreal aerosol and the implications for a columnar optical closure study, *Atmos. Chem. Phys.*, **15**, 7247-7267, acp-15-7247-2015.

Achtert, P. and **M. Tesche** (2014), Assessing lidar-based classification schemes for Polar Stratospheric Clouds based on 16 years of lidar measurements at Esrange, Sweden, *J. Geophys. Res.*, **119**, 2013JD020355.

Glantz, P., A. E. Bourassa, A. Herber, T. Iversen, J. Karlsson, A. Kirkevåg, M. Maturilli, Ø. Seland, K. Stebel, H. Struthers, **M. Tesche**, and L. Thomason (2014), Remote sensing of aerosols in the Arctic for an evaluation of global climate model simulations, *J. Geophys. Res.*, **119**, 2013JD021279.

Rastak, N., S. Silvergren, P. Zieger, U. Wideqvist, J. Ström, B. Svenningsson, M. Maturilli, **M. Tesche**, A. M. L. Ekman, P. Tunved, and I. Riipinen (2014), Seasonal variation of aerosol water uptake and its impact on the direct radiative effect at Ny-Ålesund, Svalbard, *Atmos. Chem. Phys.*, **14**, acp-14-7445-2014.

Tesche, M., P. Zieger, N. Rastak, R. J. Charlson, P. Glantz, P. Tunved, and H.-C. Hansson (2014), Reconciling aerosol light extinction measurements from spaceborne lidar observations and in-situ measurements in the Arctic, *Atmos. Chem. Phys.*, **14**, acp-14-7869-2014.

Althausen, D., R. Engelmann, H. Baars, B. Heese, T. Kanitz, M. Komppula, E. Giannakaki, A. Pfüller, A. M. Silva, J. Preißler, F. Wagner, J. L. Rascado, S. Pereira, J.-H. Lim, J. Y. Ahn, **M. Tesche**, and I. S. Stachlewska (2013), PollyNET — A network of multiwavelength polarization Raman lidars, *Proceedings of SPIE*, **8894**, 12.2028921.

Müller, D., I. Veselovskiy, A. Kolgotin, **M. Tesche**, A. Ansmann, and O. Dubovik (2013), Vertical profiles of pure dust and mixed smoke-dust plumes inferred from inversion of multiwavelength Raman/polarization lidar data and comparison to AERONET retrievals and in situ observations, *Appl. Opt.*, **52**, AO.52.003178.

Pappalardo, G., L. Mona, G. D'Amico, U. Wandinger, M. Adam, A. Amodeo, A. Ansmann, A. Apituley, L. Alados Arboledas, D. Balis, A. Boselli, J. A. Bravo-Aranda, A. Chaikovsky, A. Comeron, J. Cuesta, F. De Tomasi, V. Freudenthaler, M. Gausa, E. Giannakaki, H. Giehl, A. Giunta, I. Grigorov, S. Groß, M. Haeffelin, A. Hiebsch, M. Iarlori, D. Lange, H. Linné, F. Madonna, I. Mattis, R.-E. Mamouri, M. A. P. McAuliffe, V. Mitev, F. Molero, F. Navas-Guzman, D. Nicolae, A. Papayannis, M. R. Perrone, C. Pietras, A. Pietruczuk, G. Pisani, J. Preißler, M. Pujadas, V. Rizi, A. A. Ruth, J. Schmidt, F. Schnell, P. Seifert, I. Serikov, M. Sicard, V. Simeonov, N. Spinelli, K. Stebel, **M. Tesche**,

T. Trickl, X. Wang, F. Wagner, M. Wiegner, and K. M. Wilson (2013), Four-dimensional distribution of the 2010 Eyjafjallajökull volcanic cloud over Europe observed by EARLINET, *Atmos. Chem. Phys.*, **13**, acp-13-4429-2013.

Tesche, M., U. Wandinger, A. Ansmann, D. Althausen, D. Müller, and A. Omar (2013), Ground–based validation of CALIPSO observations of dust and smoke in the Cape Verde region, *J. Geophys. Res.*, **118**, jgrd.50248.

Wagner, J., A. Ansmann, U.Wandinger, P. Seifert, A. Schwarz, **M. Tesche**, A. Chaikovsky, and O. Dubovik (2013), Evaluation of the lidar radiometer inversion code (LIRIC) to determine microphysical properties of volcanic and desert dust, *Atmos. Meas. Tech.*, **6**, 10.5194/amt-6-1707-2013.

Ansmann, A., P. Seifert, **M. Tesche**, and U. Wandinger (2012), Profiling of fine and coarse particle mass: Case studies of Saharan dust and Eyjafjallajökull/Grimsvötn volcanic plumes, *Atmos. Chem. Phys.*, **12**, acp-12-9399-2012.

Glantz, P. and **M. Tesche** (2012), Assessment of two aerosol optical thickness retrieval algorithms applied to MODIS Aqua and Terra measurements in Europe, *Atmos. Meas. Tech.*, **5**, amt-5-1727-2012.

Haustein, K., C. Pérez, J. M. Baldasano, O. Jorba, S. Basart, R. L. Miller, Z. Janjic, T. Black, S. Nickovic, M. C. Todd, R. Washington, D. Müller, **M. Tesche**, B. Weinzierl, M. Esselborn, and A. Schladitz (2012), Atmospheric dust modeling from meso to global scales with the online NMMB/BSC-Dust model—Part 2: Experimental campaigns in Northern Africa, *Atmos. Chem. Phys.*, **12**, acp-12-2933-2012.

Müller, D., K.–H. Lee, J. Gasteiger, **M. Tesche**, B. Weinzierl, K. Kandler, T. Müller, C. Toledano, S. Otto, D. Althausen, and A. Ansmann (2012), Comparison of optical and microphysical properties of pure Saharan mineral dust observed with AERONET sun photometer, Raman lidar, and in–situ instruments during SAMUM 2006, *J. Geophys. Res.*, **117**, 2011JD016825.

Tesche, M., P. Glantz, C. Johansson, M. Norman, A. Hiebsch, A. Ansmann, D. Althausen, R. Engelmann, and P. Seifert (2012), Volcanic ash over Scandinavia originating from the Grímsvötn eruptions in May 2011, *J. Geophys. Res.*, **117**, 2011JD017090.

Ansmann, A., **M. Tesche**, P. Seifert, S. Groß, V. Freudenthaler, A. Apituley, K. Wilson, I. Serikov, V. Linné, B. Heinold, A. Hiebsch, F. Schnell, J. Schmidt, I. Mattis, U. Wandinger, and M. Wiegner (2011), Ash and fine-mode particle mass profiles from EARLINET-AERONET observations over central Europe after the eruptions of the Eyjafjallajökull volcano in 2010, *J. Geophys. Res.*, **116**, 2010JD015567.

Engelmann, R., A. Ansmann, S. Horn, M. Esselborn, J. Fruntke, P. Seifert, D. Althausen, **M. Tesche**, and K. Lieke (2011), Doppler lidar studies of heat island effects on vertical mixing of aerosols during SAMUM–2, *Tellus*, **63B**, j.1600-0889.2011.00552.x.

Gasteiger, J., M. Wiegner, S. Groß, V. Freudenthaler, C. Toledano, **M. Tesche**, and K. Kandler (2011), Modeling lidar–relevant optical properties of complex mineral dust aerosols, *Tellus*, **63B**, j.1600-0889.2011.00559.x.

Groß, S., J. Gasteiger, V. Freudenthaler, M. Wiegner, A. Geiß, A. Schladitz, C. Toledano, K. Kandler, **M. Tesche**, A. Ansmann, and A. Wiedensohler (2011), Characterization of the planetary boundary layer during SAMUM–2 by means of lidar measurements, *Tellus*, **63B**, j.1600-0889.2011.00557.x.

Groß, S., **M. Tesche**, V. Freudenthaler, C. Toledano, M. Wiegner, A. Ansmann, D. Althausen, and M. Seefeldner (2011), Characterization of Saharan dust, marine aerosols and mixtures of biomass burning aerosols and dust by means of multi–wavelength depolarization- and Raman measurements during SAMUM–2, *Tellus*, **63B**, j.1600-0889.2011.00556.x.

Heinold, B., I. Tegen, M. Esselborn, V. Freudenthaler, S. Groß, K. Kandler, P. Knippertz, D. Müller, K. Schepanski, A. Schladitz, **M. Tesche**, C. Toledano, B. Weinzierl, A. Ansmann, D. Althausen, T. Müller, A. Petzold, and A. Wiedensohler (2011), Regional modeling of Saharan dust and land fire smoke: Model description and validation, *Tellus*, **63B**, j.1600-0889.2011.00570.x.

Herold, C., D. Althausen, D. Müller, **M. Tesche**, P. Seifert, R. Engelmann, C. Flamant, R. Bhawar, and P. DiGirolamo (2011), Comparison of Raman–lidar observations of water vapor with COSMO–DE forecasts during COPS 2007, *Weather and Forecasting*, **26**, 2011WAF2222448.1.

Knippertz, P., **M. Tesche**, B. Heinold, K. Kandler, and C. Toledano (2011), Dust mobilization and

aerosol transport from West Africa to Cape Verde—A meteorological overview of SAMUM–2, *Tellus*, **63B**, j.1600-0889.2011.00544.x.

Köhler, C. H., T. Trautmann, E. Lindermeir, W. Vreeling, K. Lieke, K. Kandler, B. Weinzierl, S. Groß, and **M. Tesche** (2011), Comparison of ground–based radiation measurements in the thermal IR during SAMUM–2 with radiative transfer simulations, *Tellus*, **63B**, j.1600-0889.2011.00563.x.

Schladitz, A., T. Müller, S. Nordmann, **M. Tesche**, S. Groß, V. Freudenthaler, J. Gasteiger, and A. Wiedensohler (2011), In–situ aerosol characterization at Cape Verde part 2: Parameterization of relative humidity and wavelength–dependent aerosol optical properties, *Tellus*, **63B**, j.1600-0889.2011.00568.x.

Schumann, U., B. Weinzierl, O. Reitebuch, H. Schlager, A. Minikin, C. Forster, R. Baumann, T. Sailer, K. Graf, H. Mannstein, C. Voigt, S. Rahm, R. Simmet, M. Scheibe, M. Lichtenstern, P. Stock, H. Rueba, D. Schaeuble, A. Tafferner, M. Rautenhaus, T. Gerz, H. Ziereis, M. Krautstrunk, C. Mallaun, J.-F. Gayet, K. Lieke, K. Kandler, M. Ebert, S. Weinbruch, A. Stohl, J. Gasteiger, S. Groß, V. Freudenthaler, M. Wiegner, A. Ansmann, **M. Tesche**, H. Olafsson, K. Sturm (2011), Airborne observations of the Eyjafjalla volcano ash cloud over Europe during air space closure in April and May 2010, *Atmos. Chem. Phys.*, **11**, 2245-2279.

Seifert, P., A. Ansmann, S. Groß, V. Freudenthaler, B. Heinold, A. Hiebsch, J. Schmidt, F. Schnell, **M. Tesche**, U. Wandinger, I. Mattis, and M. Wiegner (2011), Ice formation in ash–influenced clouds after the eruption of the Eyjafjallajökull volcano in April 2010, *J. Geophys. Res.*, **116**, 2011JD015702.

Tesche, M., A. Ansmann, D. Müller, D. Althausen, R. Engelmann, V. Freudenthaler, S. Gross, and M. Esselborn (2011), Profiling of Saharan dust and biomass burning smoke with multiwavelength polarization Raman lidar at Cape Verde, *Tellus*, **63B**, j.1600-0889.2011.00548.x.

Tesche, M., D. Müller, S. Groß, A. Ansmann, D. Althausen, V. Freudenthaler, B. Weinzierl, A, Veira, and A. Petzold (2011), Optical and microphysical properties of smoke over Cape Verde inferred from multiwavelength lidar measurements, *Tellus*, **63B**, j.1600-0889.2011.00549.x.

Weinzierl, B., D. Sauer, M. Esselborn, S. Mund, A. Petzold, A. Veira, **M. Tesche**, A. Ansmann, and M. Wirth (2011), Airborne observations of microphysical and optical properties of dust and biomass–burning aerosol layers in the Cape Verde region during SAMUM (2008), *Tellus*, **63B**, j.1600-0889.2011.00566.x.

Ansmann, A., **M. Tesche**, S. Groß, V. Freudenthaler, P. Seifert, A. Hiebsch, J. Schmidt, U. Wandinger, I. Mattis, D. Müller, and M. Wiegner (2010), The 16 April 2010 major volcanic ash plume over central Europe: EARLINET lidar and AERONET photometer observations at Leipzig, Germany, *Geophys. Res. Lett.*, **37**, 2010GL043809

Mattis, I., P. Seifert, D. Müller, **M. Tesche**, A. Hiebsch, T. Kanitz, J. Schmidt, F. Finger, U. Wandinger, and A. Ansmann (2010), Volcanic aerosol layers observed with multiwavelength Raman lidar over central Europe in 2008–2009, *J. Geophys. Res.*, **115**, 2009JD013472.

Müller, D., B. Weinzierl, A. Petzold, K. Kandler, A. Ansmann, T. Müller, **M. Tesche**, V. Freudenthaler, M. Esselborn, B. Heese, D. Althausen, A. Schladitz, S. Otto, and P. Knippertz (2010), Mineral dust observed with AERONET Sun photometer, Raman lidar, and in situ instruments during SAMUM 2006: Shape–independent particle properties, *J. Geophys. Res.*, **115**, 2009JD012520.

Müller, D., A. Ansmann, V. Freudenthaler, K. Kandler, C. Toledano, A. Hiebsch, J. Gasteiger, M. Esselborn, **M. Tesche**, B. Heese, D. Althausen, B. Weinzierl, and W. von Hoyningen–Huene (2010), Mineral dust observed with AERONET Sun photometer, Raman lidar, and in situ instruments during SAMUM 2006: Shape–dependent particle properties, *J. Geophys. Res.*, **115**, 2009JD012523.

Seifert, P., A. Ansmann, I. Mattis, U. Wandinger, **M. Tesche**, R. Engelmann, D. Müller, C. Pérez, and K. Haustein (2010), Saharan dust and heterogeneous ice formation: Eleven years of cloud observations at a central–European EARLINET site, *J. Geophys. Res.*, **115**, 2009JD013222.

Tesche, M., A. Ansmann, A. Hiebsch, I. Mattis, J. Schmidt, P. Seifert, and U. Wandinger (2010), Lidar observations of the Eyjafjallajökull volcanic ash plume at Leipzig, Germany, *Proceedings of SPIE*, **7827**, pp. xxii-xxx.

Wandinger, U., **M. Tesche**, P. Seifert, A. Ansmann, D. Müller, and D. Althausen (2010), Size matters: Influence of multiple scattering on CALIPSO light–extinction profiling in desert dust, *Geophys. Res. Lett.*, **37**, 2010GL042815.

Ansmann, A., **M. Tesche**, P. Knippertz, E. Bierwirth, D. Althausen, D. Müller, and O. Schulz (2009), Vertical profiling of convective dust plumes in southern Morocco during SAMUM, *Tellus*, **61B**, j.1600-0889.2008.00384.x.

Ansmann A., H. Baars, **M. Tesche**, D. Müller, D. Althausen, R. Engelmann, T. Pauliquevis, and P. Artaxo (2009), Dust and smoke transport from Africa to South America: Lidar profiling over Cape Verde and the Amazon rainforest, *Geophys. Res. Lett.*, **36**, 2009GL037923.

Ansmann, A., **M. Tesche**, P. Seifert, D. Althausen, R. Engelmann, J. Fruntke, U. Wandinger, I. Mattis, and D. Müller (2009), Evolution of the ice phase in tropical altocumulus: SAMUM lidar observations over Cape Verde, *J. Geophys. Res.*, **114**, 2008JD011659.

Bierwirth, E., M. Wendisch, A. Ehrlich, B. Heese, **M. Tesche**, D. Althausen, A. Schladitz, D. Müller, S. Otto, T. Trautmann, T. Dinter, W. von Hoyningen–Huene, and R. Kahn (2009), Spectral surface albedo over Morocco and its impact on the radiative forcing of Saharan dust, *Tellus*, **61B**, j.1600-0889.2008.00395.x.

Esselborn, M., M. Wirth, A. Fix, B. Weinzierl, K. Rasp, **M. Tesche**, and A. Petzold (2009), Spatial distribution and optical properties of Saharan dust observed by airborne high spectral resolution lidar during SAMUM 2006, *Tellus*, **61B**, j.1600-0889.2008.00394.x.

Freudenthaler, V., M. Esselborn, M. Wiegner, B. Heese, **M. Tesche**, A. Ansmann, D. Müller, D. Althausen, M. Wirth, A. Fix, G. Ehret, P. Knippertz, C. Toledano, J. Gasteiner, M. Garhammer, and M. Seefeldner (2009), Depolarization–ratio profiling at several wavelengths in pure Saharan dust during SAMUM 2006, *Tellus*, **61B**, j.1600-0889.2008.00396.x.

Haustein, K., C. Pérez, J. M. Baldasano, D. Müller, **M. Tesche**, A. Schladitz, M. Esselborn, B. Weinzierl, K. Kandler, and W. von Hoyningen–Huene (2009), Regional dust model performance during SAMUM 2006, *Geophys. Res. Lett.*, **36**, 2008GL036463.

Heese, B., D. Althausen, T. Dinter, M. Esselborn, T. Müller, **M. Tesche**, and M. Wiegner (2009), Vertically resolved dust optical properties during SAMUM: Tinfou compared to Ouarzazate, *Tellus*, **61B**, j.1600-0889.2008.00404.x.

Heinold, B., I. Tegen, M. Esselborn, K. Kandler, P. Knippertz, D. Müller, A. Schladitz, **M. Tesche**, B. Weinzierl, A. Ansmann, D. Althausen, B. Laurent, A. Massling, T. Müller, A. Petzold, K. Schepanski, and A. Wiedensohler (2009), Regional Saharan dust modelling during the SAMUM 2006 campaign, *Tellus*, **61B**, j.1600-0889.2008.00387.x.

Kaaden, N., A. Massling, A. Schladitz, T. Müller, K. Kandler, L. Schütz, B. Weinzierl, A. Petzold, **M. Tesche**, S. Leinert, and A. Wiedensohler (2009), State of mixing, shape factor, number size distribution, and hygroscopic growth of the Saharan anthropogenic and mineral dust aerosol at Tinfou, Morocco, *Tellus*, **61B**, j.1600-0889.2008.00388.x.

Knippertz, P., A. Ansmann, D. Althausen, D. Müller, **M. Tesche**, E. Bierwirth, T. Dinter, T. Müller, W. von Hoyningen–Huene, K. Schepanski, M. Wendisch, B. Heinold, K. Kandler, A. Petzold, L. Schütz, and I. Tegen (2009), Dust mobilization and transport in the northern Sahara during SAMUM 2006— A meteorological overview, *Tellus*, **61B**, j.1600-0889.2008.00380.x.

Mattis, I., **M. Tesche**, M. Grein, V. Freudenthaler, and D. Müller (2009), Systematic error of lidar profiles caused by a polarization–dependent receiver transmission: Quantification and error correction scheme, *Appl. Opt.*, **48**, 2742–2751.

Müller, D., B. Heinold, **M. Tesche**, I. Tegen, D. Althausen, L. A. Arboledas, V. Amiridis, A. Amodeo, A. Ansmann, D. Balis, A. Comeron, G. D'amico, E. Gerasopoulos, J. L. Guerrero-Rascado, V. Freudenthaler, E. Giannakaki, B. Heese, M., Iarlori, P. Knippertz, R. E., Mamouri, L. Mona, A. Papayannis, G. Pappalardo, R.-M. Perrone, G. Pisani, V. Rizi, M. Sicard, N. Spinelli, A. Tafuro, and M. Wiegner (2009), EARLINET observations of the 14-22-May long-range dust transport event during SAMUM 2006: Validation of results from dust transport modelling, *Tellus*, **61B**, j.1600-0889.2008.00400.x.

Otto, S., E. Bierwirth, B. Weinzierl, K. Kandler, M. Esselborn, **M. Tesche**, M. Wendisch, and T. Trautmann (2009), Radiative effects of a Saharan dust plume observed during SAMUM assuming non–spherical dust particles, *Tellus*, **61B**, j.1600-0889.2008.00381.x.

Tesche, M., A. Ansmann, D. Müller, D. Althausen, R. Engelmann, V. Freudenthaler, and S. Groß (2009), Vertically resolved separation of dust and smoke over Cape Verde by using multiwavelength

Raman and polarization lidars during Saharan Mineral Dust Experiment, *J. Geophys. Res.*, **114**, 2009JD011862.

Tesche, M., A. Ansmann, D. Müller, D. Althausen, I. Mattis, B. Heese, V. Freudenthaler, M. Wiegner, M. Esselborn, G. Pisani, and P. Knippertz (2008), Vertical profiling of Saharan dust with Raman lidars and airborne HSRL in southern Morocco during SAMUM, *Tellus*, **61B**, j.1600-0889.2008.00390.x.

Wiegner, M., J. Gasteiger, K. Kandler, B. Weinzierl, K. Rasp, M. Esselborn, V. Freudenthaler, B. Heese, C. Toledano, **M. Tesche**, and D. Althausen (2009), Numerical simulations of optical properties of Saharan dust aerosols with emphasis on linear depolarization ratio, *Tellus*, **61B**, j.1600-0889.2008.00381.x.

Ansmann, A., **M. Tesche**, D. Althausen, D. Müller, V. Freudenthaler, B. Heese, M. Wiegner, G. Pisani, P. Knippertz and O. Dubovik (2008), Influence of Saharan dust on cloud glaciation in southern Morocco during the Saharan Mineral Dust Experiment, *J. Geophys. Res.*, **113**, 2007JD008785.

Cheng, Y. F., A. Wiedensohler, H. Eichler, J. Heintzenberg, **M. Tesche**, A. Ansmann, M. Wendisch, H. Su, D. Althausen, H. Herrmann, T. Gnauk, E. Brüggemann, M. Hu, and Y. H. Zhang (2008), Relative humidity dependence of aerosol optical properties and direct radiative forcing in the surface boundary layer at Xinken in Pearl River Delta of China: An observation based numerical study, *Atmos. Envir.*, **42**, j.atmosenv.2008.04.009.

Eichler, H., Y. F. Cheng, W. Birmili, A. Wiedensohler, E. Brüggemann, T. Gnauk, H. Herrmann, D. Althausen, A. Ansmann, R. Engelmann, **M. Tesche**, Y. H. Zhang, M. Hu, S. Liu, and L.M. Zeng (2008), Hygroscopic properties and ambient extinction of aerosol particles in south–eastern China, *Atmos. Envir.*, **42**,
j.atmosenv.2008.05.007.

Esselborn, M., M. Wirth, A. Fix, **M. Tesche**, and G. Ehret (2008), Airborne high spectral resolution lidar for measuring aerosol extinction and backscatter coefficients, *Appl. Opt.*, **47**, 346–358.

Fan, S., B. Wang, **M. Tesche**, R. Engelmann, D. Althausen, J. Liu, W. Zhu, Q. Fan, M. Li, N. Ta, L. Song, and K. Leong (2008), Meteorological conditions and structures of atmospheric boundary layer in October 2004 over Pearl River Delta area, *Atmos. Envir.*, **42**, j.atmosenv.2008.01.067.

Grzeschik, M., H.–S. Bauer, V. Wulfmeyer, D. Engelbart, U. Wandinger, I. Mattis, D. Althausen, R. Engelmann, **M. Tesche**, and A. Riede (2008), Four–dimensional variational analysis of water–vapor Raman lidar data and their impact on mesoscale forecasts, *J. Atmos. Ocean. Tech.*, **25**, 2007JTECHA974.1.

Mattis I., D. Müller, A. Ansmann, U. Wandinger, J. Preißler, P. Seifert, and **M. Tesche** (2008), Ten years of multiwavelength Raman lidar observations of free–tropospheric aerosol layers over central Europe: Geometrical properties and annual cycle, *J. Geophys. Res.*, **113**, 2007JD009636.

Tesche, M., D. Müller, A. Ansmann, M. Hu, and Y. Zhang (2008), Retrieval of microphysical properties of aerosol particles from one–wavelength Raman lidar and multiwavelength Sun photometer observations, *Atmos. Envir.*, **42**, j.atmosenv.2008.02.014.

Mattis, I., L. Mona, D. Müller, G. Pappalardo, L. A. Arboledas, G. D'Amico, A. Amodeo, A. Apituley, J. M. Baldasano, C. Böckmann, J. Bösenberg, A. Chaikovsky, A. Comeron, E. Giannakaki, I. Grigorov, J. L. G. Rascado, O. Gustafsson, M. Iarlori, H. Linné, V. Mitev, D. N. Francisco Molero Menendez, D. Nicolae, A. Papayannis, C. P. García-Pando, M. R. Perrone, A. Pietruczuk, J.-P. Putaud, F. Ravetta, A. Rodríguez, P. Seifert, M. Sicard, V. Simeonov, P. Sobolewski, N. Spinelli, K. Stebel, A. Stohl, **M. Tesche**, T. Trickl, X. Wang, and M. Wiegner (2007), EARLINET correlative measurements for CALIPSO, *Proceedings of SPIE.*, **6750**, art. no. 67500Z.

Müller, D., A. Ansmann, I. Mattis, **M. Tesche**, U. Wandinger, D. Althausen, and G. Pisani (2007), Aerosol–type–dependent lidar ratio observed with Raman lidar, *J. Geophys. Res.*, **112**, 2006JD008292.

Tesche, M., A. Ansmann, D. Müller, D. Althausen, R. Engelmann, M. Hu, and Y. Zhang (2007), Particle backscatter, extinction, and lidar ratio profiling with Raman lidar in South and North China, *Appl. Opt.*, **46**, 6302–6308.

Müller, D., **M. Tesche**, H. Eichler, R. Engelmann, D. Althausen, A. Ansmann, Y. F. Cheng, Y. H. Zhang, and M. Hu (2006), Strong particle light absorption over the Pearl River Delta (South China) and

Beijing (North China) determined from combined Raman lidar and Sun photometer observations, *Geophys. Res. Lett.*, **33**, 2006GL027196.

Pahlow, M., D. Müller, **M. Tesche**, H. Eichler, G. Feingold, W. L. Eberhard, and Y. F. Cheng (2006), Retrieval of aerosol properties from combined multiwavelength lidar and sunphotometer measurements, *Appl. Optics*, **45**, 7429–7442.

Wandinger, U., I. Mattis, **M. Tesche**, A. Ansmann, J. Bösenberg, A. Chaikovsky, V. Freudenthaler, L. Komguem, H. Linné, V. Matthias, J. Pelon, L. Sauvage, P. Sobolewski, G. Vaughan, and M. Wiegner (2004), Air–mass modification over Europe: EARLINET aerosol observations from Wales to Belarus, *J. Geophys. Res.*, **109**, 2004JD005142.

Invited talks

Aerosol-Cloud-Interactions, Fortbildungtag der DMG Sektion München (22 November 2019)
Future directions in aerosol profiling with lidar, Stockholm University (5 December 2018)
Aviation effects on already existing cirrus clouds, National Observatory of Athens, Greece (22 November 2017)
PM monitoring from space, lecture at the 2nd ECARS summer school on Crete, Greece (7 April 2017)
Aviation effects on already-existing cirrus clouds, seminar at DLR Oberpfaffenhofen (24 Oct 2016)
Plane tracks in cirrus clouds, seminar at Stockholm University (14 Oct 2015)
Observing volcanic ash layers with lidar, AVT-213 Volcanic Ash meeting, Karlstad, Sweden (13 May 2013)

Contributions to international conferences

This list only includes presentations as first or presenting author.

posters at AGU 2019 in San Francisco, USA (2019): *Aerosol-cloud interactions from combined observations with geostationary and polar-orbiting sensors* and *Aerosol-type classification based on AERONET version 3 inversion products*

poster at MOPGA Kick-Off Meeting in Paris, France (2019): *Overview of the MOPGA PACIFIC project*

talk at ELC2018 in Thessaloniki, Greece: *3+2+X: On the optimum depolarisation input for inverting lidar measurements of non-spherical particles*

poster at ILRC 28 in Bucharest, Romania (2017): *Lidar Spectroscopy Instrument (LiSsI) at the University of Hertfordshire – A facility for chemical profiling of aerosol particles*

talk at ICCP2016 in Manchester, United Kingdom: *Aviation effects on already-existing cirrus clouds*

posters at ICCP2016 in Manchester, United Kingdom: *Characterisation of clouds during ASCE 2014* and *Lidar observations of the effect of gravity-wave activity in the properties of Polar Stratospheric Clouds*

talk at DUST2016 in Castellaneta Marina, Italy: *Vertical profiles of mineral dust in mixed East Asian pollution plumes based on Raman spectrometer lidar measurements*, contribution withdrawn for personal reasons

poster at AGU 2015 in San Francisco, USA: *"Plane tracks" in cirrus clouds*

poster at 12th Ny-Ålesund Seminar in Tromsø, Norway (2015): *Reconciling aerosol light extinction measurements from spaceborne lidar observations and in situ measurements in*

the Arctic

talk at AMS 2015 in Phoenix, USA: *Vertical profiles of mineral dust in mixed East Asian pollution plumes based on Raman spectrometer lidar measurements*

posters at NOSA 2014 Aerosol Symposium in Stockholm, Sweden: *Seasonal variations in the development of the planetary boundary layer at Stockholm, Sweden, as derived from three years of aerosol lidar measurements* and *Obtaining PM2.5 in the Stockholm region from spaceborne AOT measurements*

talk at AirQuality2014 in Garmisch-Partenkirchen, Germany: *Obtaining PM2.5 in the Stockholm region from spaceborne AOT measurements*

poster at EGU 2013 in Vienna, Austria: *Reconciling light extinction measurements from in situ/remote sensing and ground/space*

posters at EAC 2013 in Prague, Czech Republic: *Reconciling aerosol light extinction from ground-based in-situ measurements and active satellite remote sensing* and *Estimating PM2.5 in the Stockholm region from spaceborne AOT measurements*

poster at AirQuality2012 in Athens, Greece: *Volcanic ash over Scandinavia originating from the Grímsvötn eruptions in May 2011*

posters at EGU 2012 in Vienna, Austria: *Volcanic ash over Scandinavia originating from the Grímsvötn eruptions in May 2011* and *Assessment of diverse algorithms applied on MODIS Aqua and Terra data over land surfaces in Europe*

talk at ILRC 26 in Porto Helio, Greece (2012): *Ground–based validation of CALIPSO observations of dust and smoke in the Cape Verde region*

poster at ILRC 26 in Porto Helio, Greece (2012): *Volcanic ash over Scandinavia originating from the Grímsvötn eruptions in May 2011*

talk at EGU 2011 in Vienna, Austria: *Separation of volcanic ash and sulfate aerosol based on lidar–photometer observations in central Europe after the eruption of the Eyjafjallajökull volcano*

talk at SPIE Remote Sensing 2010 in Toulouse, France: *Lidar observations of the Eyjafjallajökull volcanic ash plume at Leipzig, Germany*

poster at IAC 2010 in Helsinki, Finland: *Lidar observations of the Eyjafjallajökull volcanic ash plume at Leipzig, Germany, in the framework of EARLINET*

talk at ILRC 25 in Sankt Petersburg, Russia (2010): *Vertically resolved separation of dust and smoke over Cape Verde during SAMUM–2*

talk at EGU 2009 in Vienna, Austria: *Lidar observations during the Saharan Mineral Dust Experiments*

talk at ILRC 24 in Boulder, USA (2008): *Lidar observations of pure and aged Saharan dust during the Saharan Mineral Dust Experiments 1 & 2*

poster at the Third International Workshop on Mineral Dust in Leipzig, Germany (2008): *Lidar observations of pure and aged Saharan dust during the Saharan Mineral Dust Experiments 1 & 2*

talk at ILRC 23 in Nara, Japan (2006): *Optical and microphysical properties of aerosols in southern (Pearl River Delta) and northern China (Beijing) observed with Raman lidar and Sun photometer*

Author's Declaration

I hereby declare that the present thesis has been produced by myself and without the assistance of further individuals or parties. All used sources have been included in the list of references. Reproduced or adapted text passages, tables and figures have been marked as such or provided with the respective reference. All papers included in this thesis have been reprinted with the permission of the respective publishers.

I also confirm that this thesis or a similar version of this thesis has neither been submitted nor rated elsewhere to achieve the academic degree of Doctor rerum naturalium habilitatus. The electronic version of this thesis is identical to the printed version which has been submitted to the habilitation commission at the Faculty of Physics and Earth Sciences at Leipzig University.

Leipzig, 20 July 2020   Matthias Tesche

Paper I

The author conducted and analysed the lidar measurements at Leipzig, prepared the figures, and contributed to the method development and the writing of the paper.

Paper II

Ansmann, A., **M. Tesche**, P. Seifert, S. Groß, V. Freudenthaler, A. Apituley, K. Wilson, I. Serikov, V. Linné, B. Heinold, A. Hiebsch, F. Schnell, J. Schmidt, I. Mattis, U. Wandinger, and M. Wiegner (2011)
Ash and fine-mode particle mass profiles from EARLINET-AERONET observations over central Europe after the eruptions of the Eyjafjalla-jökull volcano in 2010

The author conducted and analysed the lidar measurements at Leipzig, prepared the figures, and contributed to the method development and the writing of the paper.

Paper III

The author conceived this study, conducted the lidar measurements at Stockholm, and led the method development, data analysis, figure preparation and writing of the manuscript.

Paper IV

Paper V

The author contributed to the development and the writing of the publication, prepared the figures, and contributed to the discussion of the findings and revision of the manuscript.

Paper VI

The author conceived this study, performed the ground-based measurements at Cape Verde, and led the method development, data analysis, figure preparation, and writing of the manuscript.

Paper VII

Paper VIII

Tesche, M., P. Zieger, N. Rastak, R. J. Charlson, P. Glantz, P. Tunved, and H.-C. Hansson (2014)
Reconciling aerosol light extinction measurements from spaceborne lidar observations and in-situ measurements in the Arctic

Paper IX

Paper X

The author performed parts of the measurements and contributed to the preparation of the figures and the manuscript as well as in the discussion of the findings.

Paper XI

Paper XII

Shin, S.-K., **M. Tesche**, K. Kim, M. Kezoudi, B. Tatarov, D. Müller, and Y. Noh (2018)

Paper XIII

Paper XIV